Listening to the Universe with next generation ground-based gravitational-wave detectors

Ssohrab Borhanian[1, 2, 3, 4, *] and B. S. Sathyaprakash[1, 5, 6]

[1]*Institute for Gravitation and the Cosmos, Department of Physics, Pennsylvania State University, University Park, Pennsylvania 16802, USA*
[2]*Theoretisch-Physikalisches Institut, Friedrich-Schiller-Universität Jena, Fröbelstieg 1, 07743 Jena, Germany*
[3]*Dipartimento di Fisica "G. Occhialini", Universitá degli Studi di Milano-Bicocca, Piazza della Scienza 3, 20126 Milano, Italy*
[4]*INFN, Sezione di Milano-Bicocca, Piazza della Scienza 3, 20126 Milano, Italy*
[5]*Department of Astronomy and Astrophysics, Pennsylvania State University, University Park, Pennsylvania 16802, USA*
[6]*School of Physics and Astronomy, Cardiff University, Cardiff, CF24 3AA, United Kingdom*
(Dated: November 13, 2024)

In this study, we use simple performance metrics to assess the science capabilities of future ground-based gravitational-wave detector networks—composed of A+ or Voyager upgrades to the LIGO, Virgo, and KAGRA observatories and proposed next generation observatories such as Cosmic Explorer and Einstein Telescope. These metrics refer to coalescences of binary neutron stars (BNSs) and binary black holes (BBHs) and include: (i) network detection efficiency and detection rate of cosmological sources as a function of redshift, (ii) signal-to-noise ratios and the accuracy with which intrinsic and extrinsic parameters would be measured, and (iii) enabling multimessenger astronomy with gravitational waves by accurate 3D localization and early warning alerts. We further discuss the science enabled by the small population of rare and extremely loud events. While imminent upgrades will provide impressive advances in all these metrics, next generation observatories will deliver an improvement of an order-of-magnitude or more in most metrics. In fact, a network containing two or three such facilities will detect half of all the BNS and BBH mergers up to a redshift of $z = 1$ and $z = 20$, respectively, give access to hundreds of BNSs and ten thousand BBHs with signal-to-noise ratios exceeding 100, readily localize hundreds to thousands of mergers to within 1 deg^2 on the sky and better than 10% in luminosity distance, respectively, and consequently, enable mutlimessenger astronomy through follow-up surveys in the electromagnetic spectrum several times a week. Such networks will further shed light on potential cosmological merger populations and detect an abundance of high-fidelity BNS and BBH signals which will allow investigations of the high-density regime of matter at an unprecedented level and enable precision tests of general relativity in the strong-field regime, respectively.

I. INTRODUCTION:

A. Dawn of gravitational-wave astronomy

Over the past five years and three observing runs, the Advanced Laser Interferometer Gravitational-Wave Observatory (LIGO) consisting of the LIGO-Hanford and LIGO-Livingston detectors [1] and the Virgo detector [2] have discovered gravitational waves (GWs) from the merger of dozens of binary black holes (BBHs) [3–8], two binary neutron stars (BNSs) [9, 10] and two binary neutron star-black holes (NSBHs) [11]. In addition to the pioneering first direct observation of GWs from a pair of merging BBHs (GW150914) [3], LIGO and Virgo have made many spectacular and surprising new discoveries. These include, amongst others, a BNS merger that was observed in the entire electromagnetic window from gamma-rays to radio waves (GW170817) [9, 12, 13], systems in which black hole (BH) companions have masses that could not have resulted from the evolution of massive stars (thus raising questions as to their origin, GW170729 [14] and GW190521 [15, 16]), binaries that show a clear signature of sub-dominant octupole radiation in addition to the dominant quadrupole (confirming once again predictions of general relativity, GW190412 [17] and GW190814 [18]), and a binary with a mass-ratio of almost 1:10 that challenges astrophysical BBH formation models while its secondary companion could well be the heaviest neutron star (NS) or the lightest BH observed so far (GW190814 [18]). GW catalogs compiled by other groups [19–23] have largely confirmed the population of coalescing compact binaries found by LIGO and Virgo but have reported additional events of interest (see, e.g., [24–28])

These discoveries have already made a massive impact on our understanding of different tenets of astrophysics, fundamental physics, and cosmology. They have allowed a first glimpse into the dynamics of strongly curved spacetimes and the validity of general relativity (GR) in unexplored regimes of the theory [29–34], raised deeper questions on the formation mechanisms and evolutionary scenarios of compact objects [16, 18, 35–46], provided a new tool for measuring cosmic distances that will help in precision cosmology [47, 48] and in mapping the large scale structure of the Universe [49–52], and brought to bear a novel approach to determine the structure and properties of NSs to help in the exploration of the dense matter equation of state which governs the dynamics of NS cores [53–63]. The second part of the third observing run saw the discovery of two neutron star-black hole binaries, GW200105 (a marginal event) and GW20015 [11, 64] thereby completing the quest for the three types of ultra-compact-object binaries, two of which have only been observed in the gravitational window.

At the same time, multimessenger observations of GW170817—the inspiral and coalescence of a pair of NSs—have at once begun to impact on several enigmatic questions in nuclear astrophysics and fundamental physics. We now know that BNS mergers are progenitors of short, hard gamma-ray bursts [13] and sites where r-process heavy elements are produced from neutron-rich ejecta [65–74], GWs travel at the speed of light to within one part in 10^{15} [13] which has helped rule out certain alternative theories of gravity that were invoked to explain the origin of dark energy [75, 76], and that

* ssohrab.borhanian@unimib.it

the equation of state of dense matter cannot be too stiff, thus constraining the radius of NSs of 1.4 $M_\odot$ to be below about 14 km [54, 55]. Moreover, the luminosity distance determined by gravitational-wave observations and the redshift from the identification of the host galaxy allowed the first measurement of the Hubble constant with standard sirens [77, 78] thus beginning a new era in observational cosmology [79–81] envisaged more than three decades ago [47].

LIGO-Virgo discoveries have informed numerous investigations about the properties of NSs and BHs including the maximum mass of NSs [82–86], potential primordial origin of the observed BHs [87–93], stochastic backgrounds that might be produced by the astrophysical population of BBH and BNS mergers [94–96], to name a few. It has already become clear that the GW window has the potential to transform our knowledge of physics and astronomy in the coming decades—some of which we hope to explore in this study.

B. Imminent upgrade and new detectors

With the planned sensitivity improvements of Advanced LIGO and Advanced Virgo [97, 98]) and the addition of two new detectors, KAGRA [99, 100] and LIGO-India [101, 102]), the next five years of gravitational-wave astronomy will enable significant advances in resolving some of the outstanding problems in physics and astronomy. We will explore in detail the potential of this imminent *A+ detector generation* (i.e. upgrades to Advanced LIGO, Advanced Virgo, and KA-
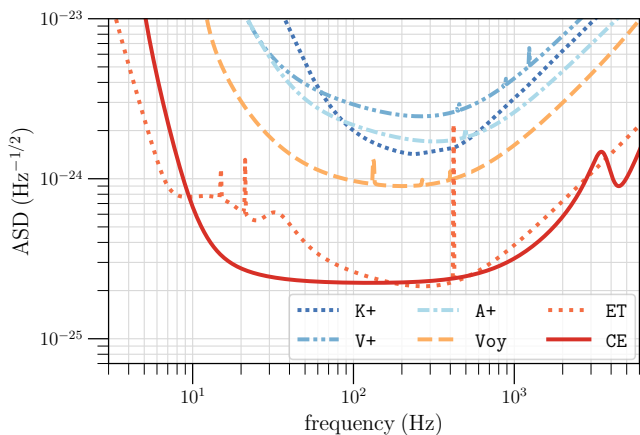

FIG. 1. Amplitude spectral densities (ASDs) illustrating the sensitivities of three generations of detectors: (i) Advanced-plus upgrade of LIGO (A+: Hanford, Livingston, and India), Virgo (V+: Italy), and KAGRA (K+: Japan), (ii) Voyager upgrade of LIGO (Voy), and (iii) the next generation of detectors consisting of Cosmic Explorer (CE) and Einstein Telescope (ET). These ASDs could be realized in the next 5, 10, and 15-20 years, respectively. Refer to the text for different detector networks, composed of combinations of these detectors, considered in this paper. The ASDs are taken from the `kagra_plus`, `advirgo_plus`, `aplus`, `voyager_cb`, `et`, and `ce2_40km_cb` .txt-files inside `ce_curves.zip` file at   https://dcc.cosmicexplorer.org/public/0163/T2000007/005/ ce_curves.zip. The shown ET ASD is scaled by a factor of 2/3 to represent the effective sensitivity of ET's triangular design.

GRA with sensitivity curves shown in Fig. 1). The Hubble-Lemaître tension—the discrepancy between the early and late Universe measurements of the Hubble constant [103]—could be resolved by the A+ network with multimessenger observations of ∼ 50 BNS mergers [79] or with the identification of a handful of BBHs within 500 Mpc [80]. The BNS mergers could also help gain first insights into the cold equation of state of dense cores of neutron stars. The A+ generation will observe several BBH mergers each day and a loud BBH event (with signal-to-noise ratio in excess of 100) each month (cf. Fig. 2, bottom right panel)—events that would help verify the BH no-hair theorem and further constrain GR or see hints of its violation.

C. Future of gravitational-wave astronomy

It is possible to further enhance the sensitivity of current facilities with new lasers, cryo-cooled mirror substrates, active noise cancellation techniques for gravity gradient, and the like. The concept of Voyager technology [104], which can be installed in current facilities, aims to improve the sensitivity beyond A+ detectors by a factor of ∼ 2 to 4 depending on the frequency. New facilities—such as interferometers with longer arms—and instrumentation would be needed to make sensitivity improvements beyond that facilitated by the Voyager concept. Einstein Telescope (ET) [105, 106], Cosmic Explorer (CE) [107], and Neutron Star Extreme Matter Observatory (NEMO) [108] are three such concepts (jointly referred to as next generation or, simply, NG) that are currently being pursued with the hope of first facilities being built within the next 10 to 15 years.

There have been extensive studies on the capability of next generation detectors and the scientific discoveries they enable [102, 109–129]. In this study we will focus in detail on the potential of the Voyager, ET, and CE detector generations using the Voy, ET, and CE noise curves shown in Fig. 1. While out of the scope of our investigation, the triangular geometry proposed for ET facilitates a particularly powerful probe of the detector's sensitivity and data quality. In a triangular configuration, ET consists of three V-shaped detectors, each with an opening angle of 60 degrees, rotated relative to each other by 120 degrees. The sum of the responses of the three detectors, called the *null stream* [130], is, by construction, devoid of any GW signals [109]. This null stream enables an unbiased estimation of the detector's sensitivity, free from the confusion noise from the background of unresolved GW sources, and also provides a way of measuring non-stationary, incoherent noise artifacts [131].

We find that a Voyager network would localize ∼ 16 BNS mergers within a redshift of 0.5 to within 1 deg², providing ample opportunity for EM follow-up, and detect thousands of BNS mergers within its per-mille redshift of $z = 0.9$ (see Sec. III for definitions of the per-mille redshift and reach used in this paper). In contrast, the best NG network would detect almost every BNS merger, some 50,000 of them, up to a redshift of $z = 0.9$, localizing a few thousand of them to better than 1 deg², measuring distances to more than ten thousand of the mergers to an accuracy better than 10%. Together with EM follow-up observations, such high-fidelity measurements

would provide unprecedented access to fundamental questions in physics and astronomy including the nature of NSs, central engines of gamma-ray jets, production of heavy elements in the Universe, and the expansion rate as a function of redshift. NG observatories would have a reach of $z \sim 1$–2 to BNS mergers and a per-mille redshift of $z \sim 3$–10.

The Voyager network will have access to BBHs all the way to $z \sim 10$, detecting 50% of all mergers within a redshift of 1.4. It would achieve a signal-to-noise ratio of 100 for more than 50 mergers each year. The best NG network, on the other hand, will observe almost all BBH mergers within a redshift of 10, and at least every other BBH merger up to $z \gtrsim 30$. In fact, BBH mergers with signal-to-noise ratios of 1000 or larger will be observed more than 10 times each year. Such exquisite observations will allow extremely accurate measurements of BH masses, their spins and distances, allowing us to address a variety of questions in astrophysics and dynamical spacetimes. These include, but are not limited to, the astrophysical models of the formation and evolution of BBHs, tests of the BH no-hair theorem, exploration of the epoch of the formation of first stars at redshifts of 10–30, etc.

D. Organization of the paper

In Sec. II we will introduce the detector networks we are considering in this study, the properties of the source populations we are examining, and the analysis methodology we are using to assess the measurement capabilities of detector networks. In the rest of the paper we will introduce and discuss the metrics used to assess the relative performance of different networks. In Sec. III we will discuss the efficiency of detector networks in detecting signals as a function of redshift (or luminosity distance). Detection efficiency will inform us of the completeness of the observed population with respect to the full underlying population of mergers. Sec. III will also discuss the cosmic merger rate of compact binary coalescences inferred using current LIGO-Virgo observations, a model for the redshift evolution of the star formation rate and metallicity, and the resulting detection rates of the networks as functions of the redshift. In Sec. IV we will present the evaluation of the chosen detector networks and a forecast of the science questions that could be addressed by different generations of networks. Enabling multimessenger astronomy will require accurate 3D sky localization of compact binary coalescences, which will be the focus of Sec. V. This Section will also include forecasts for early warning alerts that would be possible with future detectors, with alerts sent to astronomers 10 minutes, 5 minutes, and 2 minutes before the merger occurs and the corresponding 3D sky localization of the event. Sec. VI is devoted to discussing the science enabled by rare events with SNRs larger than 300 or even 1000, e.g. observing higher multipole modes, testing the black hole no-hair theorem to exquisite precession, etc. Sec. VII provides a brief summary, limitations of the study, and how they might be improved and other studies that would be necessary to firm up the science potential of future detectors.

The Appendix contains further information about this study and the science capabilities of additional networks not reported in the main body of the paper. Appendix A reports the set-

TABLE I. The networks of GW detectors whose performance is evaluated using quantitative metrics discussed in Sec. III–VI. Note that the time-scale of operation of the various networks is our best guess estimate of when a given network is likely to operate; they do not correspond to any official projections.

Detectors	Network Name	Time-scale
LIGO (HLI+), Virgo+, KAGRA+	HLVKI+	2025-2030
LIGO (HLI-Voy), Virgo+, KAGRA+	VK+HLIv	2030-2035
ET, LIGO (HLI+), KAGRA+	HLKI+E	2035-2040
CE, Virgo+, KAGRA+ LIGO-I+	VKI+C	2040-2045
ET, CE, KAGRA+, LIGO-I+	KI+EC	2040-2045
ET, CE, CE-South	ECS	2040+

tings used in the Fisher-information software package GWBENCH [132]; this would help other interested users to more readily reproduce the results of this paper. Appendix B details how to access the raw data used in this study. Appendix C provides the best fit parameters of a (modified) sigmoid function that is used to fit the efficiency of detection of the various networks. In the main body of the paper we provide only the cumulative histograms of signal-to-noise ratios and parameter error estimates for the studied BNS and BBH populations in the different networks. Thus, in Appendix D we also present the histograms of the respective quantities. Finally, Appendix E compares the results for detector networks containing one or two CEs and with arm lengths of either 20 km or 40 km. Comparison of the results in this Appendix highlights the importance of having at least one 40 km Cosmic Explorer detector for the completeness of the detected catalogs and the need for the Einstein Telescope to accurately localize sources.

Unless specified otherwise, we use the geometric system of units in which Newton's constant and the speed of light are both set to unity: $c = G = 1$.

II. NETWORKS, POPULATIONS, AND METHODOLOGY

A. Detector networks

In this paper we will consider six global networks composed of at least three detectors in some combination of the aforementioned detector generations as described below and summarized in Tab. I:

1. An A+ network [133] consisting of the LIGO-Hanford (H), LIGO-Livingston (L), Virgo (V), KAGRA (K), and LIGO-India (I) detectors and denoted by HLVKI+ that could be operational in the next **5 to 10 years**,

2. A Voyager network [104] consisting of three LIGO detectors (HLI) operating with Voyager technology in addition to A+ versions of Virgo and KAGRA and denoted by VK+HLIv that could be operating in the next **10 to 15 years**, and

3. Four networks consisting of at least one NG detector (Einstein Telescope (E) in Italy [110], Cosmic Explorer (C) in the US [98], and Cosmic Explorer South (S) in Australia) together with a combination of A+ sensitivity

detectors, denoted as `HLKI+E`, `VKI+C`, `KI+EC`, and `ECS`. The fiducial locations of the ET and CE detectors can be found in Tab. III of [132]. Such networks are expected to be operational in roughly **15 to 20 years**.

Although the choice of when a specific A+ configuration is included in a NG network seems arbitrary, this resulted from our judgement that when a NG detector comes online the corresponding region's 2G+ detector(s) may no longer be in operation. For example, Virgo is not likely to be operational when ET is built, LIGO-Hanford and LIGO-Livingston may not be operating at the same time as CE. Should it prove necessary to assess the performance of a network comprised of a different combination of detectors, e.g. `HLI+C`, it would be straightforward to do so with GWBENCH, see Sec. II C for details.

B.   Source populations

Throughout this paper, we examine two source populations comprising either BNSs or BBHs. We assume the local (i.e. $z = 0$) merger rate for BNS and BBH to be $R_{\rm BNS} = 320^{+490}_{-240}\,{\rm Gpc}^{-3}\,{\rm yr}^{-1}$ and $R_{\rm BBH} = 24^{+14}_{-7}\,{\rm Gpc}^{-3}\,{\rm yr}^{-1}$, respectively [18], as determined by the first and second gravitational-wave transient catalogs [6, 7]. Redshift evolution of the rates is discussed in Sec. III D.

Each population was uniformly distributed in six redshift bins, $z \in [0.02, 0.5], [0.5, 1], [1, 2], [2, 4], [4, 10], [10, 50]$, with 250,000 injections per bin. The corresponding luminosity distances D_L were calculated with the PLANCK18 cosmology of ASTROPY. Uniform sampling over several redshift bins provides us with good parameter sampling. However, the probability density functions of the populations are scaled appropriately to capture the redshift-dependent merger rates (see Sec. IV A for details).

The injections were further uniformly sampled over sky positions (α and $\cos(\delta)$) and binary orientation angles ($\cos(\iota)$ and ψ), with right ascension α, declination δ, inclination ι, and polarization angle ψ. The injected spins were chosen to be aligned with the orbital angular momentum ($\chi_{1x} = \chi_{1y} = \chi_{2x} = \chi_{2y} = 0$) while the z-components were uniformly sampled, for BNS $\chi_{1z}, \chi_{2z} \in [-0.05, 0, 05]$ and for BBH $\chi_{1z}, \chi_{2z} \in [-0.75, 0, 75]$. The BNS masses were chosen to be normally distributed in $[1, 2]\,M_\odot$ with mean $\mu = 1.35\,M_\odot$ and standard deviation $\sigma = 0.15\,M_\odot$. The BBH masses were chosen to follow the `POWER+PEAK` distribution described in the Second Gravitational-Wave Transient Catalog population paper [134], but with the secondary mass sampled uniformly in $[5\,M_\odot, m_1]$. These parameters are summarized in Tab. II. Note that differences in the simulated populations and network configurations require cautious comparison with other literature.

C.   Analysis methodology

We assess the performance of the chosen GW networks using a fast, Fisher-information [135–138] based Python package, GWBENCH, that we developed and made publicly available [132]; Appendix A reports the settings used in GWBENCH

and Sec. VII B summarizes the limitations of the Fisher-information formalism. The Fisher information formalism approximates the parameter posteriors to be Gaussian (assuming Gaussian noise), provides an analytic recipe to calculate the covariance matrix of the posteriors, and thus allows the computation of measurement error estimates for the gravitational waveform parameters. The implementation in GWBENCH incorporates the effect of Earth's rotation, which is important for signals lasting for longer than about an hour, and numerical differentiation schemes, enabling access to a host of gravitational waveform models in LAL, the LSC Algorithm Library [139]—ultimately enabling the use of more sophisticated waveform models and, therefore, more accurate estimates. GWBENCH packs this in an easy-to-use fashion and further gives access to signal-to-noise ratio (SNR) calculations, various detector locations and noise curves, and basic sampling methods. Alternatively, the gravitational-wave community has developed other Fisher-information based Python packages such as GW-FAST [140] and GWFISH [141] that can be used to perform similar analyses.

Thus, the package allows us to make a comprehensive evaluation of the six chosen detector networks using well-defined performance metrics: SNR ρ, 90%-credible sky area Ω_{90}, and measurement error estimates of gravitational waveform parameters. The latter depend on the waveform models employed: For the BNS population we use the `IMRPhenomD_NRTidalv2` model [142] to accurately capture tidal effects. For the BBH population we use the `IMRPhenomXHM` [143, 144] model to accurately capture the dynamics of sub-dominant modes beyond the quadrupole that are important for highly mass-asymmetric systems which our BBH population includes. We perform the Fisher analysis over 9 parameters for both populations: chirp mass $\mathcal{M}$, symmetric mass ratio η, luminosity distance D_L, time and phase of coalescence t_c, ϕ_c, and the aforementioned binary orientation angles ι, ψ and sky positions α, δ. The Fisher analysis is performed in the frequency domain over the range $f_L = 5\,{\rm Hz}$ to $f_U = N\,f_{\rm isco}$ in $\mathrm{d}f = 1/16\,{\rm Hz}$ steps. The frequency at the innermost, stable, circular orbit for a

TABLE II. Sampling parameters for the BNS and BBH populations.

Population	BNS	BBH
m_1	Gaussian ($\mu = 1.35\,M_\odot$, $\sigma = 0.15\,M_\odot$)	`POWER+PEAK` [134]
m_2	Gaussian ($\mu = 1.35\,M_\odot$, $\sigma = 0.15\,M_\odot$)	uniform in $[5\,M_\odot, m_1]$
χ_{1x}, χ_{2x}	0	
χ_{1y}, χ_{2y}	0	
χ_{1z}, χ_{2z}	uniform in $[-0.05, 0.05]$	uniform in $[-0.75, 0.75]$
z	uniform in six bins: $[0.02, 0.5], [0.5, 1], [1, 2], [2, 4], [4, 10], [10, 50]$	
D_L	convert z via ASTROPY.PLANCK18	
$\cos(\iota)$	uniform in $[-1, 1]$	
α	uniform in $[0, 2\pi]$	
$\cos(\delta)$	uniform in $[-1, 1]$	
ψ	uniform in $[0, 2\pi]$	
t_c, φ_c	0	

binary of total mass M is defined as $f_{\rm isco} = (6^{3/2} \pi M)^{-1}$. The factor N is chosen to be 4 for `IMRPhenomD_NRTidalv2` and 8 for `IMRPhenomXHM` to include the full ringdown dynamics. In either case, we truncated f_U above 1024 Hz to improve performance since the detector noise curves make waveform contributions above these frequencies negligible. Since the used Virgo+ sensitivity curve starts from 10 Hz we discarded injections with $f_U < 11$ Hz which only affects the most massive BBHs at very large redshifts.

The performance metrics are chosen in order to assess the scientific capabilities of the Cosmic Explorer design at accomplishing specific science goals outlined in [122]. The raw data for a number of networks including the reference ones studied in this paper are available online (see Appendix B).

The accuracy of the 90%-credible sky area estimates from GWBENCH has been tested against the well-established BAYESTAR code [145] for BNS signals in Ref. [146]. Their findings suggest that the sky-localization estimates using Fisher analysis are trustworthy for a large population of events such as in this study. Indeed, they find that the agreement between Fisher and BAYESTAR for the 90%-credible sky area estimates improves strongly for larger SNR signals, see Fig. 2 in [146]: The GWBENCH and BAYESTAR estimates agree at 90th percentiles to within a factor ~ 6 and < 6 for signals with SNR of at least 15 and 25, respectively. Given that all well-localized events ($\Omega_{90} \leq 1\,{\rm deg}^2$) in our population, see Fig. 5, have SNRs $\rho \geq 30$ for BNSs (≥ 20 for BBHs), we believe our conclusions for the sky localization capabilities of the investigated networks to be well-justified for such events. Furthermore, we note that their test was performed for a three-detector network of lower sensitivity than the weakest network in our study (`HLVKI+`), while all but one (`VKI+C`) of our networks contain five detectors.

The GWBENCH package employs numerical inversion to calculate covariance matrices from Fisher information matrices. In particular, the code requires the condition number of a Fisher matrix—the fraction of its largest and smallest eigenvalue—to be less than 10^{15}, otherwise it discards the event from further analysis [147]. Such large condition numbers can occur for loud signals when two waveform parameters have vastly different error scales, making such events likely to be classified as ill-conditioned and hence discarded in our study. Consequently, the expected event numbers for signals in the high-SNR/well-measured tail of the population quoted throughout this paper should be regarded as conservative lower bounds. The exceptions are SNR statements and network efficiencies since a signal's SNR is calculated independently of its Fisher matrix.

III. MERGER AND DETECTION RATES: COMPACT BINARIES THROUGHOUT THE COSMOS

This section summarizes the assumptions and the essential elements of the simulations carried out in this study. We begin with a discussion of the response of a detector to an incident signal and the need to include the motion of the detector when computing the response. We then examine the efficiency of a network of detectors, which determines a network's detection rate, followed by a definition of the average and maximum distance up to which a network can observe compact binary coalescences. We conclude with the computation of detection rate as a function of redshift for different detector networks.

A. Detector response including its motion relative to a source

a. Antenna pattern Gravitational-wave detectors are quadrupole antennas and their sensitivity to sources has the same anisotropic response as that of a quadrupole (see, e.g., Ref. [148]) with the additional complication that GWs are metric perturbations with two independent polarizations h_+ and $h_\times$. The response of a GW detector to signals coming from a direction (α, δ) is [149–151]

$$
\begin{aligned}
h^{(A)}(t, \boldsymbol{\mu}) = {} & F_+^{(A)}(\alpha, \delta, \psi; R_A, \alpha_A, \beta_A, \gamma_A)\, h_+(t, \boldsymbol{\lambda}) \\
& + F_\times^{(A)}(\alpha, \delta, \psi; R_A, \alpha_A, \beta_A, \gamma_A)\, h_\times(t, \boldsymbol{\lambda}),
\end{aligned} \tag{1}
$$

where $F_+^{(A)}$ and $F_\times^{(A)}$ are the quadrupole antenna pattern functions of a detector indexed by A in the long-wavelength approximation (which is sufficiently accurate even in the case of NG detectors that will be tens of kilometers long, except for small corrections that might be needed at kilohertz frequencies), (α, δ) are the source's right ascension and declination in the geocentric coordinate system, ψ is the polarization angle, $(R_A, \alpha_A, \beta_A, \gamma_A)$ are the altitude, latitude, longitude, and the angle from local north to the x-arm of detector A, $\boldsymbol{\lambda} = \{\lambda_k\}$, $k = 1, \ldots, n_\lambda$, is the parameter vector describing the strain at the location of the detector and $\boldsymbol{\mu} = \{\mu_K\} = \{\alpha, \delta, \psi, \boldsymbol{\lambda}\}$, $K = 1, \ldots, n_\mu$, is the full parameter vector including the source's position in the sky and the polarization angle.

b. Strain parameters For a compact binary system on a quasi-circular inspiralling orbit, $\boldsymbol{\lambda}$ consists of the luminosity distance D_L to the source, the orientation of the orbit relative to the line-of-sight ι, the redshifted masses (m_1, m_2) and spins $(\boldsymbol{S}_1, \boldsymbol{S}_2)$ of the companions, the epoch of coalescence t_c taken to be the time when the amplitude of the response, which grows until the compact binary coalesces and then decays down rapidly, reaches its maximum value, and φ_c the phase of the signal at that epoch.

It is often convenient to use dimensionless spins $(\boldsymbol{\chi}_1, \boldsymbol{\chi}_2)$, which, in geometric units, are given by $(\boldsymbol{\chi}_1, \boldsymbol{\chi}_2) = (\boldsymbol{S}_1/m_1^2, \boldsymbol{S}_2/m_2^2)$. The magnitudes of the dimensionless spin vectors lies between $[0, 1]$. Likewise, in the post-Newtonian expansion of the waveform phase the chirpmass $\mathcal{M} = (m_1 m_2)^{3/5}/(m_1 + m_2)^{1/5}$ and symmetric mass ratio $\eta = m_1 m_2/(m_1 + m_2)^2$ appear more naturally than the component masses [152].

c. Time-dependent antenna pattern The position of the source in the sky is given in the geocentric coordinate system with respect to which the detector's position, described by angles $(\alpha_A(t), \beta_A(t))$, varies due to Earth's rotation. The relative motion of a detector with respect to a source induces amplitude modulation in the observed signal due to the changing antenna pattern functions in the direction of a source [153]. The value of the antenna pattern changes at most by a magnitude of order $\Delta h \sim |\sin(2\Delta\alpha)|$, where $\Delta\alpha$ is the change in the right ascension of the source relative to the detector; $\Delta h \sim 1$ over a six hour period. Since we can determine the amplitude of a signal to an accuracy of order $1/\rho$, where ρ is the SNR, the amplitude modulation could be important for signals that last

for more than ~ 30 minutes at an SNR of $\rho = 10$, and for even shorter periods for louder events. For signals that last for periods greater than 30 minutes, time-dependence of the response could further improve the localization of the source and is most relevant for BNS sources in ET.

d.   Detector location-dependent phase factor   In addition, a detector location-dependent phase factor should be included to account for the changing arrival times of the signal at the detectors relative to the geocentric coordinate system. This is accomplished by multiplying the Fourier transform of the response function $\tilde{h}(f)$ by the appropriate phase factor [153]:

$$\tilde{h}(f) \rightarrow \tilde{h}(f) \exp\left[\mathrm{i}2\pi f \frac{\boldsymbol{r}(t) \cdot \boldsymbol{n}(\alpha, \delta)}{c}\right],$$

where $\boldsymbol{r}(t)$ is the position vector of the detector on Earth, $\boldsymbol{n}$ is a unit vector in the direction of the source, and c is the speed of light. This phase factor is precisely what allows the triangulation of the source's sky position and is most effective when three or more non-collocated detectors are available.

e.   Frequency modulation   The frequency modulation due to Earth's rotation, however, is not important as the fractional change in frequency is expected to be negligible over the observation period of a signal: $\Delta f/f = v_{\mathrm{rot}}/c \ll 1/(f P_{\mathrm{max}})$, where $v_{\mathrm{rot}}/c = 1.5 \times 10^{-6}$ is Earth's rotational velocity at the equator, and P_{max} is the maximum duration for which a signal lasts in the detector's sensitivity bandwidth. P_{max} is the largest for BNS signals and varies from a few minutes to several hours depending on the lower-frequency cutoff $f \gtrsim 1\,\mathrm{Hz}$ of a detector below which contribution to the SNR of a signal is negligible. Thus, the change in frequency is not discernible for compact binary coalescence sources and frequency modulation can be neglected.

B.   Network efficiency

Having defined the response of a detector to a GW signal we next turn to defining the efficiency of a network of detectors, which would be required in computing the detection rate of a network. The *efficiency* $\epsilon(z)$ of a detector, or a network of detectors, at a given redshift or luminosity distance is defined as the fraction of all sources within that redshift for which the matched filter SNR ρ of the network is larger than a preset threshold ρ_*. To this end, the matched filter SNR ρ of a network of n_D detectors to an incident signal is defined as:

$$\rho^2 = \sum_{A=1}^{n_D} \rho_A^2, \quad \rho_A^2 = 4 \int_{f_L}^{f_U} \frac{\left|\tilde{h}^{(A)}(f)\right|^2}{S_h(f)}\, \mathrm{d}f, \qquad (2)$$

where $h^{(A)}$ is the response function of detectors $A = 1, \ldots, n_D$, given in Eq. (1), f_L and f_U are the detector- and signal-dependent lower and upper frequency cutoffs chosen so that there is negligible SNR outside that interval. The SNR depends on both the intrinsic and extrinsic parameters of the source: the source's masses and spins, distance, sky position, and orientation.

In order to compute the efficiency of a network at a given redshift z we inject signals in the interval z and $z + \mathrm{d}z$ with their intrinsic and extrinsic parameters distributed as in Tab. II

and count the number of sources for which the SNR was larger than ρ_*:

$$\epsilon(z, \rho_*) = \frac{1}{N_z} \sum_{k=1}^{N_z} \Pi(\rho_k - \rho_*), \quad \Pi(x) = \begin{cases} 0, & \text{if } x \leq 0 \\ 1, & \text{if } x > 0, \end{cases} \quad (3)$$

where N_z is the number of sources in the simulation in the redshift interval $[z, z + dz]$, ρ_k is the SNR of the kth event in the injection list, and $\Pi(x)$ is the Heaviside step function. We repeat this process from $z = 0.01$ to $z = 50$, thereby obtaining the efficiency curves shown in Fig. 2, top two panels, for different detector networks considered in this study. The well-known *sigmoid* functions with three parameters are a good fit to the efficiency curves

$$f_{\mathrm{sigmoid}} = \left(\frac{1+b}{1+b\,\mathrm{e}^{ax}}\right)^c. \qquad (4)$$

Appendix C lists the best-fit parameters a, b, and c for the various networks. Note that for a given source population the network efficiency depends only on the SNR threshold ρ_* and not how sources are distributed as a function of redshift. The detection rate of networks for a different source distribution than the one considered in this study can be computed using the efficiency curves provided here.

The network efficiency is plotted for two choices of the SNR threshold, $\rho_* = 10$ and $\rho_* = 100$. The lower value corresponds to the smallest SNR at which we assume a confident detection can be made by a detector network while the larger value is included to show redshift/distance from within which one can observe signals with high-fidelity. In Fig. 2, there are a pair of fitting lines with the same color for a given network but distinguished by circles for $\rho_* = 10$ and squares for $\rho_* = 100$, the one with greater efficiency corresponds to the lower ρ_*.

The network efficiency can be used to characterize the *completeness* of the survey of a detector network. For example, while the VK+HLIv network is 50% complete for BNS sources up to a redshift of $z \simeq 0.23$, the ECS network achieves 50% completeness up to a redshift of $z \simeq 2$, as can be seen from the top panels of Fig. 2 and Tab. III. Most remarkably, the ECS network will be almost 90% complete to BNS mergers within $z = 1$—the redshift limit up to which many current and future EM telescopes will have the ability to carry out follow-up observations of the mergers. Access to such a complete sample would help in understanding the physics and astrophysics of BNS mergers with little observational bias.

C.   The *reach* and *per-mille redshift* of a network

In the following, we refer to the *reach* z_r of a network as the redshift at which the detection efficiency is $\epsilon = 0.5$, which means the network is capable of detecting at least half of the source population at any redshift up to its reach at a threshold SNR ρ_*. Further, we present the *per-mille redshift* z_{pm} as the redshift for which the detection efficiency at the SNR threshold ρ_* drops to $\epsilon = 0.001$. This may be seen as a proxy for the networks' horizon redshift.

In Tab. III we provide the reach and per-mille redshift of all the networks for BNS and BBH mergers for two threshold
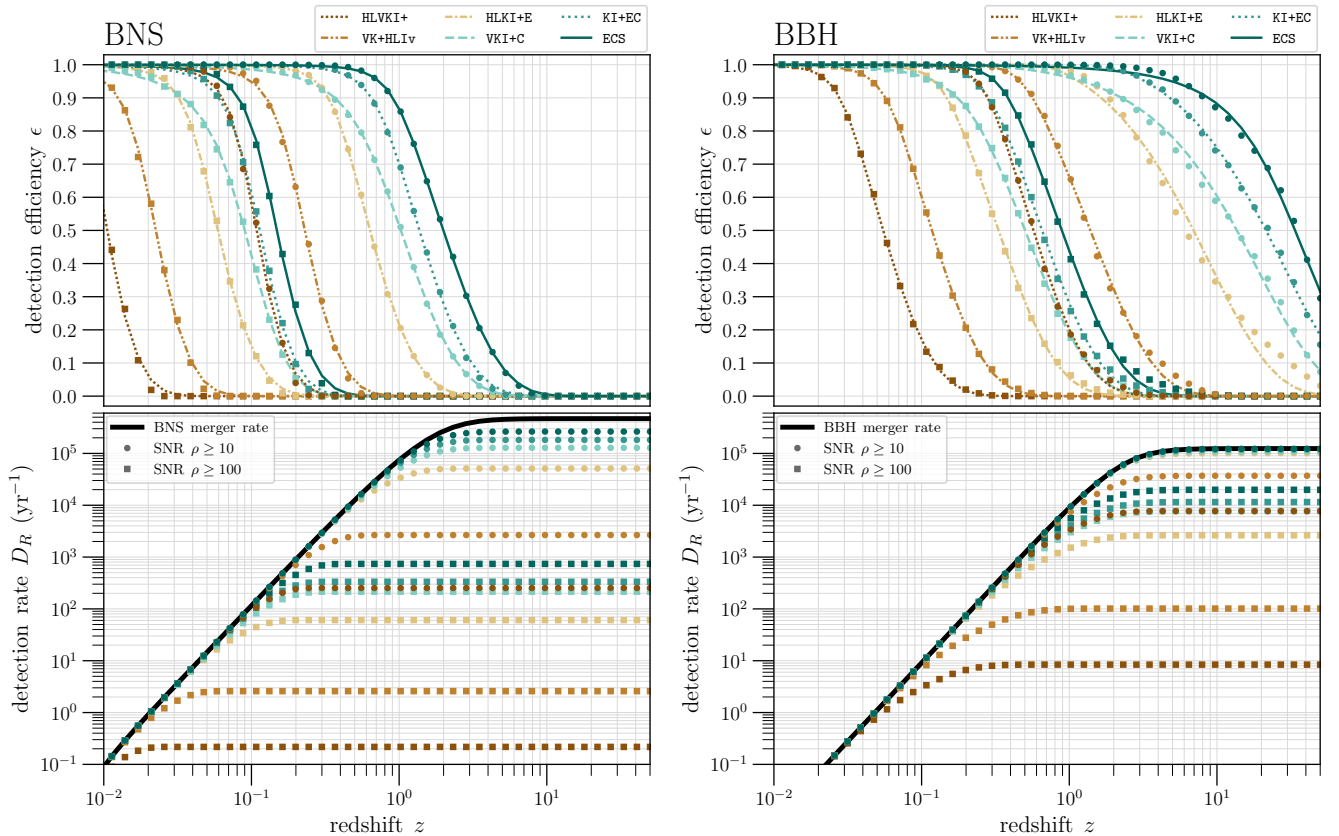
FIG. 2. Detection efficiencies ϵ and detection rates D_R, see Eqs. (3) and (9), respectively, of the six studied A+, Voyager, and NG networks are plotted as functions of redshift z. The efficiency specifies the value at the indicated redshift z while the detection rate corresponds to the integrated rate up to that redshift. The circles (squares) denote the values for events with SNR $\rho \geq 10$ ($\rho \geq 100$). The thick, black lines in the rate panels are the cosmic BNS and BBH merger rates, see Sec. III. The fit lines in the efficiency panels are sigmoid fits with $f_{\text{sigmoid}} = \left(\frac{1+b}{1+b\,e^{ax}} \right)^c$. The fit parameters for the curves are given in Appendix C.

SNR values: *detections* with $\rho \geq 10$ and exceptionally loud signals with $\rho \geq 100$. Note that the GW literature has many different definitions of the reach (see, e.g., Ref. [154]) which may not all agree with the one defined here.

D. Merger and detection rates

The merger rate of compact binaries in the local Universe comes from the first and second Gravitational-Wave Transient Catalogs GWTC-1 and GWTC-2 [6, 7]. They contain 2 BNS and 44 stellar-mass BBH mergers as enumerated in Tab. 1 of Ref. [134]. The inferred local merger rates (i.e. at redshift $z = 0$) were found to be $R_{\text{BNS}} = 320^{+490}_{-240}$ Gpc^{-3} yr^{-1} for BNS mergers and $R_{\text{BBH}} = 24^{+14}_{-7}$ Gpc^{-3} yr^{-1} for BBH mergers [18].

LIGO and Virgo rarely observe coalescences at cosmological distances (i.e. $z \gtrsim 0.5$) but future detectors will. Several factors affect the rate as a function of redshift. Following Ref. [155] we take into account three principal ones: (1) The rate at which stars form, (2) the delay between the formation of a compact binary and its merger, and, in the case of BBHs, (3) the variation of metallicity with redshift.

The star formation rate (SFR) $\psi(z)$ as a function of redshift is not known precisely but several phenomenological models are available capturing the observational uncertainty [156–159] (for a recent review see, e.g., Ref. [160]). The SFR initially increases as a function of redshift, peaking around $z \sim 2$, after which it falls off. We will take the compact binary formation rate, and hence the merger rate, to essentially follow the SFR except that there will be a delay t_d between the epoch t_f when a compact binary forms and the epoch when it merges. Furthermore, the merger rate is calibrated by demanding its local value at $z = 0$ to be consistent with the merger rate determined by LIGO and Virgo observations given above. Finally, metallicity plays a crucial role in the formation of BHs due to its effect on stellar winds, which must be folded into the calculation of rates. In addition, we must be mindful of the fact that the cosmological volume element (dV/dz) corresponding to a redshift interval dz is itself a function of redshift due to the Hubble expansion and the Universe was smaller at earlier times.

Compact binaries that form at redshift z_f merge at redshift z after a delay time t_d (see, e.g., Ref. [161, 162]). For a given redshift z and delay t_d the redshift when the binary forms can be found by solving

$$t_d - \frac{1}{H_0} \int_z^{z_f} \frac{dz'}{(1+z')E(z')} = 0, \quad E(z') = \left[\Omega_\Lambda + \Omega_M (1+z')^3 \right],$$

(5)

where Ω_M and Ω_Λ are the dark matter and dark energy densi-

ties and we have assumed a flat Universe in which dark energy is interpreted as a cosmological constant [163]. The delay time is not the same for all binaries and depends on the configuration of the compact binary when it forms and is modelled by a probability density $P(t_d)$. The merger rate density $\dot{n}(z)$ (normally computed in units of Gpc^{-3} yr^{-1}) in the source's frame is obtained by integrating the SFR over all possible time delays,

$$\dot{n}(z) = A \int_{t_d^{\min}}^{t_d^{\max}} \psi(z_f(z, t_d)) \, P(t_d) \, dt_d, \tag{6}$$

where $t_d^{\min}$ and $t_d^{\max}$ denote the smallest and largest possible time delays and the normalization constant A is chosen so that local rate $\dot{n}(0)$ is consistent with the rate inferred using the GWTC-2 catalog [134]: $\dot{n}_{\text{BNS}}(0) = 320 \, \text{Gpc}^{-3}\text{yr}^{-1}$ and $\dot{n}_{\text{BBH}}(0) = 23 \, \text{Gpc}^{-3}\text{yr}^{-1}$, where we have taken the central value of the rate posteriors ignoring the measurement uncertainties.

The delay-time distribution is not very well known but could be inferred accurately from future observations [164–166]. As is customary, we take $P(t_d)$ to be Jeffry's prior $P(t_d) \propto 1/t_d$ [161]. With normalization it becomes

$$P(t_d) = \frac{1}{\ln\left(t_d^{\max}/t_d^{\min}\right) t_d}. \tag{7}$$

For this prior, most of the contribution to the density comes from near $t_d^{\min}$ which we set to be $t_d^{\min} = 20 \, \text{Myr}$ for BNS and $t_d^{\min} = 10 \, \text{Myr}$ for BBH mergers. We take $t_d^{\max} = 10 \, \text{Gyr}$ in both cases.

From the merger rate density $\dot{n}(z)$ one computes the merger rate per redshift bin using

$$R(z) = \dot{n}(z) \frac{dV}{dz} \tag{8}$$

where $dV(z)/dz$ is the comoving volume element. An observer in the local Universe would measure the rate of mergers to be a factor $(1 + z)$ smaller than in the source's frame, i.e. $R_{\text{obs}}(z) = R(z)/(1 + z)$.

SNR ρ	BNS				BBH			
	≥ 10		≥ 100		≥ 10		≥ 100	
	z_r	z_{pm}	z_r	z_{pm}	z_r	z_{pm}	z_r	z_{pm}
HLVKI+	0.11	0.39	0.01	0.04	0.57	3.5	0.05	0.31
VK+HLIv	0.23	0.92	0.02	0.09	1.4	10	0.12	0.7
HLKI+E	0.63	3.3	0.06	0.27	7	> 50	0.33	2.2
VKI+C	1	6.6	0.09	0.39	14	> 50	0.5	3.6
KI+EC	1.4	8	0.11	0.44	21	> 50	0.65	4.3
ECS	2	13	0.15	0.59	34	> 50	0.89	6.1

TABLE III. The reach z_r and per-mille redshift z_{pm} of the considered networks for BNS and BBH signals with SNRs $\rho \geq 10$ or $\rho \geq 100$. Here we define the reach (per-mille redshift) as the redshift at which a given network detects 50% (0.1%) of the injections with the specified SNR or louder. Please refer to the detection efficiency panels of Fig. 2 for a visual representation.

A network of detectors, however, would not observe all the mergers that would occur at a given redshift but only a fraction $\epsilon(z, \rho_*)$ determined by the network's efficiency given in Eq. (3), which in turn depends on the SNR threshold ρ_*. Thus, the detection rate, i.e. the number of detections per year, $D_R(z, \rho_*)$ observed up to redshift z is given by:

$$D_R(z, \rho_*) = \int_0^z \epsilon(z', \rho_*) \frac{\dot{n}(z')}{(1 + z')} \frac{dV(z')}{dz'} \, dz'. \tag{9}$$

The BBH merger rate was chosen to follow the 'Madau-Dickinson-Belczynski-Ng' rate for field BHs described in [167]. For the BNS population we take the SFR to be that of Madau-Dickinson but neglect the effect of metallicity evolution as this is not as important for the formation of NSs.

The bottom panels of Fig. 2 plot the detection rate D_R as a function of redshift for two choices of the threshold: $\rho_* = 10$ and $\rho_* = 100$. We will discuss the distributions of SNR and measurement error estimates in the next section.

IV. VISIBILITY AND MEASUREMENT QUALITY OF COMPACT BINARY MERGERS IN FUTURE DETECTORS

In the following we summarize the overall capabilities of the six detector networks for the BNS and BBH populations throughout the chosen redshift range $z \in [0.02, 50]$. As such we will make 'full-population' statements for the expected detection rates that each network should achieve given a set of targets for the performance metrics specified below.

Figs. 3 and 4 present cumulative histograms for six performance metrics: SNR ρ, 90%-credible sky area Ω_{90}, fractional errors on chirpmass $\Delta\mathcal{M}/\mathcal{M}$ and luminosity distance $\Delta D_L/D_L$, and absolute errors on symmetric mass ratio $\Delta\eta$ and inclination angle $\Delta\iota$. Fig. 3 summarizes the BNS injections, while Fig. 4 shows the results for the BBHs. In both cases, the cumulative histograms present the *relevant* data from the 1.5 million injections that were simulated in the redshift range and are shown to the 0.01%-level. Here, *relevant* data refers to (i) the entire injection set in the case of the SNR sub panel, with $(\rho < 1)$-events truncated, and (ii) the detectable events with $\rho \geq 10$ for the remaining metrics. We show the respective histograms in Appendix D.

A. Incorporation of redshift-dependent merger rates

While the uniform sampling per redshift bin provides us with good parameter sampling, it also means that we need to scale the probability density functions of the populations to capture the redshift-dependent merger rates as discussed in the previous section. For this purpose we divide the redshift range in $N = 150$ sub-bins, containing each $n_i \approx 10,000$ injections. Each sub-bin has an associated merger rate R_i, $i = 1, \ldots, N$ computed following Sec. III, allowing us to define sub-bin probabilities as $p_i = R_i/R$ with $R = \sum_{i=1}^{N} R_i$. We then sample the N sub-bin indices i with probabilities p_i up to the desired number of BNS and BBH mergers, e.g. corresponding to 10 years of mergers, thus providing us with a number of samples n_i for each index i. Finally, we uniformly sample n_i injections
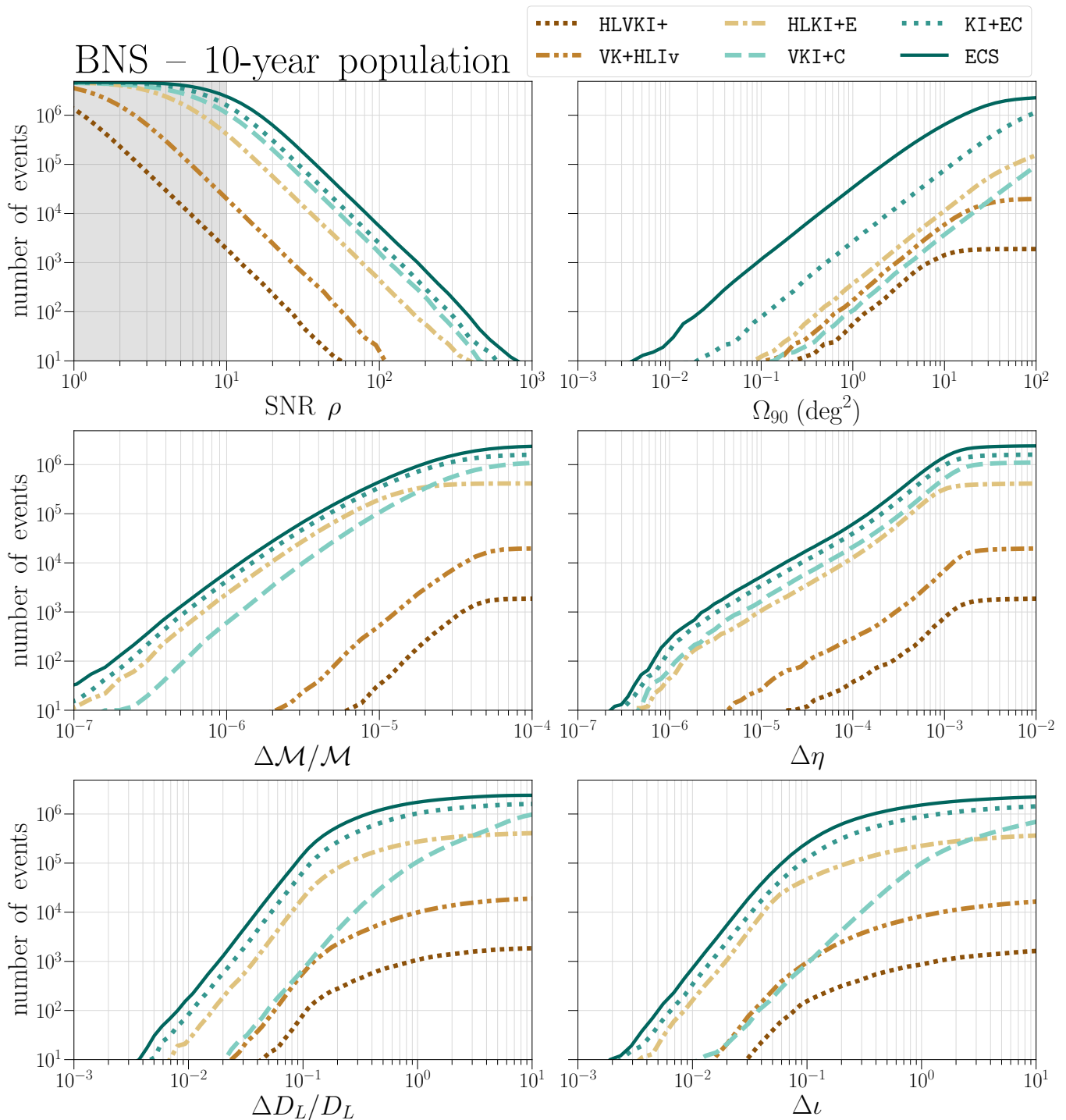
FIG. 3. Cumulative histograms for the SNR ρ, 90%-credible sky area Ω_{90}, fractional errors on chripmass $\Delta\mathcal{M}/\mathcal{M}$ and luminosity distance $\Delta D_L/D_L$, and absolute errors on symmetric mass ratio $\Delta\eta$ and inclination angle $\Delta\iota$ for BNS mergers observed in the six studied A+, Voyager, and NG networks. The histograms were generated from $\sim 4.7 \times 10^6$ injections sampled according to Sec. IV A. The non-SNR panels are obtained for events with SNR $\rho \geq 10$, indicated by the non-shaded region in the SNR panel. The SNR panel is flipped to highlight the behavior for large values.

from the simulated BNS and BBH mergers in the i-th sub-bin, thus resulting in a random sample of injections in each sub-bin with the desired total number of mergers in the total redshift range.

In order to mitigate sampling effects in the distribution tails

we perform all analyses using a **10-year random sample** of BNS and BBH mergers drawn from the simulated populations at the corresponding cosmic merger rates for the redshift range of interest. We show these 10-year samples in all histograms and scatter plots throughout this paper to better represent what
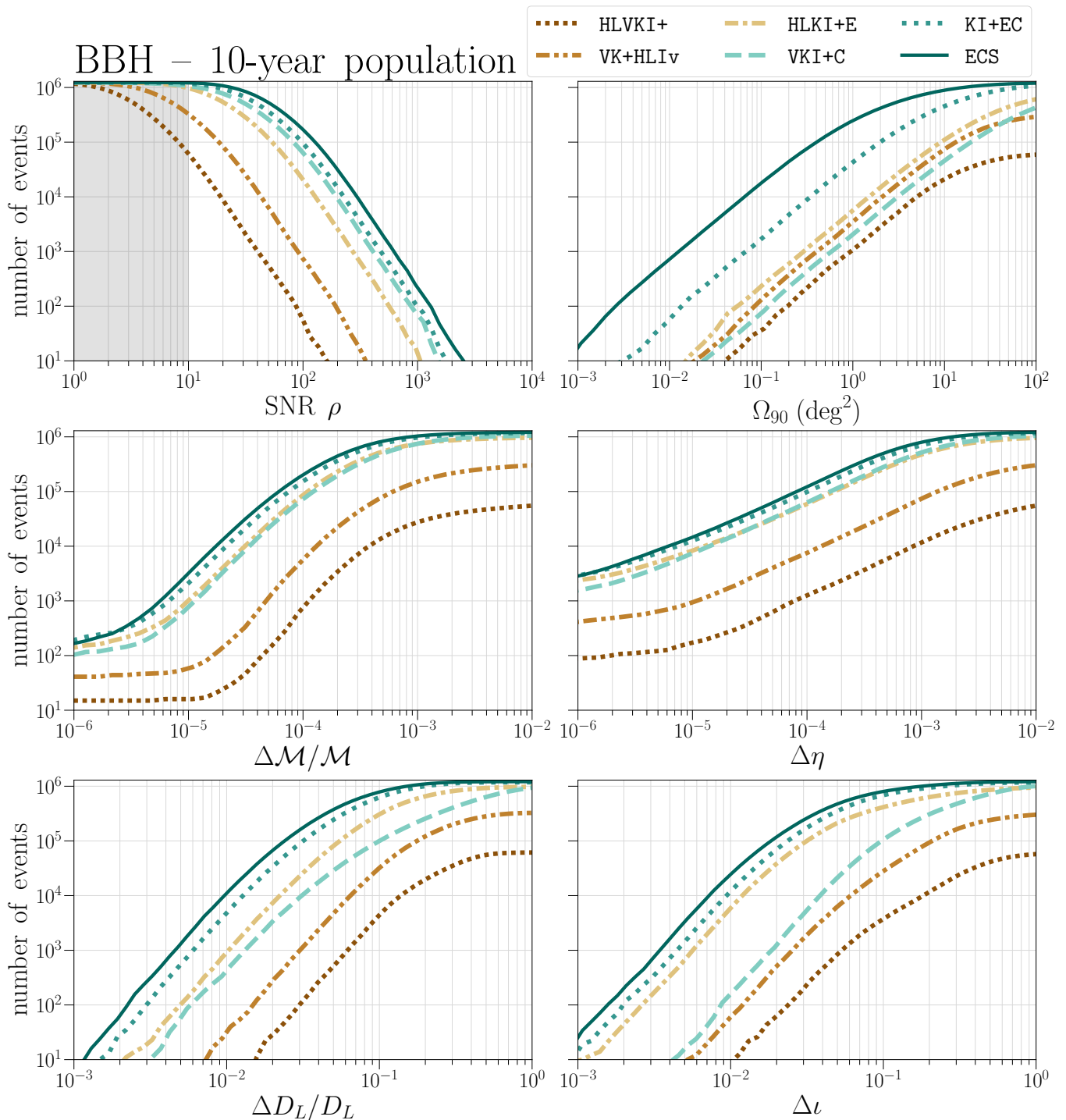
FIG. 4. Cumulative histograms for the SNR ρ, 90%-credible sky area Ω_{90}, fractional errors on chripmass $\Delta\mathcal{M}/\mathcal{M}$ and luminosity distance $\Delta D_L/D_L$, and absolute errors on symmetric mass ratio $\Delta\eta$ and inclination angle $\Delta\iota$ for BBH mergers observed in the six studied A+, Voyager, and NG networks. The histograms were generated from $\sim 1.2 \times 10^6$ injections sampled according to Sec. IV A. The non-SNR panels are obtained for events with SNR $\rho \geq 10$, indicated by the non-shaded region in the SNR panel. The SNR panel is flipped to highlight the behavior for large values.

each network is statistically capable to achieve and we mention this again in the captions of the respective figures. Similarly, all presented cumulative histograms are calculated from these larger samples to improve the statistics. In contrast, **we cite yearly detections rates** for the studied networks both in the

text and tables, in order to represent rates for a time-scale more akin to the observing runs of the LIGO and Virgo detectors.

B. Signal visibility

The cosmic merger rate of BNS is of the order of 4.7×10^5 per year, but depending on the network we can only expect completeness as low as $\sim 0.04\%$ in HLVKI+ and $\sim 0.4\%$ in VK+HLIv, but up to $\sim 50\%$ with three NG detectors (ECS), translating to $O(10^2)$, $O(10^3)$, and up to $O(10^5)$ BNS detections per year, respectively, summarized in Tab. IV. These raw numbers illustrate the stark difference in volume and corresponding merger rates that each network's reach encompasses: $z_r \sim 0.11$ for HLVKI+, $z_r \sim 0.23$ for VK+HLIv, and $z_r \sim 2$ for ECS (see Fig. 2 and Tab. III). Further, Tab. IV indicates that we can expect a host of BNS events in the 'GW170817-class' with SNRs $\rho \geq 30$, while SNR values above 100 are only regularly observable in NG networks. In fact, the NG networks containing a CE detector will observe such loud events at rates of the order 1/10 to 1/4 of *all* yearly BNS detections in the Voyager network.

TABLE IV. Cosmic merger rates (per year) of BNS and BBH mergers in the Universe and the number that would be observed by different detector networks each year with $\rho \geq 10, 30, 100$, where ρ is the SNR ratio. Due to uncertainty in the various quantities that go into the calculation these numbers are no more accurate than one or two significant figures.

	BNS			BBH		
Cosmic rate	4.7×10^5			1.2×10^5		
SNR ρ	≥ 10	≥ 30	≥ 100	≥ 10	≥ 30	≥ 100
HLVKI+	190	6	1	6,100	240	6
VK+HLIv	2,000	71	2	33,000	2,900	74
HLKI+E	41,000	1,700	45	97,000	31,000	2,100
VKI+C	110,000	6,000	160	110,000	53,000	6,400
KI+EC	160,000	9,400	250	120,000	69,000	9,500
ECS	240,000	20,000	550	120,000	87,000	17,000

The picture for BBH mergers, see the SNR panel of Fig. 4 and Tab. IV, is less skewed in favor of the NG networks in comparison to the Voyager network since its redshift reach $z_r \sim$ 1.4 extends into the peak of the Madau-Dickinson-Belczynski-Ng merger rate density; see [167]: Both HLVKI+ and VK+HLIv will detect $O(10^3)$ and $O(10^4)$ BBH mergers per year with completeness of 5% and 28%, respectively, while the NG networks will observe $O(10^5)$ BBH mergers with completeness between 81% (HLKI+E) and 99% (ECS). In fact, all considered networks will detect BBH coalescences with SNRs above 100 albeit at per-mille redshifts of $z_{pm} \sim 0.31, 0.7$, and up to 6.1 for HLVKI+, VK+HLIv, and ECS, respectively, and corresponding reaches of $z_r \sim 0.05, 0.12$, and 0.89. Hence, the difference between these networks comes down to the NG networks' reach for BBHs extending beyond redshift 7 (or even 14 with at least one CE detector) and the resulting completeness of the observable population at high redshifts: KI+EC and ECS will detect essentially all BBH signals at the cosmic merger rate of $\sim 1.2 \times 10^5 \text{ yr}^{-1}$.

While the yearly rates for all six networks far exceed the number of events observed with the current generation of detectors [6, 7], the differences between these future networks are still crucial in their impact for astrophysics, cosmology,

tests of GR, and dense matter physics. Fig. 5 captures these differences and presents what signal loudness and sky localization distributions to expect for GW observations from the studied networks throughout the redshift range over 10 years of observations.

Only NG networks will deliver an abundance of exceptionally loud BNS signals with SNRs above 100; even to cosmological distances of $z \lesssim 0.4$. Such events will allow us to probe the nuclear physics with high fidelity, constrain the dense-matter equation of state, and explore the BNS post-inspiral signal.

For both the BNS and BBH coalescences the differences in reach and per-mille redshifts, see Tab. III, imply that not only a larger, but also older part of the BNS and BBH populations can be studied with NG networks. Especially, KI+EC and ECS will observe almost all BNS and BBH mergers up to luminosity distances of $\lesssim 2 \text{ Gpc}$ and $\lesssim 25 \text{ Gpc}$, respectively. Their per-mille redshifts lie at $z_{pm} \gtrsim 8$ for BNSs and beyond 50 for BBHs, in contrast to the Voyager network with $z_{pm} \sim 0.9$ and $z_{pm} \sim 9.7$, respectively. This means that a NG network could observe BNS coalescences from roughly 500 Myr and BBH mergers from less than 50 Myr after the Big Bang, thus expanding their observational potential deep into the realm of the dark ages! While the expectations for mergers in this regime are very low, population III stars and primordial BHs could pose potential progenitor and source systems, to which all networks other than NG would be blind.

TABLE V. Detection rates of BNS and BBH mergers from the full redshift range $z \in [0.02, 50]$ to be observed by different detector networks each year with $\Omega_{90}/\text{deg}^2 \leq 1, 0.1, 0.01$ as well as $\Delta D_L/D_L \leq 0.1, 0.1$, where Ω_{90} is the 90%-credible sky area and D_L the luminosity distance. These detection rates are calculated for events with SNR $\rho \geq 10$. Due to uncertainty in the various quantities that go into the calculation these numbers are no more accurate than one or two significant figures.

Metric	Ω_{90} (deg^2)			$\Delta D_L/D_L$	
Quality	≤ 1	≤ 0.1	≤ 0.01	≤ 0.1	≤ 0.01
			BNS		
HLVKI+	5	1	0	8	0
VK+HLIv	17	1	0	58	0
HLKI+E	37	1	0	1,900	3
VKI+C	11	1	0	67	0
KI+EC	270	8	0	6,600	8
ECS	3,400	120	3	15,000	18
			BBH		
HLVKI+	110	4	0	440	0
VK+HLIv	350	13	0	3,200	3
HLKI+E	560	23	1	31,000	92
VKI+C	210	8	0	10,000	45
KI+EC	4,400	170	6	64,000	490
ECS	24,000	1,800	72	78,000	1,100

Lastly, the shear abundance of loud events up to far redshifts will further enable astronomers and cosmologists to better understand source population demographics as well as trace and correlate the large-scale structure of the Universe with these mergers. Louder and more abundant signals will be a

treasure trove for tests of GR which benefit from the outright signal strengths but also the potential of signal binning. We examine rare, extremely loud signals with SNRs $\rho \gtrsim 300$ in Sec. VI.

C. Measurement quality

The three-dimensional localization of a source, on the sky and in luminosity distance, is crucial in enabling a multitude of science, especially for BNS mergers which can exhibit observable electromagnetic (EM) counterparts. Hence, we summarize the expected detection rates of events with 90%-credible sky area $\Omega_{90}/\deg^2 \leq 0.01, 0.1, 1$ and fractional luminosity distance errors $\Delta D_L/D_L \leq 0.01, 0.1$ in Tab. V. The visual representations in form of cumulative histograms can be found in the Ω_{90}- and $\Delta D_L/D_L$-panels of Fig. 3. We will further expand our examination of the potential to enable multi-messenger astronomy at redshifts $z \leq 0.5$ in Sec. V.

GW190814 [18] is the best-localized, observed GW event so far, with a 90%-credible sky area of $19 \deg^2$ and a luminosity distance error of about 19%. In comparison, both HLVKI+ and VK+HLIv will detect $O(1)$ to $O(10)$ BNS sources per year with sky areas below $1 \deg^2$ and 10% luminosity distance errors, with BBH-numbers being ~ 20 (sky area) or ~ 50 (distance errors) times larger. HLVKI+ and VK+HLIv will further be capable to observe annually $O(1)$ BNS and $O(1)$ to $O(10)$ BBH mergers, respectively, with sky areas below $0.1 \deg^2$.

The picture for the NG networks is distinctly different than it was for the signal visibility. Since these networks differ in the number of NG detectors per network with one in HLKI+E and VKI+C, two in KI+EC, and three in ECS and since sky localization and luminosity distance measurements improve dramatically with more detectors in a network, the number of more sensitive NG detectors has a strong effect on the measurement quality. This is illustrated by the increase of green-colored points in the KI+EC and ECS panels of Fig. 5, indicating their improved sky localization capabilities.

Consequently, these networks will detect BNS coalescences localized to within a 90%-credible sky area smaller than $(1, 0.1) \deg^2$ on the order of $(O(10), O(1))$ per year in HLKI+E and VKI+C, $(O(10^2), O(1))$ per year in KI+EC, and $(O(10^3), O(10^2))$ per year in ECS, with the latter being the only network to observe a handful of BNS per year with $\Omega_{90} \leq 0.01 \deg^2$. Furthermore, fractional luminosity distance errors smaller than $(0.1, 0.01)$ will be observed at rates of the order $(O(10), O(0))$ per year in VKI+C, $(O(10^3), O(1))$ per year in HLKI+E and KI+EC, and $(O(10^4), O(10))$ per year in ECS. The rates for BBHs are approximately one order of magnitude larger per year $(\lesssim 20\times)$, if permitted by the cosmic merger rates. The notable exceptions are that VKI+C will measure the luminosity distance of $O(10^4)$ $(\sim 150\times)$ while all NG networks observe $\sim$ 30–60 times more BBH than BNS mergers per year down to sub-1% accuracies in luminosity distance. Finally, while KI+EC will be able to pin-point some BBH mergers to within $\Omega_{90} \leq 0.01 \deg^2$, only ECS will be capable to do so for BNS mergers as well.

The sky localization capabilities of all networks, but VKI+C, scale with the networks' sensitivities (Tab. IV). In contrast, while VKI+C observes significantly more events than the Voy-

ager network VK+HLIv, if not limited by the cosmic merger rate (e.g. 80 times the number of BNS and BBH mergers with $\rho \geq 100$), both networks perform roughly equally in terms of sky localization. This is a clear indication of the importance of both the number of detectors in a network and their sensitivity. With only four detector sites and only one detector beyond the A+ generation, VKI+C's sky localization capabilities cannot surpass a network of five detectors, three of which operating at Voyager sensitivities. Ultimately, it performs equally due to its farther reach and thus larger base detection rate. In Appendix E we examine the differences between networks with four different CE configurations: i) a single 20 km arm length, ii) the same single 40 km arm length as in VKI+C, iii) two CEs with 20 and 40 km arm lengths, and iv) two CEs with 40 km arm lengths.

As was mentioned above, the three-dimensional localization of a GW source is extremely important for BNS coalescences which exhibit EM counterparts, such as the gamma-ray burst GRB 170817A and kilonova AT2017gfo associated with the GW event GW170817 [12]. Unfortunately, such coincident detections with bright, EM transients like GRBs, require the emission of the burst in our direction while being in the field-of-view (FOV) of operating telescopes. Thus, if this initial pointer is missed or poorly localized, the EM follow-up will be hampered. As such the second BNS event GW190425, observed by the LIGO and Virgo detectors, did not appear to have a coincident gamma-ray burst, its location was not determined, and the potential counterpart was not studied in the EM spectrum.

If the GW signal itself already were to point to the source, by pin-pointing the sky location to within a 90%-credible sky area that telescopes can quickly survey, a strong, coincident EM would not be required to find the fainter counterpart. Further, the identification of the signal's host galaxy allows the astronomy community to improve their surveys of the Universe's large-scale structure both locally but also in the distant Universe with BBHs. Besides, measurements of the host's redshift in conjunction with an accurate estimate of the luminosity distance from the GW signal could enable high-fidelity measurements of the Hubble constant in the local Universe to the level needed to resolve the Hubble-Lemaître tension with a single compact binary coalescence [80]. We examine the potential of the chosen networks in enabling multi-messenger astronomy in the next section.

V. ENABLING MULTI-MESSENGER ASTRONOMY

The EM follow-up campaign of the BNS event GW170817 [12] resulted in the identification of the counterpart and observation of the afterglow in the entire EM spectrum, providing a treasure trove of data that has impacted several areas in fundamental physics [13, 54, 55, 75, 76], astrophysics [13, 65–74] and cosmology [48, 77]. As such the synergy of GW and EM observations of compact binary coalescences in the readily EM-observable Universe, $z \leq 0.5$, will be of paramount importance in the coming decades. In this section we examine how well each network will localize BNS and BBH mergers at redshifts $z \leq 0.5$ in the GW window enabling the potential for EM follow-up irrespective of a loud EM transient such
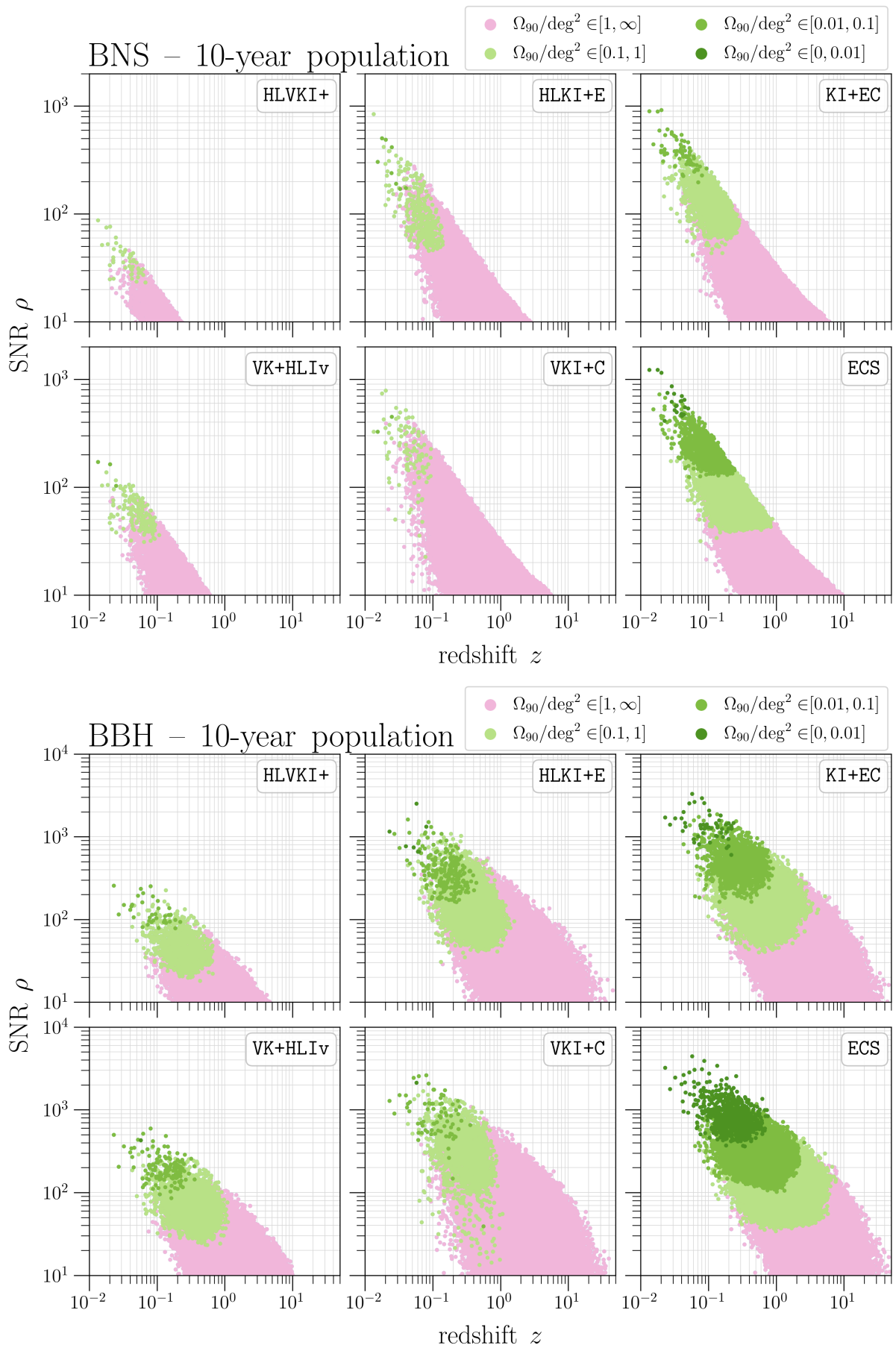
FIG. 5. The scatter plots illustrate the correlations between redshift z, SNR ρ, and 90%-credible sky area Ω_{90} for BNS (*top*) and BBH (*bottom*) mergers in the six studied A+, Voyager, and NG networks.

as a gamma-ray burst. Further, we illustrate each network's capabilities for early warning of BNS mergers, i.e. both the detection and sky localization of a compact binary during the inspiral ahead of the merger.

Tab. VI presents the FOVs for 13 current or planned EM telescopes that have the capability to slew and follow-up GW detections. When considering these FOVs it is important to remember that they represent the sky area the respective telescope can observe without any tiling: It is not uncommon for EM telescope to observe larger FOVs during a follow-up campaign by tiling the search region with up to ~ 10 segments.

TABLE VI. Field-of-views (FOVs) for various electromagnetic telescopes.

EM telescope	FOV (deg^2)
Rubin Observatory [168]	9.6
EUCLID [169]	0.54
Athena [170]	0.35
Nancy Roman Grace Space Telescope [171]	0.28
Chandra X-ray Observatory [172]	0.15
Lynx [173]	0.134
Swift–XRT [174]	0.12
30 m-Telescope [175]	0.11
Keck [176]	0.11
VLT [177]	0.054
ELT [178]	0.028
GMT [179]	0.008
HST–WFC3 [180]	0.002

A. Three-dimensional localization

The localization of the GW signal's sky position is the key metric governing the feasibility of a follow-up campaign with EM telescopes. Additionally, GW observations can provide accurate distance measurements that are independent of the cosmic distance-ladder calibration issues and can help distinguish between a number of potential hosts [181]. Finally, the visibility of certain EM phenomena such as gamma-ray bursts and jets depends on the binary's orientation with respect to the observer's line of sight. Thus, in this section we present the potential of the chosen networks to measure these metrics in form of the SNR, 90%-credible sky area, as well as luminosity distance and inclination angle errors for GW signals at redshifts $z \leq 0.5$.

Fig. 6 presents the distribution and correlation of SNR ρ, sky area Ω_{90}, and fractional luminosity distance error $\Delta D_L/D_L$ for BNS signals as well as the cumulative histograms for all four metrics, including absolute errors on the inclination angle ι. We also summarize the expected detection rates of events with 90%-credible sky area $\Omega_{90}/\mathrm{deg}^2 \leq 0.01, 0.1, 1$ and fractional luminosity distance errors $\Delta D_L/D_L \leq 0.01, 0.1$ in Tab. VII.

The cosmic merger rate for BNSs up to redshift $z \leq 0.5$ is approximately 12,000 per year. The top part of Fig. 6 and Tab. VII indicate that networks containing less than two *distinct* NG detector sites (HLVKI+, VK+HLIv, HLKI+E, and VKI+C) will

localize, if at all, rare, *golden*[1] BNS signals ($\lesssim$ 1 per year) to within $\Omega_{90} \leq 0.1\,\mathrm{deg}^2$. Luminosity distances should be measured to better than 10% accuracy $O(1)$ (HLVKI+), $O(10)$ (VK+HLIv, VKI+C), and $O(10^3)$ (HLKI+E) per year; and only HLKI+E will be capable to consistently observe a few golden events per year to sub-1% accuracy. The discrepancy between the NG networks HLKI+E and VKI+C stems from the sub-10 Hz sensitivity of ET and its ability to measure both polarizations by itself. KI+EC and ECS with two and three NG sites will determine the sky positions of a few or ~ 100 BNS mergers per year to $\leq 0.1\,\mathrm{deg}^2$, respectively, and measure the luminosity distance of $O(10)$ events per year to sub-1% accuracies. Ultimately, ECS is the only network to consistently localize golden BNS mergers to within $\Omega_{90} \leq 0.01\,\mathrm{deg}^2$. In fact, the scatter plot in Fig. 6 indicates most of these observations will come with a sub-10% accuracy in the luminosity distance while a few golden events will push it down below 1%.

TABLE VII. Detection rates of BNS and BBH mergers up to redshift $z = 0.5$ to be observed by different detector networks each year with $\Omega_{90}/\mathrm{deg}^2 \leq 1, 0.1, 0.01$ as well as $\Delta D_L/D_L \leq 0.1, 0.1$, where Ω_{90} is the 90%-credible sky area and D_L the luminosity distance. These detection rates are calculated for events with SNR $\rho \geq 10$. Due to uncertainty in the various quantities that go into the calculation these numbers are no more accurate than one or two significant figures. The bare merger rates for BNSs and BBHs up to redshift $z = 0.5$ are ~ 12,000 yr^{-1} and ~ 1,200 yr^{-1}, respectively.

Metric	Ω_{90} (deg^2)			$\Delta D_L/D_L$	
Quality	≤ 1	≤ 0.1	≤ 0.01	≤ 0.1	≤ 0.01
BNS					
HLVKI+	5	0	0	8	0
VK+HLIv	16	1	0	56	0
HLKI+E	36	1	0	1,800	2
VKI+C	10	1	0	56	0
KI+EC	260	8	0	4,100	8
ECS	2,800	110	2	5,600	17
BBH					
HLVKI+	100	4	0	210	0
VK+HLIv	270	14	0	560	3
HLKI+E	350	23	1	1,100	72
VKI+C	180	8	0	550	21
KI+EC	870	150	6	1,200	200
ECS	1,100	580	69	1,200	320

While BNS mergers are the headlight events for multi-messenger astronomy, sparked by GW170817 and expected EM counterparts, the EM follow-up of BBH coalescences is equally intriguing, especially since astrophysicists want to explore the unclear origins of the massive BBHs LIGO and Virgo have observed so far. As such, Fig. 7 and Tab. VII summarize the potential for multi-messenger astronomy with BBHs up to redshift $z = 0.5$. With a cosmic merger rate of only 1,200

---

[1] We refer to uncommonly rare events with high measurement fidelity at rates below 3 per year as *golden*.
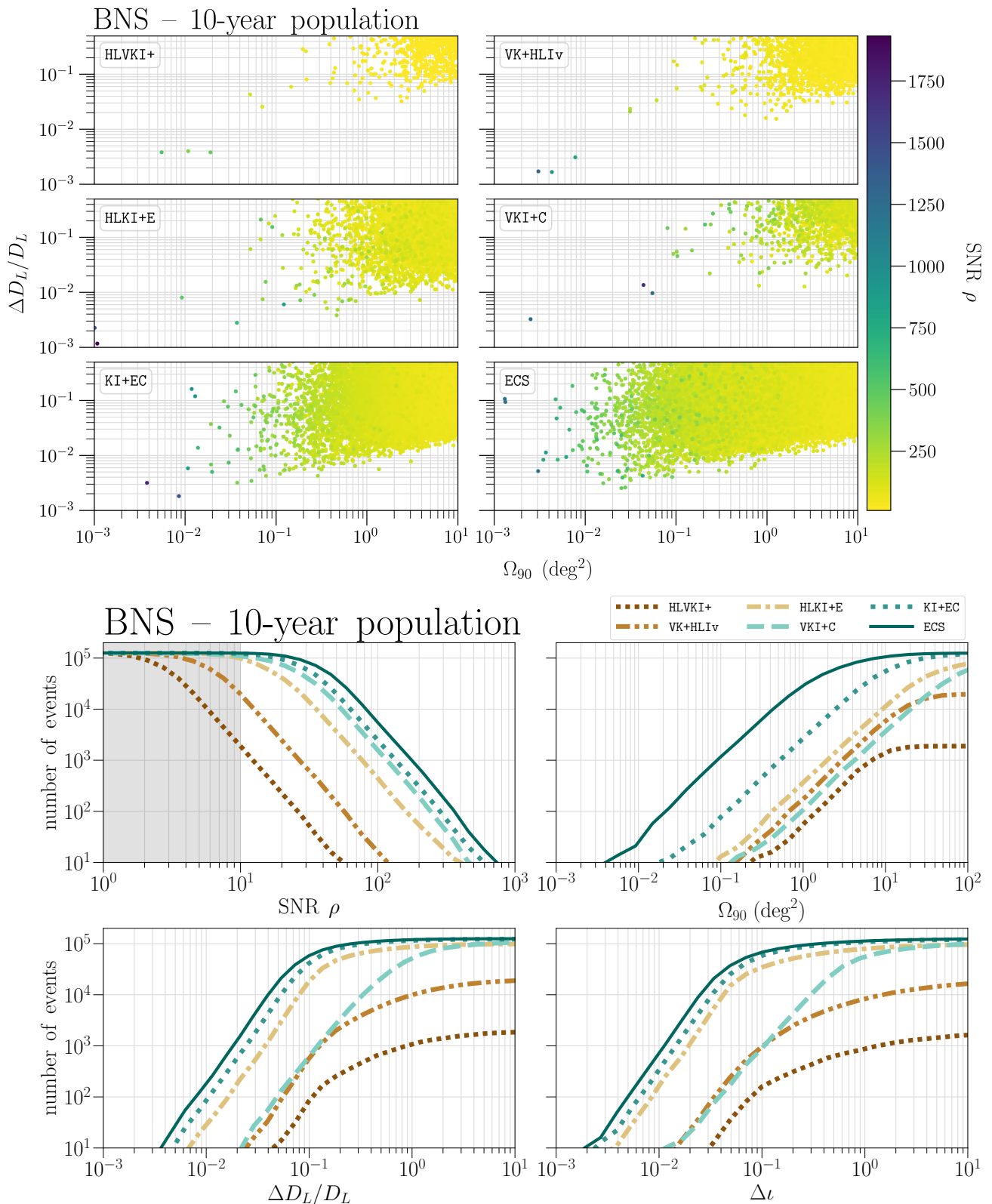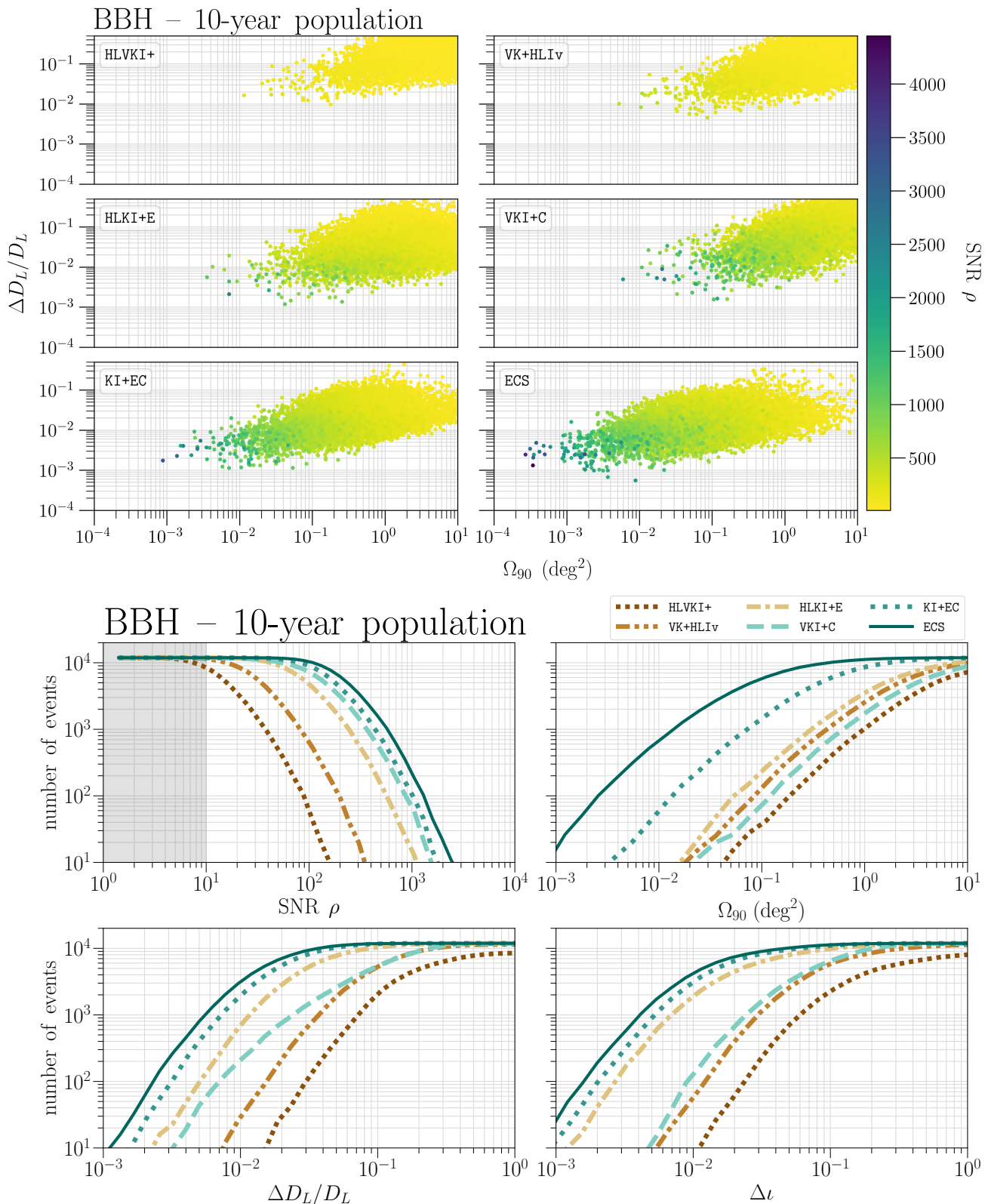
15

FIG. 6. *Top*: The scatter plots illustrate the correlations between SNR ρ, 90%-credible sky area Ω_{90}, and fractional luminosity distance error $\Delta D_L/D_L$ for BNS mergers with SNR $\rho \geq 10$ in the six studied A+, Voyager, and NG networks for redshifts $z \leq 0.5$. The color bar indicates the SNR of the events.
Bottom: Cumulative histograms for the SNR ρ, 90%-credible sky area Ω_{90}, fractional luminosity distance errors $\Delta D_L/D_L$, and absolute errors the inclination angle $\Delta \iota$ for BNS mergers observed in the six studied A+, Voyager, and NG networks for redshifts $z \leq 0.5$. The histograms were generated from $\sim 1.2 \times 10^5$ injections sampled according to Sec. IV A. The non-SNR panels are obtained for events with SNR $\rho \geq 10$, indicated by the non-shaded region in the SNR panel. The SNR panel is flipped to highlight the behavior for large values.

FIG. 7. *Top*: The scatter plots illustrate the correlations between SNR ρ, 90%-credible sky area Ω_{90}, and fractional luminosity distance error $\Delta D_L/D_L$ for BBH mergers with SNR $\rho \geq 10$ in the six studied A+, Voyager, and NG networks for redshifts $z \leq 0.5$. The color bar indicates the SNR of the events.

Bottom: Cumulative histograms for the SNR ρ, 90%-credible sky area Ω_{90}, fractional luminosity distance errors $\Delta D_L/D_L$, and absolute errors on the inclination angle $\Delta\iota$ for BBH mergers observed in the six studied A+, Voyager, and NG networks for redshifts $z \leq 0.5$. The histograms were generated from $\sim 1.2 \times 10^4$ injections sampled according to Sec. IV A. The non-SNR panels are obtained for events with SNR $\rho \geq 10$, indicated by the non-shaded region in the SNR panel. The SNR panel is flipped to highlight the behavior for large values.

BBH mergers per year, all networks localize 8% to 92% of these signals to within 1 deg². Moreover, BBHs localized to within 0.1 deg² will be observed by all networks, with `HLKI+E` seeing such an event every other week, while `KI+EC` and `ECS` pushing the rates to once every other day and almost twice a day, respectively. In fact, `KI+EC` will pinpoint BBHs to within 0.01 deg² a handful of times per year and `ECS` at least once a week! Similarly, all studied networks are capable of determining the luminosity distance of 18% to all of the BBHs to 10% or less, while better than 1%-level accuracies are much rarer: none to a few golden events in `HLVKI+` or `VK+HLIv`, respectively, $O(10)$ in both `HLKI+E` and `VKI+C`, and $O(100)$ in `KI+EC` and `ECS`. Again, `KI+EC` and `ECS` will actually detect such an event about once a day. The strong difference between the BNS and BBH rates for the given measurement accuracies in `HLVKI+` are a result of the network's vastly different redshift reaches for BNS ($z_r \approx 0.11$) and BBH ($z_r \approx 0.6$).

In conclusion, all six networks will observe at least some well-localized BNS mergers per year, yet only those with at least two NG sites will provide EM astronomers with an abundance of events to follow up on a daily basis in addition to a few golden events with very high 3D-localization accuracy. While even the A+ and Voyager networks will localize a large number of well-localized BBH events, `KI+EC` and `ECS` will elevate nearly all BBHs within a redshift of $z = 0.5$ to this level and enable the follow-up of dark siren events—in the absence of an EM counterpart—on a daily basis! As such, GW170817-like follow-up campaigns could become common-place and increasingly more dependent on the EM telescopes' availability and slewing capabilities. We also want to stress that while the rates that `KI+EC` and `ECS` enable could be deemed as unnecessarily high, in reality, not every GW event can be followed-up due to maintenance outages of EM telescope, conflicts with other observations, or the potential of objects covering the EM counterpart or the source galaxy amongst other things.

B. Early warning alerts

The EM follow-up campaign of the event GW170817 was successful in spite of the fact that the earliest observations took place many hours after the epoch of merger [65], thereby missing critical data from the fireball that would have been launched moments after the merger as evidenced by the detection of gamma ray bursts by the Fermi gamma ray observatory [182, 183] and the INTEGRAL satellite [184] a mere 1.7 s after merger. The alert from LIGO and Virgo with the full 3D localization of the event was delayed by a little over 4.5 hrs [185] (see, in particular, GCN Circular Number 21513). Six groups reported optical observations carried out between 10.89 hrs and 11.57 hrs after the epoch of merger [12]. During the third observing run, GW alerts have been sent out with a average latency of about 5 to 7 minutes (see Appendix A of Ref. [64]) and there is effort to reduce the latency to less than a minute. So far, GW170817 remains the only GW event with an EM counterpart.

a. Motivation for observing events at the onset of merger From an astrophysical point of view, there are compelling reasons to begin EM observation right at the onset of merger (see, e.g., Ref. [186] for a summary) but that would require sending
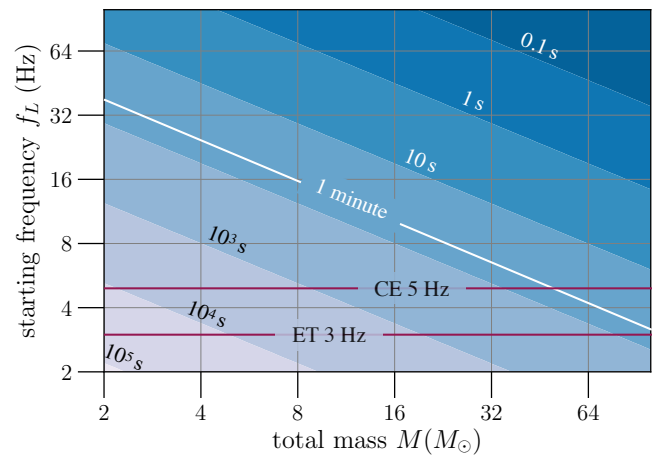

FIG. 8. The plot shows the duration (in seconds) for which a GW signal from an equal-mass binary of total mass M lasts until coalescence starting from frequency f_L.

alerts before the epoch of merger [187] to allow EM telescopes to slew to the right part of the sky. Early X-ray observations could resolve the initial state of the merger remnant, namely if a hypermassive NS forms first before collapsing to a BH or if the collapse is prompt. Immediate optical and infrared observations could inform the nature of the dynamical ejecta and outflow, formation of the accretion disc, and the onset of r-process nucleosynthesis. Radio observations could shed light on the magnetosphere interactions between the two NSs before merger and test the hypothesis that some fast radio bursts result in the aftermath of a BNS merger. As we shall argue below, it should be possible to send out alerts before the epoch of coalescence [153, 187–196] and efforts are underway to accomplish this during the fourth observing run of the LIGO and Virgo detectors [186, 197, 198].

b. Coalescence time scale Gravitational waves from the inspiral phase of BNSs last for tens of minutes to hours in ground-based detectors depending on the lower-frequency cutoff. The time left until coalescence, often referred to as *coalescence time*, starting from a frequency f_L, is given by [199]

$$\tau \simeq \left(\frac{0.25}{\eta}\right)\left(\frac{2.8\,M_\odot}{M}\right)^{5/3}\left(\frac{5\,\text{Hz}}{f_L}\right)^{8/3} 6.4 \times 10^3\ \text{s}, \quad (10)$$

where, as before, η is the symmetric mass ratio and M is the observed total mass of the system related to its intrinsic mass via $M \equiv (1 + z)M_{\text{int}}$. Thus, asymmetric binaries last longer compared to symmetric ones but the time-scale is a sharp function of both the total mass and the starting frequency.

Figure 8 plots the duration of a compact binary signal as a function of the total mass and the starting frequency for equal mass (i.e., $\eta = 1/4$) binaries. In current detectors the lower-frequency cutoff is $f_L = 20$ Hz and sources are detected at $z \ll 1$. Thus, a typical BNS would last for a few minutes. With A+ detectors, which are expected to have a lower-frequency cutoff of 10 Hz, this increases to about 15 minutes. For CE, however, a lower-frequency cutoff of 5 Hz is appropriate and BNSs at $z = 0$ would last for slightly less than two hours, while in the case ET $f_L = 3$ Hz is more appropriate, in which case $\tau \sim 6.9$ hrs.

Thus, as a detector's low-frequency sensitivity improves signals last longer and some of these could be detected well before the epoch of coalescence, making it possible to send *early warning* (EW) alerts to EM telescopes to observe the events either before or right at the onset of coalescence. Due to the sharp dependence of the time-scale on the total mass, it is far more plausible to send EW alerts for lower-mass systems than it is to do so for higher-mass binaries.

c. Early warning and localization Current algorithms are able to filter the data through a template bank within about 30 s after data acquisition. This includes time required for data transfer and application of denoising algorithms. With lower frequencies and longer duration templates filtering the data could take longer and we assume a latency of 60 s for data processing. To slew telescopes to the direction would also involve some latency and we assume that with automation this would be as low as 60 s. In what follows we will consider three EW times: $\tau_{\mathrm{EW}} = 600\,\mathrm{s}$, $\tau_{\mathrm{EW}} = 300\,\mathrm{s}$ and $\tau_{\mathrm{EW}} = 120\,\mathrm{s}$ before merger. Given the EW time, Eq. (10) can be inverted to determine the frequency f_{EW} from which the system has time τ_{EW} left until coalescence:

$$ f_{\mathrm{EW}} \simeq \left(\frac{0.25}{\eta}\right)^{3/8} \left(\frac{2.8\,M_\odot}{M}\right)^{5/8} \left(\frac{120\,\mathrm{s}}{\tau_{\mathrm{EW}}}\right)^{3/8} 22.2\,\mathrm{Hz} \qquad (11) $$

In computing the Fisher matrix integrals for EW alerts, we use a lower frequency of $f_L = 5\,\mathrm{Hz}$ for all detectors except Virgo+ for which it is set to be $f_L = 10\,Hz$ (see Sec. II C) and an upper frequency cutoff of $f_U = f_{\mathrm{EW}}$.

In order to follow-up GW events, EM telescopes would need to be given the 3D localization of the events with a fairly good accuracy. The best optical and infrared telescopes, such as the Rubin Observatory, have a FOV of $10\,\mathrm{deg}^2$, while others have narrower FOV of $\sim 1\,\mathrm{deg}^2$. X-ray and radio observatories have still narrower FOV of $\sim 0.1\,\mathrm{deg}^2$. Follow-up observations typically cover a sky area equivalent to several times their FOV and we assume the number of such follow-up grids to be between 10 to 100. We will, therefore, consider the number of events that can be localized to within $\Omega_{90} = 100\,\mathrm{deg}^2$, $20\,\mathrm{deg}^2$, $10\,\mathrm{deg}^2$, and $1\,\mathrm{deg}^2$.

Current GW observatories can localize only few events to such narrow regions in the sky *even with the full-signal power* and while their planned upgrades (A+, Voyager) will indeed see many events with a $\Omega_{90} \leq 100\,\mathrm{deg}^2$, see Fig. 6, this unfortunately does not translate to early warning: Less than $\lesssim 0.5\%$ of events can be detected 2 minutes before coalescence in the case of the Voyager network, see Fig. 9 which plots the cumulative density plots of the SNR (left panels) and Ω_{90} (right panels) for the detector networks considered in this study and BNS sources up to a redshift of 0.5.

The NG networks (HLKI+E, VKI+C, KI+EC, ECS) increase the detected fraction of events 2 minutes before coalescence to $\sim(53\%, 68\%, 86\%, 94\%)$. In fact, these networks will detect a considerable fraction of events also 5 minutes $\sim(45\%, 43\%, 73\%, 83\%)$ and 10 minutes $\sim(10\%, 7\%, 12\%, 13\%)$ before merger. This abundance of early detections translates to the ability to generate EW alerts with good localization accuracy for a small fraction of BNS events from 2 to 10 minutes before the epoch of coalescence. Tab. VIII lists the number of these BNS events that can be localized each year to within Ω_{90} of $(100, 20, 10, 1)\,\mathrm{deg}^2$. We have left out HLVKI+

and VK+HLIv networks as they do not have any significant number of detections with the required sky localization at least 2 minutes before coalescence. The VKI+C network can only meet the requirement of good sky localization for a handful events two minutes before merger.

From Tab. VIII, it is clear that ET plays a crucial role in the localization of events. The HLKI+E network is able to localize a few *golden events* per year to within $10\,\mathrm{deg}^2$ 2 and 5 minutes before merger, while the ECS (KI+EC) network will observe such events almost daily (weekly) and twice a week (every other week) 2 and 5 minutes before merger, respectively. Thus, optical and infrared telescopes such as the Rubin observatory will have plenty of opportunity to observe mergers as they happen.

These numbers decrease by up to two orders of magnitude for $\Omega_{90} \leq 1\,\mathrm{deg}^2$, yet the NG observatories KI+EC and ECS meet this constraint for a few *golden* events each year 2 and 5 minutes before the merger, thereby providing a number of events for early observation by EUCLID, Athena, Nancy Grace Roman, Chandra, Lynx, Swift-XRT, 30 m-Telescope, and Keck, and even by optical and infrared telescopes, such as the VLT, ELT, and GMT, with their smaller FOVs thanks to the potential of tiling.

VI. RARE AND LOUD EVENTS

The quality of science delivered by a GW network is determined by a combination of a large number of events at moderate SNR and a population of loud events, even if a small number, that would be useful in obtaining answers to certain key physics questions. The Advanced LIGO and Virgo network makes most of its observations at or near the threshold SNR [6, 7]. The loudest event so far is the BNS merger GW170817 [9] and it has undoubtedly delivered the best science to date, impacting many branches in physics and astronomy [12, 31, 48, 54, 55, 67, 70, 75, 76]. The number of events observed until now is also low—about one per week [7]. As shown in Sec. IV, with the HLVKI+ network the number of BNS (BBH) events will increase to 100s (1000s) per year but there will not be (m)any high fidelity BNS or BBH signals with SNR well beyond 100. This is because, the number of events at an SNR of ρ_2 (300 or 1000), relative to an SNR of ρ_1 (100), would be roughly a factor $(\rho_2/\rho_1)^3$ (respectively, 27 or 1000) smaller. The VK+HLIv network will observe a handful of BBH events with SNR > 300 but not any high-SNR BNS mergers.

NG observatories will usher in an era of precision measurements by observing large populations of signals that are needed to mitigate statistical uncertainties and systematic biases for some of the inferences (e.g. precision cosmology); with hundreds of high-SNR ($\rho \geq 300$) BBH events that could help in detecting subtle signatures of new physics, e.g. dark matter, violation of GR, etc. In this section we briefly discuss some of the most impactful science enabled by NG observatories.

a. Understanding the nature of black holes BHs are unlike other macroscopic objects. Perturbed BHs return to their quiescent state by emitting GWs whose spectra is completely determined by the BH's mass and spin angular momentum via a theorem called the *black hole no-hair theorem* [200, 201]. Thus, observation of how the remnant of a compact binary
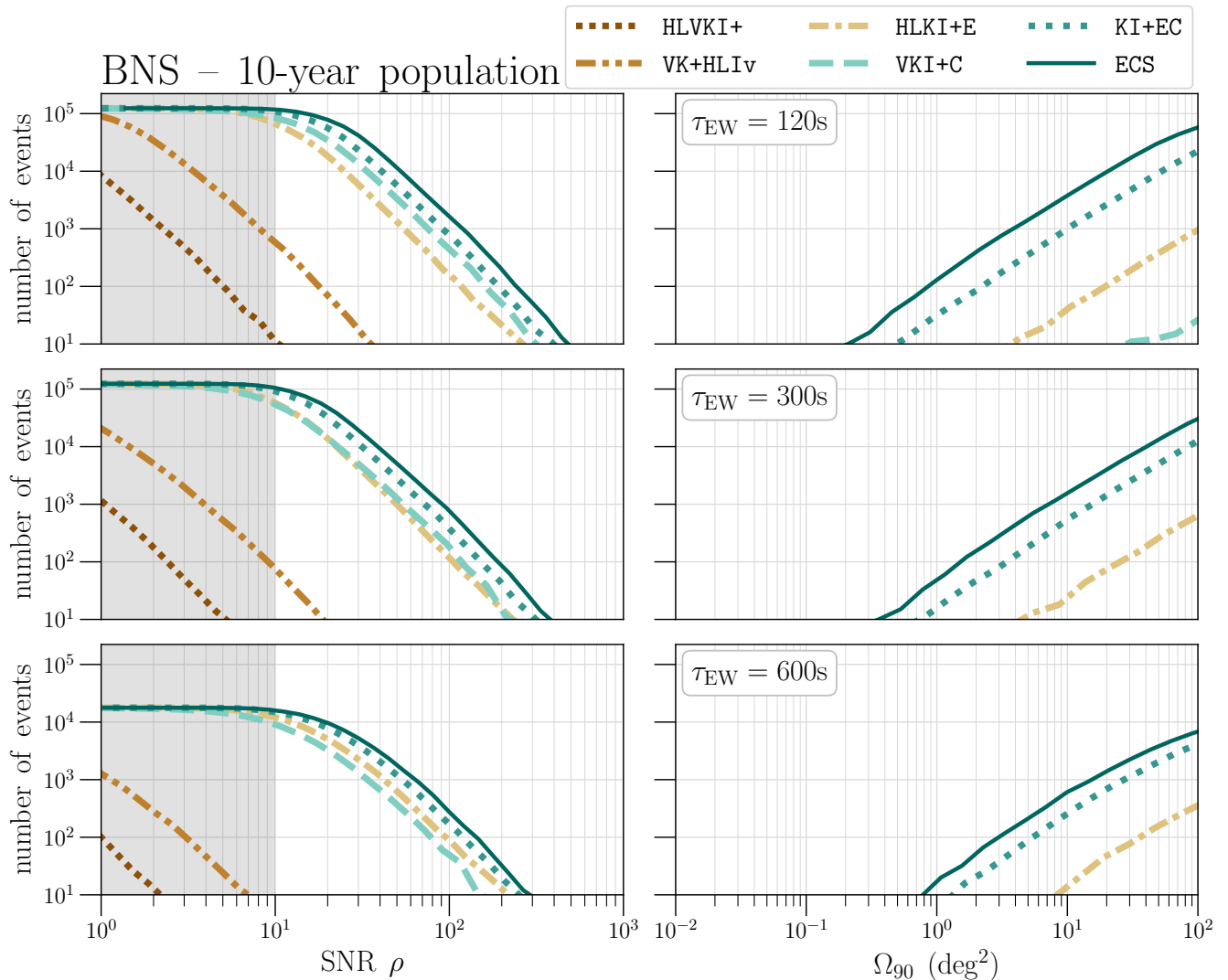
FIG. 9. Cumulative histograms for the SNR ρ and 90%-credible sky area Ω_{90} for BNS mergers observed in the six studied A+, Voyager, and NG networks for redshifts $z \leq 0.5$ 2, 5, and 10 minutes before merger. The histograms were generated from $\sim 1.2 \times 10^5$ injections sampled according to Sec. IV A. The Ω_{90} panel is obtained for events with SNR $\rho \geq 10$, indicated by the non-shaded region in the SNR panel. The SNR panel is flipped to highlight the behavior for large values.

The cumulative histograms of the SNR in the $\tau_{EW} = 600$ s panel do not reach the value 1 because $\sim 85\%$ of the events exhibited a cutoff-frequency $f_{EW} < 11$ Hz. Since this is too close to the lower frequency cutoff of the used V+ sensitivity curve used in half our networks, we chose to abort these runs for all networks.

EW time	$\tau_{EW} = 120$ s				$\tau_{EW} = 300$ s				$\tau_{EW} = 600$ s			
Ω_{90} (deg^2)	≤ 100	≤ 20	≤ 10	≤ 1	≤ 100	≤ 20	≤ 10	≤ 1	≤ 100	≤ 20	≤ 10	≤ 1
HLKI+E	50	5	2	0	28	3	1	0	3	0	0	0
VKI+C	2	0	0	0	0	0	0	0	0	0	0	0
KI+EC	1,800	210	79	3	880	99	37	1	46	8	3	0
ECS	5,100	850	330	11	2,400	320	120	4	82	16	7	0

TABLE VIII. Number of BNS mergers events for redshifts $z \leq 0.5$ observed in the six studied A+, Voyager, and NG networks that can be localized to within a small region on the sky ($\Omega_{90}/\text{deg}^2 \leq 100, 20, 10, 1$) 2, 5, and 10 minutes before merger. For a given early warning time τ_{EW} we determine the corresponding starting frequency f_{EW} using Eq. (11). The HLVKI+ and VK+HLIv networks do not meet the requirement of angular resolution for any of the early warning times considered.

coalescence settles down to its final state could tell us about its nature, but to do so, it is necessary to observe not just the fundamental mode of the GW spectrum but the higher modes and overtones excited during the coalescence [202–204]. Unfortunately, the amplitude of these sub-dominant modes and overtones is generally far lower than the dominant, fundamental quadrupole mode and detecting them would require high-SNR events [205–207]. For example, the loudest BBH event so far, GW150914, had an estimated SNR of between 4 to 8.5 in the ringdown part of the signal [29]—depending on when the ringdown signal is assumed to begin—compared to an SNR of 24 in the full inspiral-merger-ringdown signal [3]. Thus, the ringdown signal alone was not loud enough to accurately measure the parameters of even the dominant mode. To test the black hole no-hair theorem one would need to measure the complex frequencies of at least two modes with the SNR in weaker modes in excess of 15 to 20. This would require SNRs of several hundreds or more in the full signal (see, e.g., Fig. 1 of Ref. [204], cf. Tab. IV) or an SNR of 30 or more in the post-merger signal. More recently, it has been suspected that it might also be possible to detect the overtones of quasi-normal modes [208–213], which would require even higher SNRs in the post-merger signal, which, as we shall see below, is only accessible to NG observatories (cf. Fig. 10).

The *post-merger* phase of a BBH waveform is conventionally defined as the signal that follows after the waveform reaches its peak amplitude; where the amplitude evolution is given by the Euclidean norm of $h_+ - i\,h_\times$. In this study we compute this just for the quadrupole moment. Fig. 10 plots the SNR histogram in the post-merger phase of the BBH population up to redshift $z = 0.5$ observed over a duration of ten years. It is clear that only networks containing at least one NG observatory will have access to several high-fidelity events with SNR $\rho_{\text{post-merger}} \geq 100$ each year, while earlier generations of detectors will rarely see such events. Thus, NG observatories will be unique in their ability to map out the detailed structure of dynamical horizons via the complex quasi-normal mode spectrum expected in black hole mergers.

In addition to testing the no-hair theorem with perturbed BHs, it is possible to test GR by checking the consistency of the binary parameters estimated using different multipoles provided there is enough SNR from higher order modes [214, 215]. For example, the octupole mode of the inspiral signal from GW190814 is estimated to have an SNR of about 6.6 compared to the total SNR of 21.4 in the full signal [18]. In contrast, the ECS network would have, for the same event, an SNR of about 1500 in the full signal and 400 in higher order modes. Such events will determine the nature of the merger remnant with exquisite precision.

b. Inferring dense matter equation of state and QCD phase transition   Understanding the equation of state of dense nuclear matter is one of the open problems in fundamental physics (see, e.g. Ref. [216]). GW observations can determine an effective tidal deformability of a BNS system but not the tidal deformabilities of each of the companions [217, 218]. Inferring the radius of each companion would require additional assumptions that may not be valid [219, 220]. BNS mergers with SNRs in excess of several hundreds, which will be rare but abundant in the NG era, will enable accurate inference of the tidal deformabilities of both NSs without requiring additional
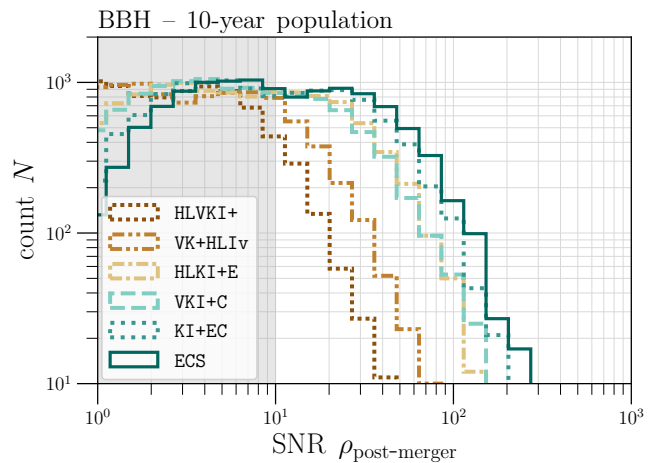

FIG. 10. Histograms of the SNR $\rho_{\text{post-merger}}$ in the post-merger signal of the BBH population in the six studied A+, Voyager, and NG networks for redshifts $z \leq 0.5$ and a observation time of **10 years**. The histograms were generated from $\sim 1.2 \times 10^4$ injections sampled according to Sec. IV A.

assumptions [221]. Thus, we expect NG observatories to measure radii of NSs to within a few hundred meters and infer the equation of state of cold dense nuclear matter to a high degree of precision [121]. The post-merger oscillations could also carry the signature of the *hot* dense matter equation of state that could be determined by NG observatories by accurately measuring the complex oscillation frequencies [222–225].

The remnant that forms after the coalescence of a BNS could sometimes be a hypermassive NS with core densities possibly exceeding several times the nuclear density [226, 227]. At such densities, matter could undergo quark-deconfinement phase transitions [228], from the hadronic phase to quark-gluon plasma, and this signature might be present in the post-merger GWs emitted by the hypermassive remnant [229, 230]. NG networks would observe post-merger signals with SNRs of 20 or more [231] depending on the equation-of-state and thereby shed light on the QCD (quantum chromodynamics) phase transition.

c. Testing general relativity   General relativity is consistent with laboratory experiments and astronomical observations over a wide range of field strengths [232]. Yet, the theory raises a number of fundamental questions that have not found satisfactory answers [233, 234]. These include BH information loss [235] and non-unitary evolution of quantum states [236], the late-time accelerated expansion of the Universe and the nature of the cosmological constant or dark energy [237, 238], BH and big bang singularities that pose a major conceptual hurdle in predictability [239], to name a few. By directly probing BH horizons and the way remnant objects approach their final state it will be possible to probe predictions of GR to higher precision [203]. NG observatories with hundreds of high-SNR BBH events with SNR > 300 will not only detect many subtle effects predicted in GR but allow precision tests of the theory [240]. For example, by measuring the final state of the BH and comparing it to the properties of the progenitor binary when the companion stars are widely separated it will be possible to test strong-field predictions in the full non-linear GR [241, 242].

Additionally, it will be possible to test predictions of alternative gravity theories invoked to explain the Universe's recent (i.e. $z \lesssim 1$) accelerated expansion, the presence of dipole radiation, and constraints on the Brans-Dicke parameter [243, 244]. With signals that arrive from very large redshifts ($z \gtrsim 10$) it will be possible to set tighter bounds on the graviton mass [245] and Lorentz violations [246].

d. Probing population III stars and primordial black holes Next generation observatories will have access to events at redshifts larger than 15—an epoch when the first stars were formed from primordial hydrogen and helium and devoid of heavier elements [247]. Detecting merging BBHs from that epoch could shed light on the properties of population III stars, especially their mass spectrum and redshift distribution. NG observatories will have the unique capability to not only detect a majority of the binaries from this epoch (with up to 70% efficiency at a redshift of $z = 20$) but decisively measure distances and infer their redshift [248, 249]. Indeed, black holes formed in the early Universe (primordial black holes) have been proposed to be sources of gravitational waves observed by LIGO and Virgo (see, e.g., Ref. [88, 90, 250, 251] for a discussion of the origin of primordial black holes), and NG detectors would have the best sensitivity high-redshift BBH coalescences in the mass range 10-100 $M_\odot$, at redshifts $z = 20$-50, when no population III stars could have existed [120, 167]. The first BHs from this era could well be the ones that seeded the supermassive BHs found in the nuclei of most galaxies today (see, e.g., Ref. [252] for a discussion of the origin of supermassive black holes). NG detectors could help understand the formation and growth of seed BHs through early cosmic history if their masses lie below about 100 $M_\odot$ [253–257].

VII. CONCLUSION

A. Summary of results

a. Visibility of full cosmic populations Due to the vastly different reaches, see Fig. 2 and Tab. III, the visibility of BNS mergers differs greatly between the three generations of observatories, see Tab. IV. These range from detections of $\rho \geq 10$-events every other day with A+ over $\rho \geq 30$-events once a week with Voyager to at least one BNS signal with SNR $\rho \geq 100$ every other day in NG networks containing a CE detector. The lower sensitivity of ET results in less frequent detections, once every week, of such loud BNS events in HLKI+E.

Since all networks have farther reaches for BBHs signals, the BBH detection rates outpace the BNS by at least one order of magnitude in the networks without a CE detector—yielding two $\rho \geq 30$-events every three days with A+, weekly $\rho \geq 100$-events with Voyager, and almost six $\rho \geq 100$-events per day with a single ET—while the rates of networks containing a CE detector are bound by the cosmic merger rate, *CE networks will observe nearly all BBHs up to redshift $z = 10$*. These networks, containing either one CE, one CE and ET, or two CEs and one ET, will observe about approximately 20 to 50 BBH signals with $\rho \geq 100$ per day. As such the differences in other metrics are discriminating factors for BBH detections.

b. Measurement quality - three-dimensional localization While the sky localization and distance estimation metrics generally follow the tendencies of the networks' visibility metric, see Tab. V, there are two stark exceptions. The NG networks containing either only one CE or only one ET exchange their roles: while ET has a lower sensitivity for BNS and BBH mergers than of CE, its low-frequency sensitivity and geometry are very advantageous for sky localization and also distance estimation.

Hence we can expect the following sky localization rates for BNS mergers from the examined networks: The A+ detector network will only observe consistently events to within $\Omega_{90} \leq 1 \deg^2$ a few times per year, while VKI+C, VK+HLIv, and HLKI+E should achieve this for 10–30 BNS signals per year. Consistent detection of BNSs localized to within $\Omega_{90} \leq 0.1 \deg^2$ requires at least two NG detector sites and even then KI+EC will only observe a handful of such events per year, while ECS will push this number to more than twice a week, and only ECS will achieve sky localizations of BNS signals to better than $\Omega_{90} \leq 0.01 \deg^2$, but only for rare, *golden* events.

While coalescences of BNSs are expected to be more abundant compared to BBHs, the intrinsic loudness of BBH mergers increases the detection rates of well-localized events: A+ and single CE networks will localize a few events per year to within $\Omega_{90} \leq 0.1 \deg^2$, while we should observe such signals once every four weeks in Voyager networks and once every other week in HLKI+E. Finally, BBHs localized to within $\Omega_{90} \leq 0.01 \deg^2$ are consistently detected only in networks containing two or three NG detectors, with KI+EC and ECS observing such events a few times per year to more than once a week, respectively! Thus, while the visibility did not allow for conclusive discrimination of the networks containing a CE detector, the sky resolution clearly favors those with at least two, preferably three NG detectors.

Finally, luminosity distance estimation accuracies better than 10% show a wide range for BNS mergers: once every five week with A+, once a week with Voyager or one CE, and 5, 18, and 41 times per day in HLKI+E, KI+EC, and ECS, respectively. BBH signals will push these numbers to more than once a day with A+, 9 times a day with Voyager, and at least 27 times per day in NG networks. In fact such networks will detect BBHs to sub-1% accuracies in the luminosity distance once a week with one CE and up to three times a day with three NG detectors.

c. Enabling multi-messenger astronomy The synergy of GW and EM observations was beautifully demonstrated with the event GW170817. As such each network's potential to enable a follow-up in the EM spectrum—even without the detection of a loud EM transient such as a GRB—is paramount in determining the network's science capabilities. The main metric is thus the sky localization in relation to the FOVs of various EM telescopes, see Tab. VI. We performed this study for BNS and BBH signals emitted from redshifts up to $z = 0.5$.

Due to the relative quietness of BNS signals, the loudest, best-localized events of the cosmic BNS population already stem from the population at $z \leq 0.5$ and the conclusions, drawn for the cosmic BNS population above, also apply to the low-z population. Hence, the A+, Voyager, and single NG detector network predominantly cater to the Rubin Observatory for follow-up surveys with a few to tens sub-1 $\deg^2$ detections per year. In fact, these networks should further be able to localize rare, *golden* BNS signals to within 0.1 $\deg^2$ once per year, thus enabling EM surveys with EUCLID, Athena, Nancy

Grace Roman, Chandra, Lynx, Swift-XRT, Keck and the 30 m-Telescope with such high-fidelity events. Networks with two or three NG detectors will deliver few to one hundred of such events to the aforementioned observatories. The triple-NG network should be able to localize rare, *golden* BNS signals to within $0.01\,\mathrm{deg}^2$, thus enabling EM follow-up with VLT and ELT. In fact, the triple-NG network is the only network to observe *golden* BNS mergers that are well-localized both on the sky ($\Omega_{90} \leq 0.01\,\mathrm{deg}^2$) and in distance ($\Delta D_L/D_L < 0.01$), see Fig. 6.

BBH detections lack EM counterparts and therefore depend on the sky localization from the GW signal to identify the binary's host galaxy. Fortunately, the intrinsic loudness of massive systems and the signal contributions from higher modes for mass-asymmetric binaries improve the sky localization estimates across all six networks, allowing them to localize BBH signals to within $0.1\,\mathrm{deg}^2$ a few times per year (A+ and one CE) and every fourth (Voyager) or second (one ET) week. Thus, starting with the Voyager generation, frequent EM follow-up surveys are possible with the following telescopes: Rubin Observatory, EUCLID, Athena, Nancy Grace Roman, Chandra, Lynx, Swift-XRT, Keck and the 30 m-Telescope. In fact the double- and triple-NG networks will observe such well-localized events every other to more than once a day. They will further provide VLT and ELT with $\Omega_{90} \leq 0.01\,\mathrm{deg}^2$-events a few times per year to more than once a week. The triple-NG network will consistently measure the three-dimensional localization of a few *golden* BBH events to better than $\Omega_{90} \leq 0.001\,\mathrm{deg}^2$ and $\Delta D_L/D_L < 0.01$, see Fig. 7, allowing for follow-up surveys by GMT and HST–WFC3 and enabling single-event, high-precision cosmology with dark sirens [132].

One particularly intriguing aspect of multi-messenger astronomy with GWs and EM radiation is the potential to trigger EW alerts for BNS coalescences ahead of the actual merger, thus enabling the EM observatories to record the events as early as possible and observe the merger in the EM spectrum as it happens. The important metric here, besides visibility, is the sky localization of the events several minutes before the merger to provide enough time for GW signal pipelines to issue an alert and telescopes to slew to the estimated sky location. In our study we found that A+ and Voyager detectors will not provide significant detection rates with the required sky localization at least 2 minutes before the merger. Similarly, a single CE network might only observe a couple such events per year early enough for the Rubin Observatory to follow-up, assuming 10-fold tiling. In contrast, the ET network should send weekly two- and biweekly five-minutes alerts. The double- and triple-NG networks on the other hand will push these numbers to 5–13 daily two-minutes, 2–6 daily five-minutes, and *approximately weekly ten-minutes* alerts to the Rubin Observatory. In fact, both networks would even provide EUCLID, Athena, Nancy Grace Roman, Chandra, Lynx, Swift-XRT, Keck and the 30 m-Telescope with two-minutes and 5-minutes EW alerts for a handful of golden events per year, see Tab. VIII.

B. Limitations of the study

The main caveat of this study is the use of the Fisher information formalism to provide measurement quality estimates. The formalism is well-known and tested, see [258] for a review of its shortcomings and [259, 260] for two approaches to improve the reliability of the Fisher-based error estimates based on Derivative Approximation for Likelihoods and the incorporation of priors for the estimates, respectively. Yet, the formalism only provides estimates for Gaussian posteriors which is likely not the best assumption for the noise of these detectors; especially for signals at visibility threshold. Further, the reliance on numerical derivatives for LAL waveforms and the numerical inversion of the Fisher matrix are sources for numerical uncertainties affecting the quoted results. Further, we did not examine the quality of spin measurements since the addition of such parameters in the Fisher analysis lead to a high rate of ill-conditioned Fisher matrices for which the numerical inversion is not to be trusted.

Lastly, the chosen population distributions—chosen to be consistent with the LIGO and Virgo observations both in mass and redshift distributions—do not capture unexpected sources such as large merger populations of population III star remnants or primordial BHs at large redshifts beyond $z = 10$. Besides, the chosen populations only include injections for which the component spins and the binary's orbital angular momentum are aligned and the chosen waveforms are non-precessing; thus the effects of spin-precession are not accounted for in the forecasts made in this study.

C. Outlook and further studies

Ultimately we can conclude that while the A+ and Voyager upgrades would do a tremendous job to increase the current detector facilities' lifespan and science capabilities. Yet, only two- and three-site NG networks will expand the detection reach significantly to observe binary black hole mergers from the edge of the observable Universe—a regime inaccessible to electromagnetic observations. These networks would be capable to observe almost every binary coalescences up to redshift $z = 0.9$ and thus provide abundant detection rates enabling scientists to examine binary progenitor population and formation channels, map the large-scale structure of the universe, perform high-precision cosmology and tests of GR, etc. Further, the three-dimensional localization capabilities of such networks should enable a host of electromagnetic telescopes to not only follow-up the detections searching for counterparts and host galaxies, but actually even alert these observatories minutes before the actual mergers in the case of BNSs, allowing astronomers to record the mergers in the electromagnetic spectrum as it happens. Finally, the large rates would further provide redundancies for follow-up surveys to ensure that enough gravitational-wave events can be examined in the electromagnetic window when accounting for maintenance and already reserved observation time. Hence, the planned and proposed detector updates and new facilities will be an important addition for the fundamental physics, astrophysics and cosmology communities.

ACKNOWLEDGMENTS

Appendix A: GWBENCH settings

We used the waveform wrapper `wf_model_name = 'lal_bns'` with the waveform model `wf_other_var_dic = {'approximant':'IMRPhenomD_NRTidalv2'}` for BNS injections and the wrapper `wf_model_name = 'lal_bbh'` together with `wf_other_var_dic = {'approximant':'IMRPhenomXHM'}` for BBH injections. The numerical derivatives were computed using step sizes of `step = 1e-9` and `step = 1e-6` for `IMRPhenomD_NRTidalv2` and `IMRPhenomXHM`, respectively. The derivative method was set to `method = 'central'` or `method = 'backward'` in case the chirpmass was close to 0.25 while the method and derivative orders were set to `order = 2` and `d_order_n = 1`, respectively. Further we set `use_rot = 1`, `conv_cos = None`, `conv_log = ('Mc','DL','lam_t')`. The injection sets were generated using the `injections` module of `gwbench`: `injections.injections_CBC_params_redshift` with `redshifted = 1`. For BNSs we used the following seeds for the various redshift bins (zmin, zmax, seed): (0, 0.5, 7669), (0.5, 1, 3103), (1, 2, 4431), (2, 4, 5526), (4, 10, 7035), and (10, 50, 2785). For BBHs we used (0, 0.5, 5485), (0.5, 1, 1054), (1, 2, 46), (2, 4, 5553), (4, 10, 5998), and (10, 50, 4743).

Appendix B: Data release

We will share the raw data for a number of networks—including the ones presented in this paper—together with the data used in a different, ongoing study once we publish the results of that study.

Appendix C: Sigmoid best-fit parameters

Tabs. IX and X record the best-fit parameters a, b, and c of the sigmoid curves fitted to the detector efficiencies $\epsilon(z)$ in Fig. 2 Sec. III and Fig. 14 in App. E, respectively.

Appendix D: Visibility and measurement quality: histograms

In Sec. IV we presented the cumulative density plots of the SNR, 90%-credible sky area, and other parameters. Here we show the corresponding histograms for the respective parameters, presented on a log-log scale in Figs. 11 and 12. Since the total number of events accessible each year is in excess of a million for BNS and more than one-hundred thousand for BBH, we have shown the histograms over five orders of magnitude in density. This will help recognize events at the tail end of the distribution that cannot be easily inferred from the cumulative distribution. In order to minimize Monte Carlo errors we have used a number of events expected over a 10-year period. However, as discussed in Sec. IV, numbers quoted in the text and various tables assume a 1-year observation period.

While events at the tail end of the distribution are rate, they would be very loud and their parameters will be measured with great precision. For example, only NG observatories have the potential to observe significant number of BNS (BBH) mergers with SNRs larger than 100 (1000) and localize sources to better than 10 arc min^2. We examine the science potential of these tail ends events in Sec. VI.

The density plots readily reveal the mode of the distributions, indicating where to expect most of the events to lie, and limitations of different networks, informing the best science return we can hope to extract. In fact, we see that the three generations (A+, Voyager, and NG) are qualitatively different with respect to every metric used in this study.

Appendix E: Cosmic Explorer: Influence of Proposed Detector Configurations

In developing the science case for a NG GW detector proposal, the Cosmic Explorer Project is investigating various configurations of CE detectors, e.g. with varying detector arm lengths and hence detectors sensitivity curves, see Fig. 13. Given the early state of the CE detector proposal, we included, for completeness, four networks containing one or two CE detectors with either 20 km or 40 km arms to demonstrate the potential of NG networks without an ET detector: `VKI+C..20`, `VKI+C..40`, `VKI+C..20-40`, and `VKI+C..40-40`. The `VKI+C..40` network is the same as `VKI+C` and is included as a reference from the main body of this paper. Figs. 14 to 23 reiterate the plots presented throughout this paper for these four CE networks instead of the six studied A+, Voyager, and NG networks.

Comparing Tabs. XI and XII to III and IV indicates a single 20 km CE detector to be equivalent *in sensitivity* to one ET when either is embedded into a network of A+ detectors. Hence, the `VKI+C..20` and `HLKI+E` (`VKI+C..20-40` and `KI+EC`) networks yield comparable reaches, per-mille redshifts, and detection rates at the respective threshold SNR values.

TABLE IX. The best-fit parameters a, b, and c of the sigmoid function, $f(z) = [(1 + b)/(1 + b\,e^{az})]^c$, fitted to the detection efficiency $\epsilon(z, \rho_*)$ curves of detector networks in Fig. 2 for two values of the SNR threshold $\rho_* = 10$ and $\rho_* = 100$.

Sigmoid parameter	$\rho_* = 10$			$\rho_* = 100$		
	a	b	c	a	b	c
	BNS					
HLVKI+	64.62	0.005701	0.3495	743.5	0.003345	0.3067
VK+HLIv	28.98	0.01056	0.3125	299.6	0.008898	0.3247
HLKI+E	14.95	0.006631	0.1549	129.1	0.0088	0.2344
VKI+C	5.471	0.1155	0.2049	40.74	0.07955	0.5162
KI+EC	6.708	0.01416	0.1403	52.8	0.01481	0.3585
ECS	5.834	0.00928	0.09996	44.96	0.01035	0.3129
	BBH					
HLVKI+	25.11	0.002056	0.08482	210.9	0.004143	0.1138
VK+HLIv	14.74	0.001824	0.04888	95.27	0.006636	0.1123
HLKI+E	14.2	5.08e-05	0.007811	43.1	0.004653	0.07757
VKI+C	14.2	0.03823	0.003638	16.46	0.08902	0.1202
KI+EC	2.792	0.006192	0.01262	19.55	0.00885	0.08601
ECS	0.1211	0.4108	0.2391	17.22	0.004554	0.06978

TABLE X. The best-fit parameters a, b, and c of the sigmoid function, $f(z) = [(1 + b)/(1 + b\,e^{az})]^c$, fitted to the detection efficiency $\epsilon(z, \rho_*)$ curves of detector networks in Fig. 14 for two values of the SNR threshold $\rho_* = 10$ and $\rho_* = 100$.

Sigmoid parameter	$\rho_* = 10$			$\rho_* = 100$		
	a	b	c	a	b	c
	BNS					
VKI+C..20	8.162	0.08435	0.2873	70.18	0.07338	0.4655
VKI+C..40	5.471	0.1155	0.2049	40.74	0.07955	0.5162
VKI+C..20-40	6.161	0.02666	0.153	48.81	0.02272	0.3887
VKI+C..40-40	5.384	0.02244	0.127	43.41	0.01781	0.3592
	BBH					
VKI+C..20	17.42	0.005799	0.007106	24.83	0.07936	0.1399
VKI+C..40	14.2	0.03823	0.003638	16.46	0.08902	0.1202
VKI+C..20-40	2.077	0.04043	0.01891	18.02	0.01749	0.09498
VKI+C..40-40	0.06361	0.4927	0.719	15.64	0.0136	0.08679

As the comparison of the VKI+C and HLKI+E networks already predicted, *measurement quality* depicts a more nuanced picture which does not strictly follow the conclusions drawn based on sensitivity. Comparing Tabs. XIII and XIV to V and VII, it is clear that the ET network outpaces both single CE networks, VKI+C..20 and VKI+C..40, in detection rates of well-localized events in sky area and luminosity distance for BNSs and BBHs. In fact, the single ET network slightly outperforms both double-CE networks, VKI+C..20-40 and VKI+C..40-40, in sky localization for BNSs and matches the BBHs numbers of VKI+C..20-40. The two 40 km CEs in VKI+C..40-40 will detect more well-localized BBHs per year than HLKI+E, yet fall significantly behind the KI+EC network with one ET and one 40 km CE. The situation flips again in favor of the double-CE networks for luminosity distance estimation: both VKI+C..20-40 and VKI+C..40-40 measure the luminosity distance to BNSs and BBHs consistently at a level between KI+EC and ECS.

Since early warning detections heavily depend on a network's capability to detect GWs at an early stage in the binary evolution, the double-CE networks should observe EW BNS events more often than HLKI+Edue to the higher sensitivity of CE, but much less frequently than either KI+EC or ECSwhich combine the strengths of the ET and CE detectors (see Table XV in comparison to Table VIII).
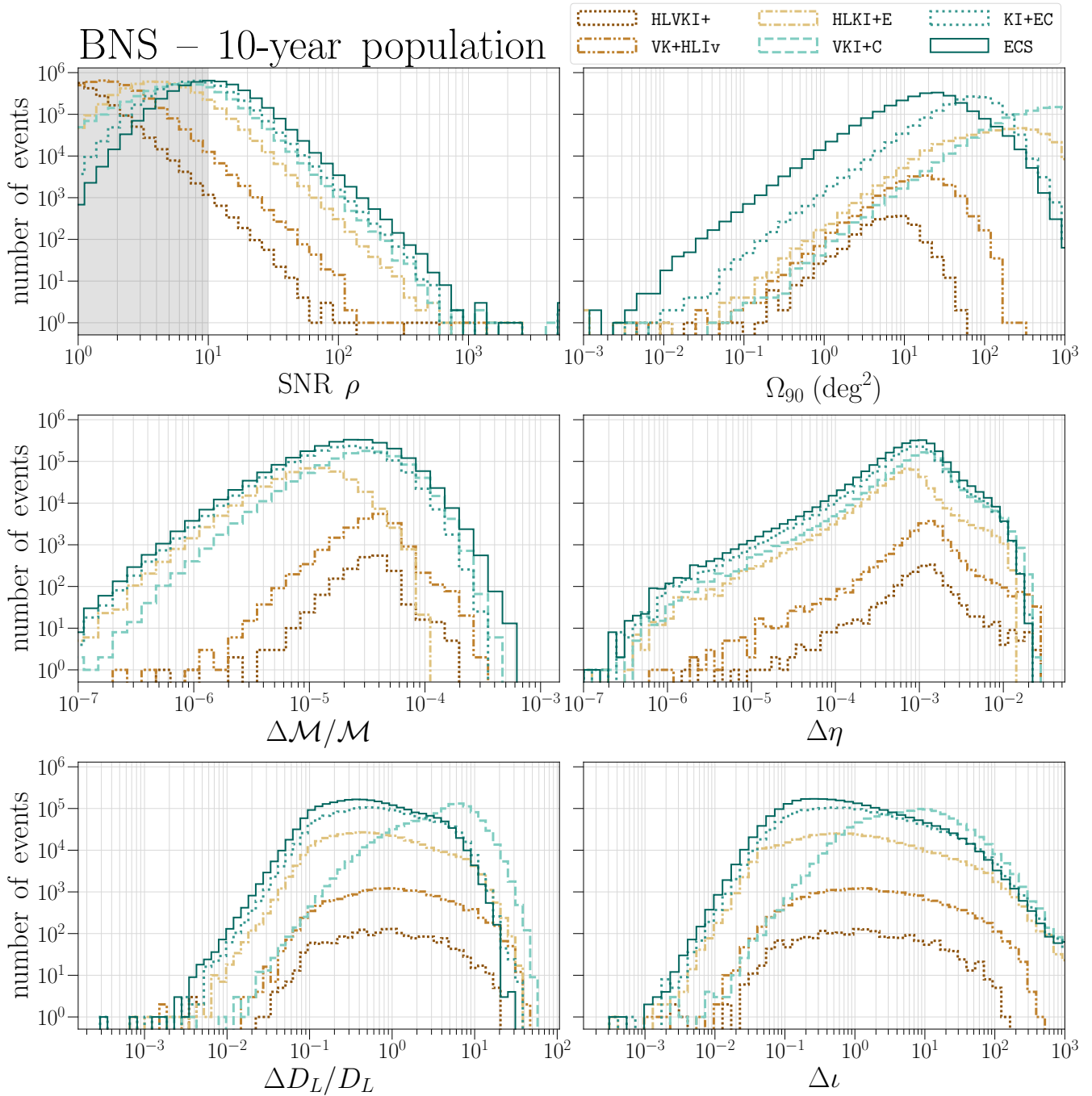
FIG. 11. Histograms of the **10 years** BNS injection sample used to generate Fig. 3 for SNR ρ, 90%-credible sky area Ω_{90}, fractional errors on chripmass $\Delta\mathcal{M}/\mathcal{M}$ and luminosity distance $\Delta D_L/D_L$, and absolute errors on symmetric mass ratio $\Delta\eta$ and the inclination angle $\Delta\iota$ observed in the six studied A+, Voyager, and NG networks. The histograms were generated from $\sim 4.7 \times 10^6$ injections sampled according to Sec. IV A. The non-SNR panels are obtained for events with SNR $\rho \geq 10$, indicated by the non-shaded region in the SNR panel.
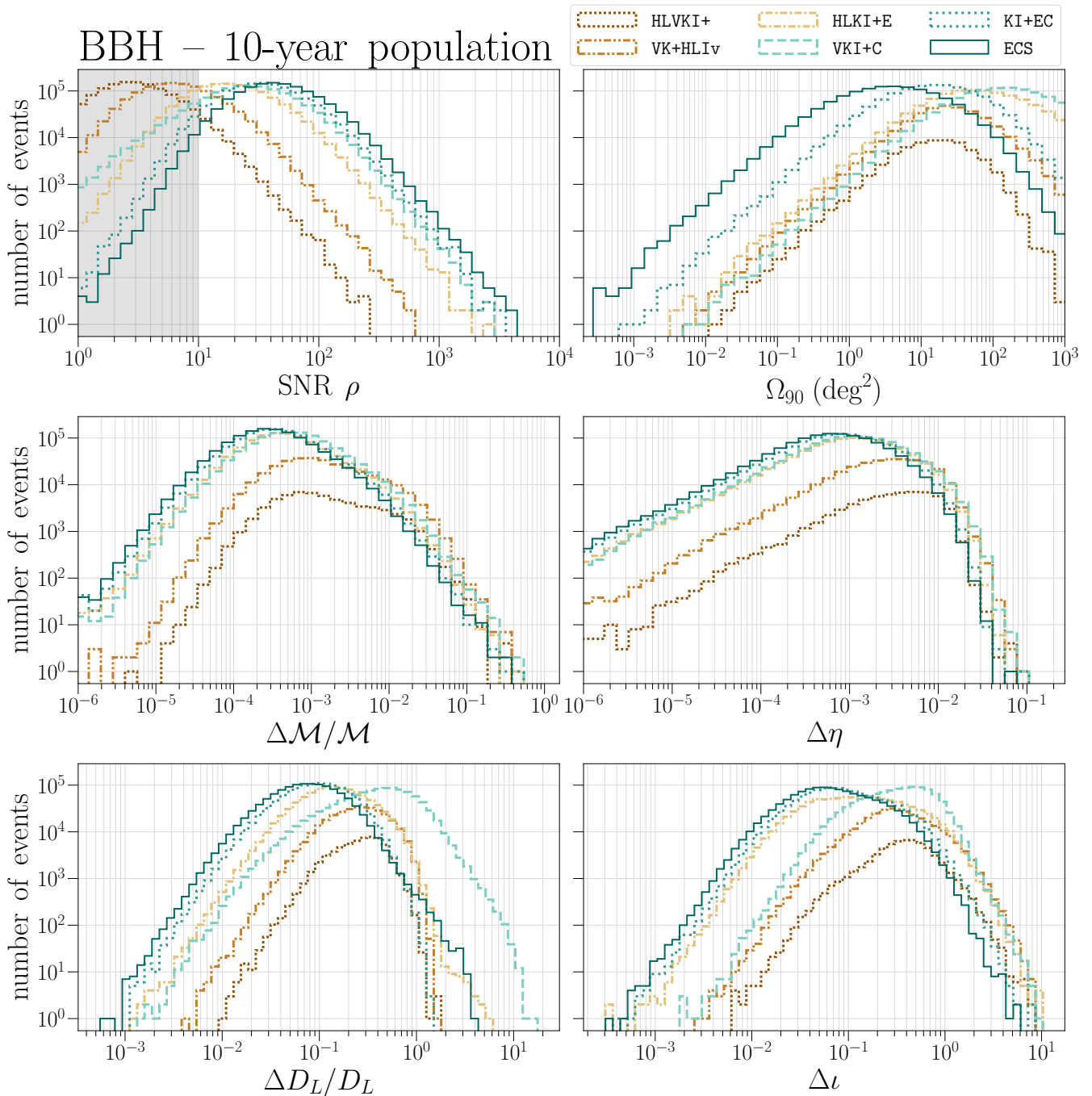
FIG. 12. Histograms of the **10 years** BBH injection sample used to generate Fig. 4 for SNR ρ, 90%-credible sky area Ω_{90}, fractional errors on chripmass $\Delta\mathcal{M}/\mathcal{M}$ and luminosity distance $\Delta D_L/D_L$, and absolute errors on symmetric mass ratio $\Delta\eta$ and the inclination angle $\Delta\iota$ observed in the six studied A+, Voyager, and NG networks. The histograms were generated from $\sim 1.2 \times 10^6$ injections sampled according to Sec. IV A. The non-SNR panels are obtained for events with SNR $\rho \geq 10$, indicated by the non-shaded region in the SNR panel.
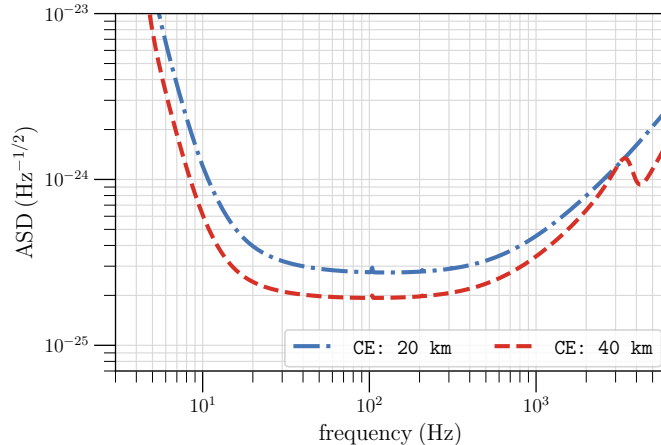
FIG. 13. Sensitivity of the two examined Cosmic Explorer configurations with 20 km and 40 km arm length, respectively. The noise curves are taken from the `ce2_20km_cb` and `ce2_40km_cb .txt`-files inside `ce_curves.zip` file at https://dcc.cosmicexplorer.org/CE-T2000007.
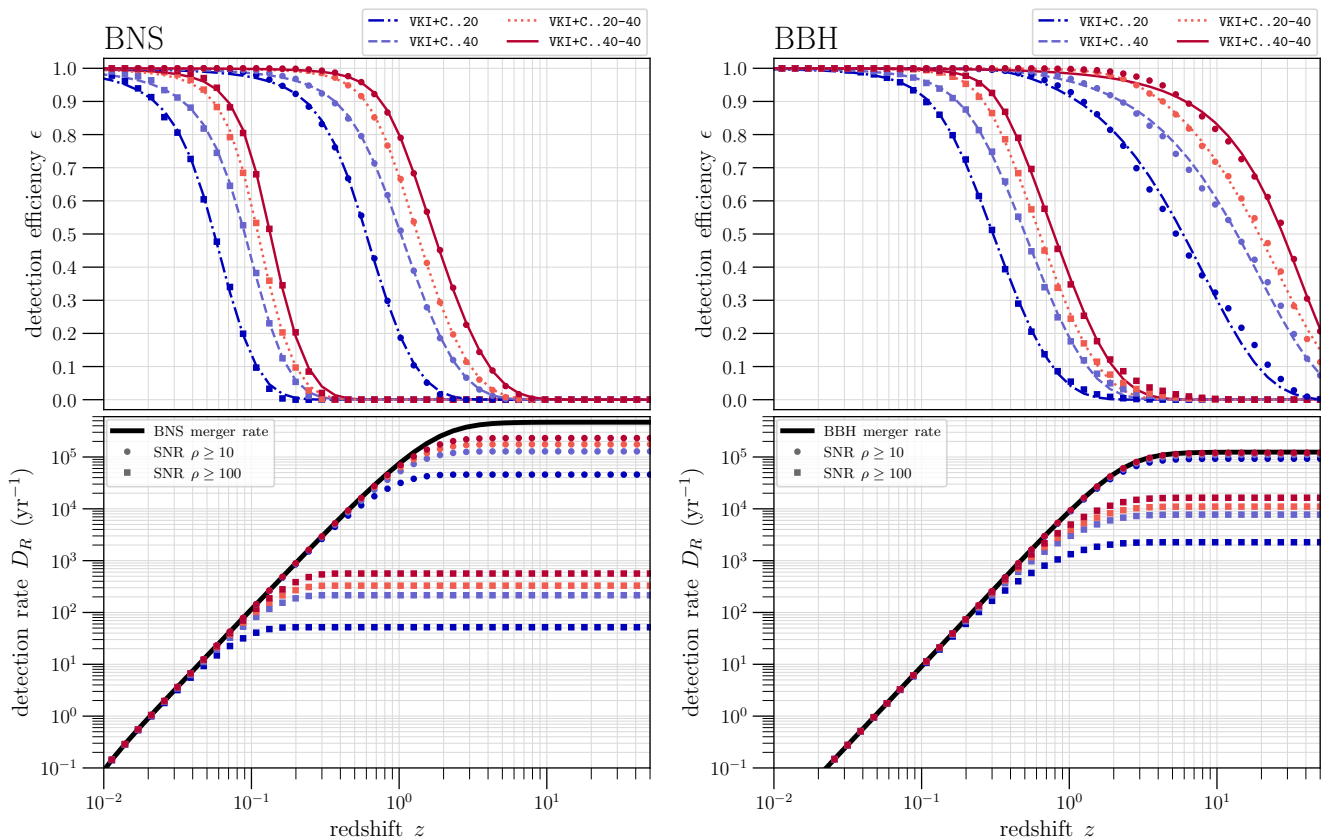

FIG. 14. Detection efficiencies ϵ and detection rates D_R, see Eqs. (3) and (9), respectively, of the four studied CE networks are plotted as functions of redshift z. The efficiency specifies the value at the indicated redshift z while the detection rate corresponds to the integrated rate up to that redshift. The circles (squares) denote the values for events with SNR $\rho \geq 10$ ($\rho \geq 100$). The thick, black lines in the rate panels are the cosmic BNS and BBH merger rates, see Sec. III. The fit lines in the efficiency panels are sigmoid fits with $f_{\text{sigmoid}} = \left(\frac{1+b}{1+b\,e^{ax}}\right)^c$.

TABLE XI. The reach z_r and per-mille redshift z_{pm} of the considered networks for BNS and BBH signals with SNRs $\rho \geq 10$ or $\rho \geq 100$. Here we define the reach (per-mille redshift) as the redshift at which a given network detects 50% (0.1%) of the injections with the specified SNR or louder. Please refer to the detection efficiency panels of Fig. 14 for a visual representation.

	BNS				BBH			
SNR ρ	≥ 10		≥ 100		≥ 10		≥ 100	
	z_r	z_{pm}	z_r	z_{pm}	z_r	z_{pm}	z_r	z_{pm}
VKI+C..20	0.6	3.3	0.06	0.25	5.9	41	0.3	2.1
VKI+C..40	1	6.6	0.09	0.39	14	> 50	0.5	3.6
VKI+C..20-40	1.3	7.9	0.11	0.44	19	> 50	0.63	4.3
VKI+C..40-40	1.7	11	0.13	0.54	28	> 50	0.79	5.4

TABLE XII. Cosmic merger rates (per year) of BNS and BBH mergers in the Universe and the number that would be observed by different detector networks each year with $\rho \geq 10, 30, 100$, where ρ is the signal-to-noise ratio. Due to uncertainty in the various quantities that go into the calculation these numbers are no more accurate than one or two significant figures.

	BNS			BBH		
Cosmic rate	4.7×10^5			1.2×10^5		
SNR ρ	≥ 10	≥ 30	≥ 100	≥ 10	≥ 30	≥ 100
VKI+C..20	37,000	1,400	38	89,000	27,000	1,700
VKI+C..40	110,000	6,000	160	110,000	53,000	6,400
VKI+C..20-40	150,000	9,200	250	120,000	66,000	9,200
VKI+C..40-40	210,000	16,000	420	120,000	80,000	14,000

TABLE XIII. Detection rates of BNS and BBH mergers from the full redshift range $z \in [0.02, 50]$ to be observed by different detector networks each year with $\Omega_{90}/\text{deg}^2 \leq 1, 0.1, 0.01$ as well as $\Delta D_L/D_L \leq 0.1, 0.1$, where Ω_{90} is the 90%-credible sky area and D_L the luminosity distance. These detection rates are calculated for events with SNR $\rho \geq 10$. Due to uncertainty in the various quantities that go into the calculation these numbers are no more accurate than one or two significant figures.

Metric	Ω_{90} (deg^2)			$\Delta D_L/D_L$	
Quality	≤ 1	≤ 0.1	≤ 0.01	≤ 0.1	≤ 0.01
BNS					
VKI+C..20	10	1	0	46	0
VKI+C..40	11	1	0	67	0
VKI+C..20-40	240	7	1	2,100	4
VKI+C..40-40	360	10	1	4,000	6
BBH					
VKI+C..20	190	7	0	6,200	18
VKI+C..40	210	8	0	10,000	45
VKI+C..20-40	4,400	180	6	34,000	240
VKI+C..40-40	6,300	270	9	42,000	420

TABLE XIV. Detection rates of BNS and BBH mergers up to redshift $z = 0.5$ to be observed by different detector networks each year with $\Omega_{90}/\text{deg}^2 \leq 1, 0.1, 0.01$ as well as $\Delta D_L/D_L \leq 0.1, 0.1$, where Ω_{90} is the 90%-credible sky area and D_L the luminosity distance. These detection rates are calculated for events with SNR $\rho \geq 10$. Due to uncertainty in the various quantities that go into the calculation these numbers are no more accurate than one or two significant figures. The bare merger rates for BNSs and BBHs up to redshift $z = 0.5$ are $\sim 12,000\,\text{yr}^{-1}$ and $\sim 1,200\,\text{yr}^{-1}$, respectively.

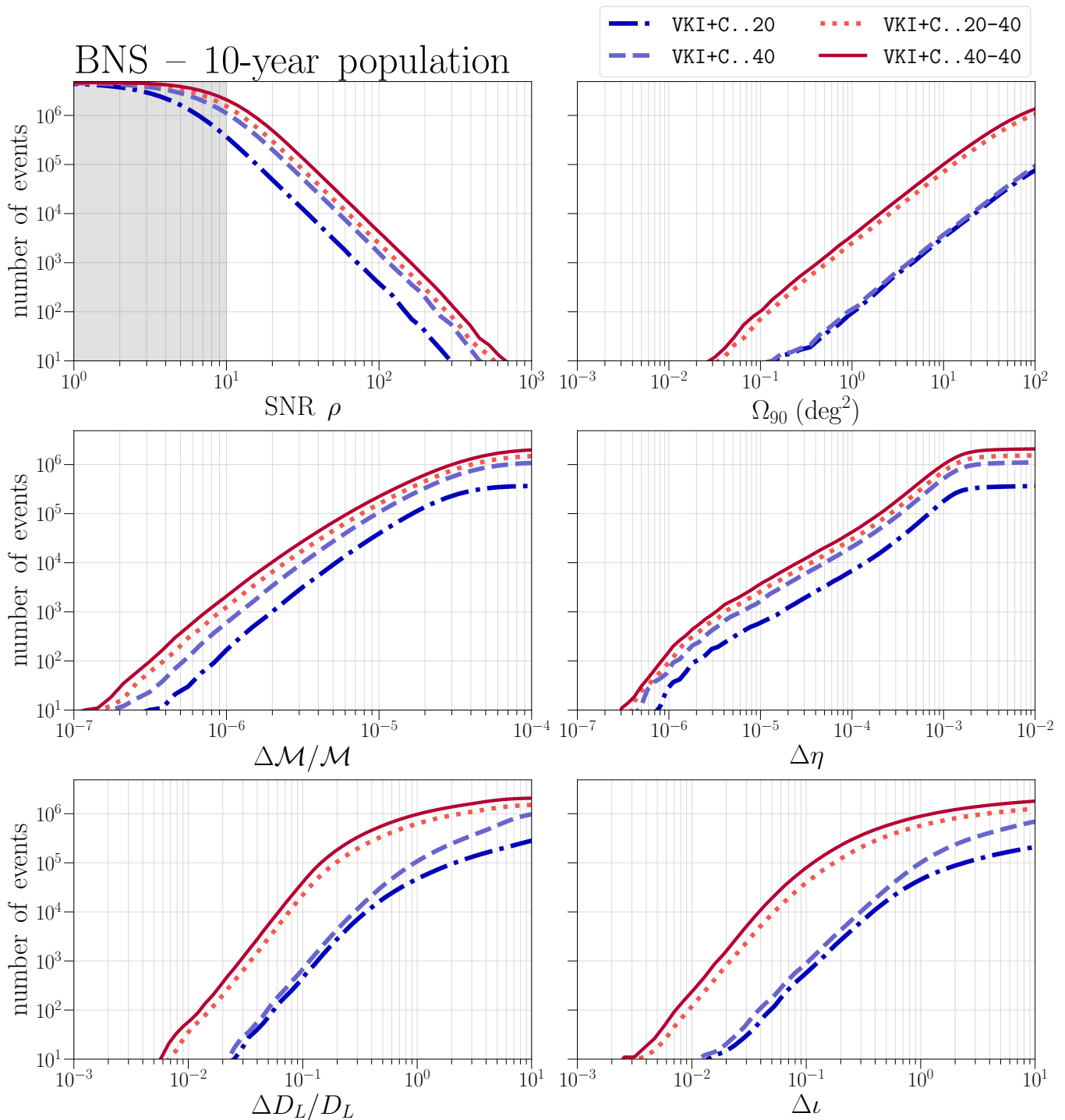| Metric	Ω_{90} (deg^2)			$\Delta D_L/D_L$	
Quality	≤ 1	≤ 0.1	≤ 0.01	≤ 0.1	≤ 0.01
BNS					
VKI+C..20	9	1	0	43	0
VKI+C..40	10	1	0	56	0
VKI+C..20-40	230	7	1	1,400	3
VKI+C..40-40	340	10	1	2,300	6
BBH					
VKI+C..20	160	7	0	470	11
VKI+C..40	180	8	0	550	21
VKI+C..20-40	840	150	5	1,000	88
VKI+C..40-40	910	200	9	1,100	130

FIG. 15. Cumulative histograms for the SNR ρ, 90%-credible sky area Ω_{90}, fractional errors on chripmass $\Delta\mathcal{M}/\mathcal{M}$ and luminosity distance $\Delta D_L/D_L$, and absolute errors on symmetric mass ratio $\Delta\eta$ and inclination angle $\Delta\iota$ for BNS mergers observed in the four studied CE networks. The histograms were generated from $\sim 4.7 \times 10^6$ injections sampled according to Sec. IV A. The non-SNR panels are obtained for events with SNR $\rho \geq 10$, indicated by the non-shaded region in the SNR panel. The SNR panel is flipped to highlight the behavior for large values.
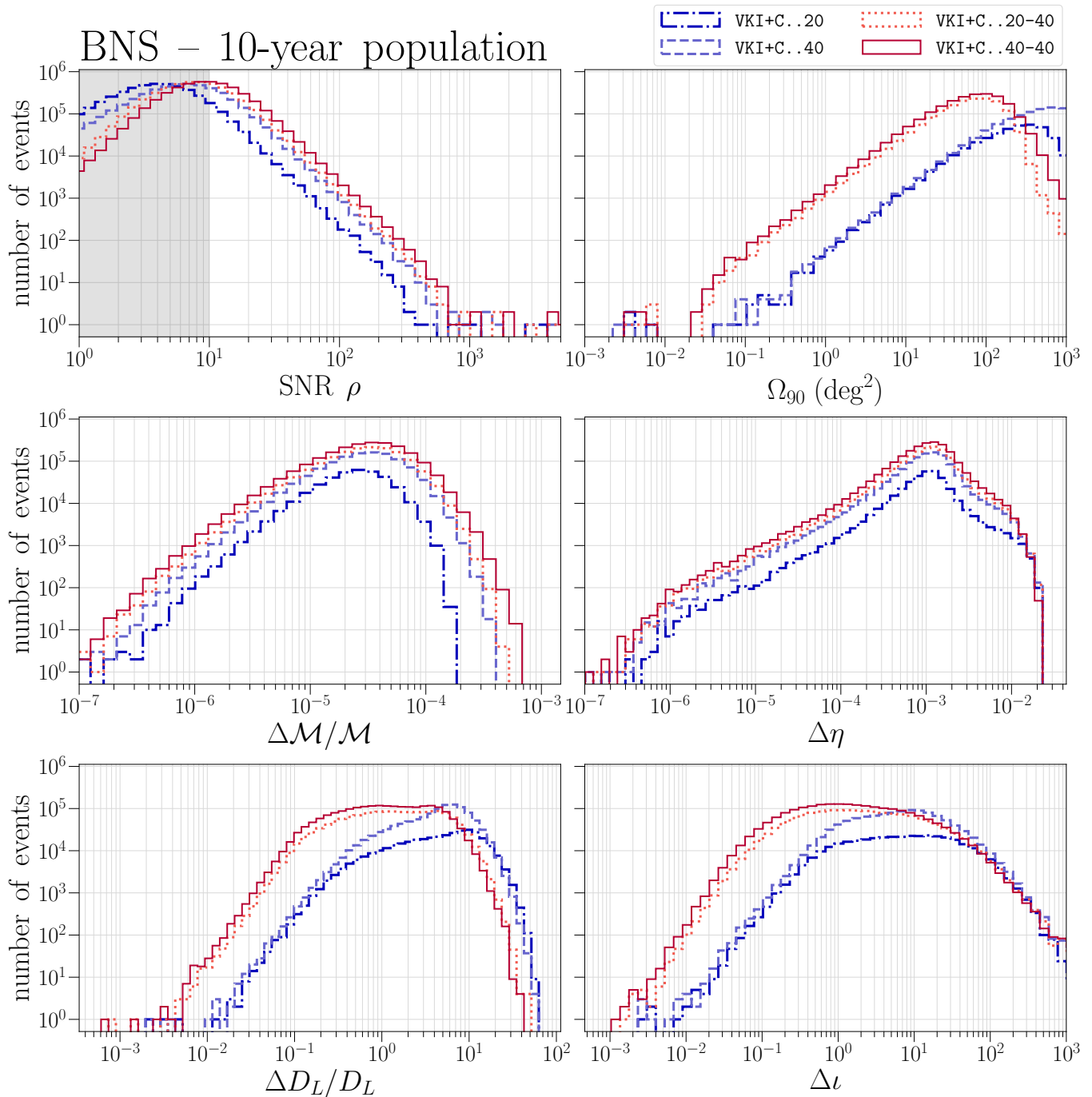
FIG. 16. Histograms of the **10 years** BNS injection sample used to generate Fig. 15 for SNR ρ, 90%-credible sky area Ω_{90}, fractional errors on chripmass $\Delta\mathcal{M}/\mathcal{M}$ and luminosity distance $\Delta D_L/D_L$, and absolute errors on symmetric mass ratio $\Delta\eta$ and the inclination angle $\Delta\iota$ observed in the four studied CE networks. The histograms were generated from $\sim 4.7 \times 10^6$ injections sampled according to Sec. IV A. The non-SNR panels are obtained for events with SNR $\rho \geq 10$, indicated by the non-shaded region in the SNR panel.
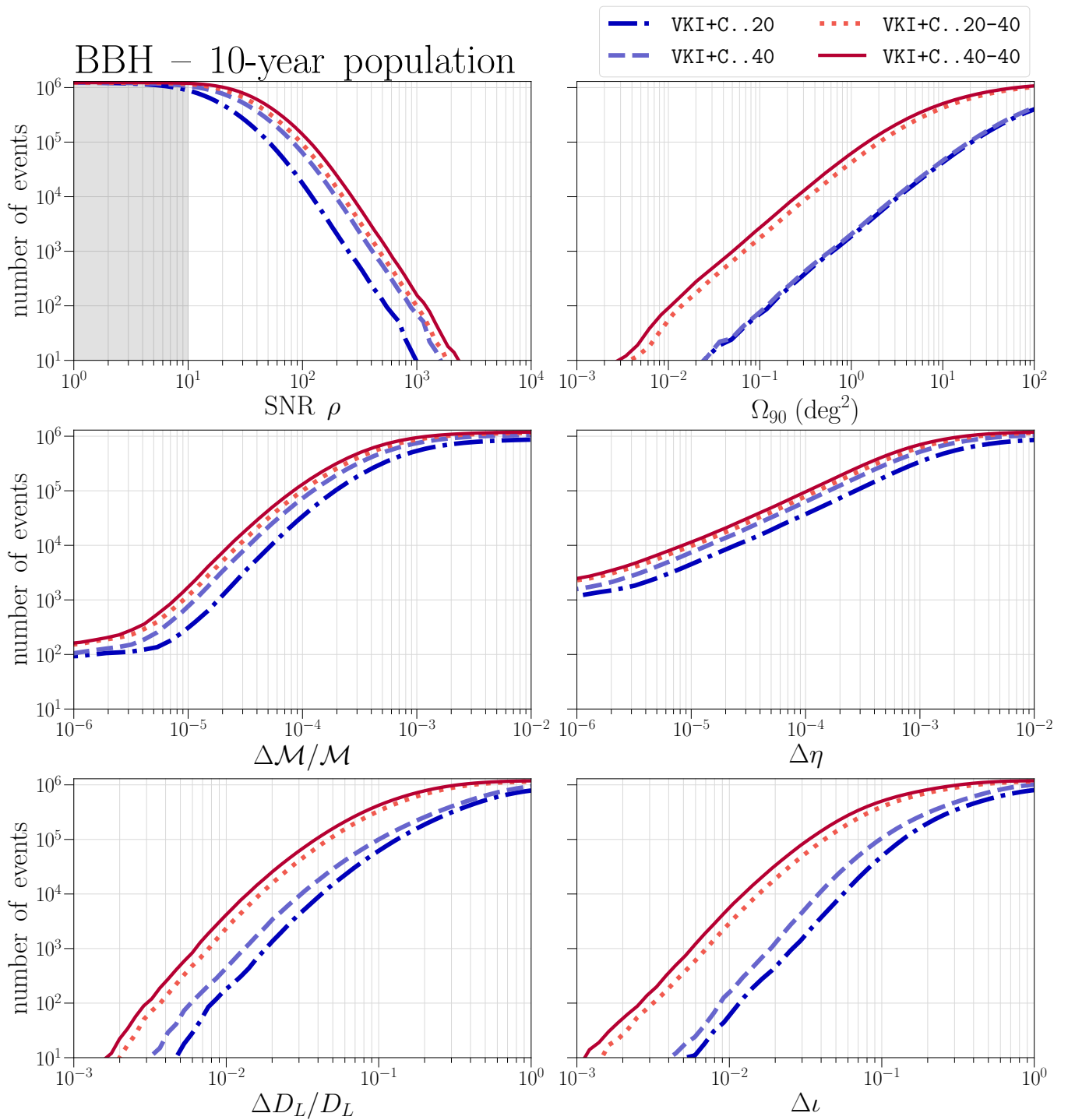
FIG. 17. Cumulative histograms for the SNR ρ, 90%-credible sky area Ω_{90}, fractional errors on chripmass $\Delta\mathcal{M}/\mathcal{M}$ and luminosity distance $\Delta D_L/D_L$, and absolute errors on symmetric mass ratio $\Delta\eta$ and inclination angle $\Delta\iota$ for BBH mergers observed in the four studied CE networks. The histograms were generated from $\sim 1.2 \times 10^6$ injections sampled according to Sec. IV A. The non-SNR panels are obtained for events with SNR $\rho \geq 10$, indicated by the non-shaded region in the SNR panel. The SNR panel is flipped to highlight the behavior for large values.
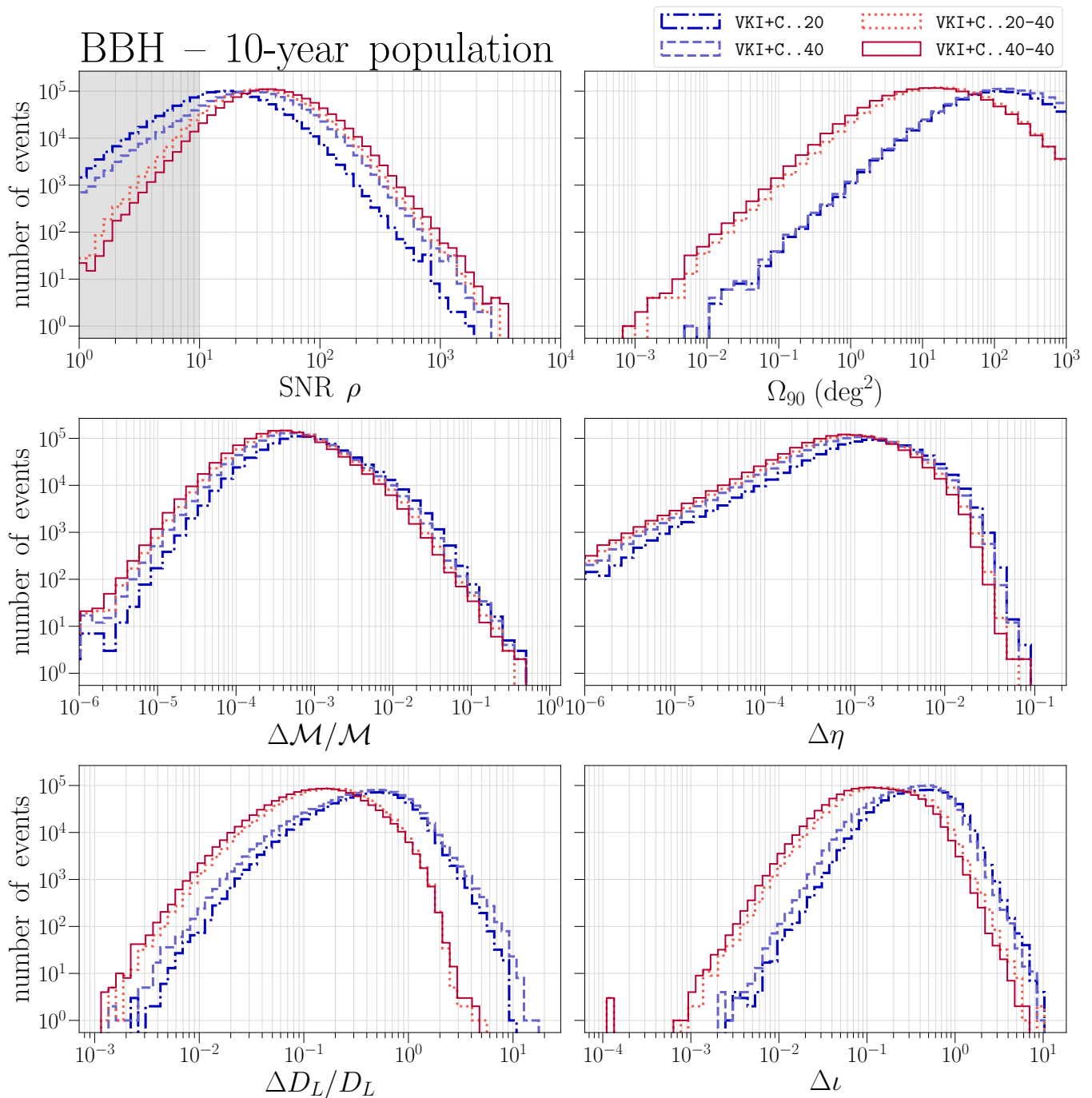
FIG. 18. Histograms of the **10 years** BBH injection sample used to generate Fig. 17 for SNR ρ, 90%-credible sky area Ω_{90}, fractional errors on chripmass $\Delta\mathcal{M}/\mathcal{M}$ and luminosity distance $\Delta D_L/D_L$, and absolute errors on symmetric mass ratio $\Delta\eta$ and the inclination angle $\Delta\iota$ observed in the four studied CE networks. The histograms were generated from $\sim 1.2 \times 10^6$ injections sampled according to Sec. IV A. The non-SNR panels are obtained for events with SNR $\rho \geq 10$, indicated by the non-shaded region in the SNR panel.
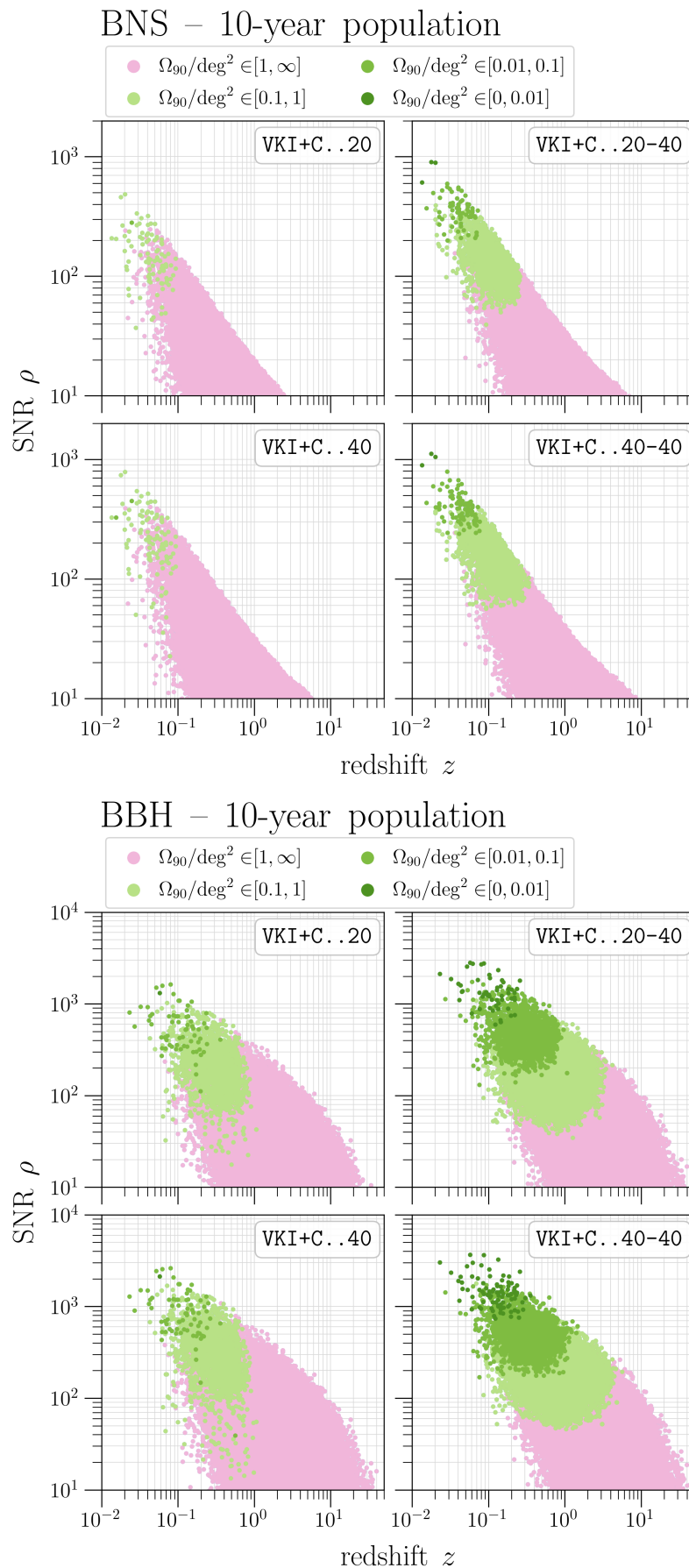
FIG. 19. The scatter plots illustrate the correlations between redshift z, SNR ρ, and 90%-credible sky area Ω_{90} for BNS (*top*) and BBH (*bottom*) mergers in the four studied CE networks.
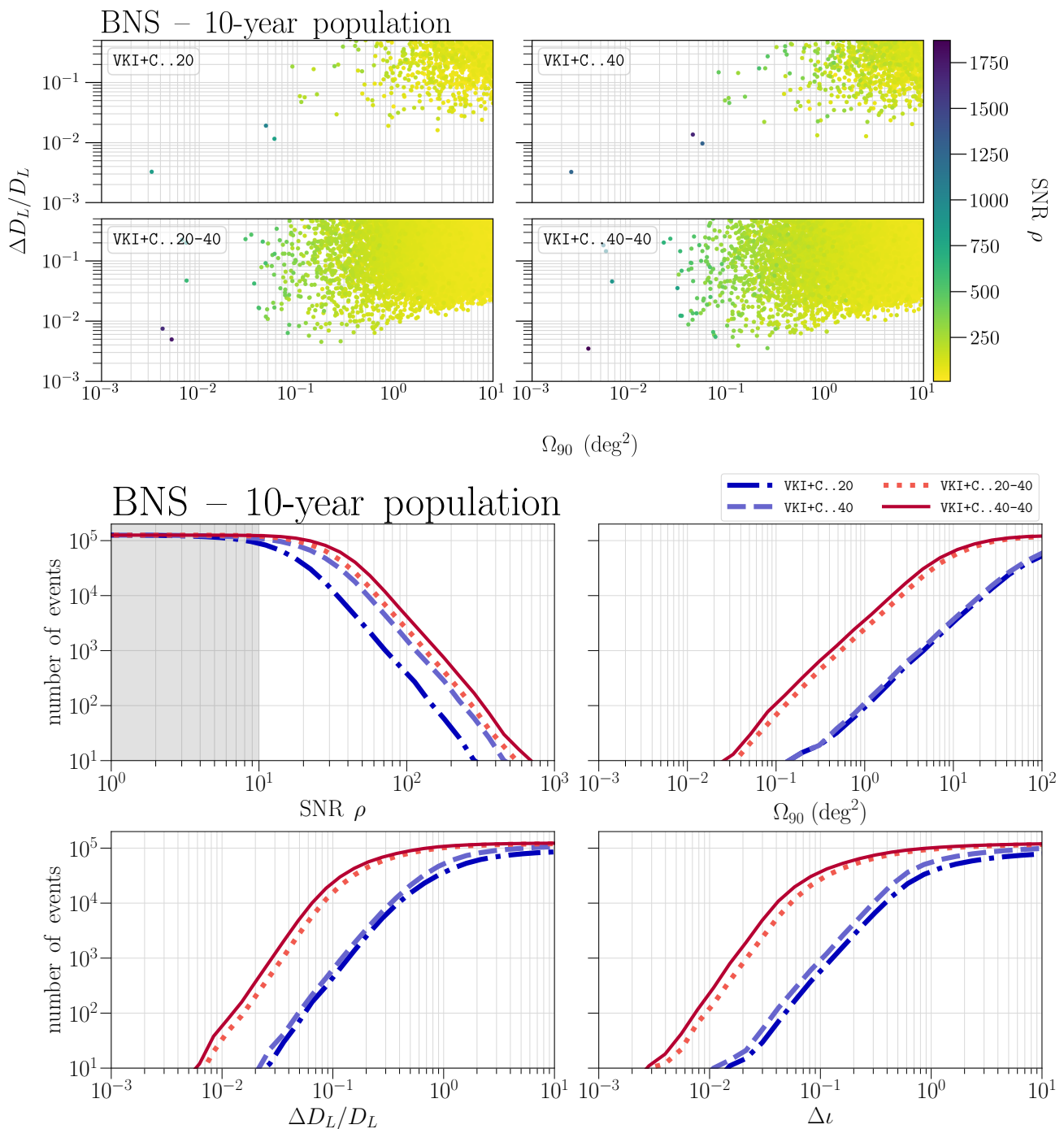
FIG. 20. *Top*: The scatter plots illustrate the correlations between SNR ρ, 90%-credible sky area Ω_{90}, and fractional luminosity distance error $\Delta D_L/D_L$ for BNS mergers with SNR $\rho \geq 10$ in the four studied CE networks for redshifts $z \leq 0.5$. The color bar indicates the SNR of the events. *Bottom:* Cumulative histograms for the SNR ρ, 90%-credible sky area Ω_{90}, fractional luminosity distance errors $\Delta D_L/D_L$, and absolute errors on the inclination angle $\Delta\iota$ for BNS mergers observed in the four studied CE networks for redshifts $z \leq 0.5$. The histograms were generated from $\sim 1.2 \times 10^5$ injections sampled according to Sec. IV A. The non-SNR panels are obtained for events with SNR $\rho \geq 10$, indicated by the non-shaded region in the SNR panel. The SNR panel is flipped to highlight the behavior for large values.

FIG. 21. *Top*: The scatter plots illustrate the correlations between SNR ρ, 90%-credible sky area Ω_{90}, and fractional luminosity distance error $\Delta D_L/D_L$ for BBH mergers with SNR $\rho \geq 10$ in the four studied CE networks for redshifts $z \leq 0.5$. The color bar indicates the SNR of the events. *Bottom:* Cumulative histograms for the SNR ρ, 90%-credible sky area Ω_{90}, fractional luminosity distance errors $\Delta D_L/D_L$, and absolute errors on the inclination angle $\Delta \iota$ for BBH mergers observed in the four studied CE networks for redshifts $z \leq 0.5$. The histograms were generated from $\sim 1.2 \times 10^4$ injections sampled according to Sec. IV A. The non-SNR panels are obtained for events with SNR $\rho \geq 10$, indicated by the non-shaded region in the SNR panel. The SNR panel is flipped to highlight the behavior for large values.
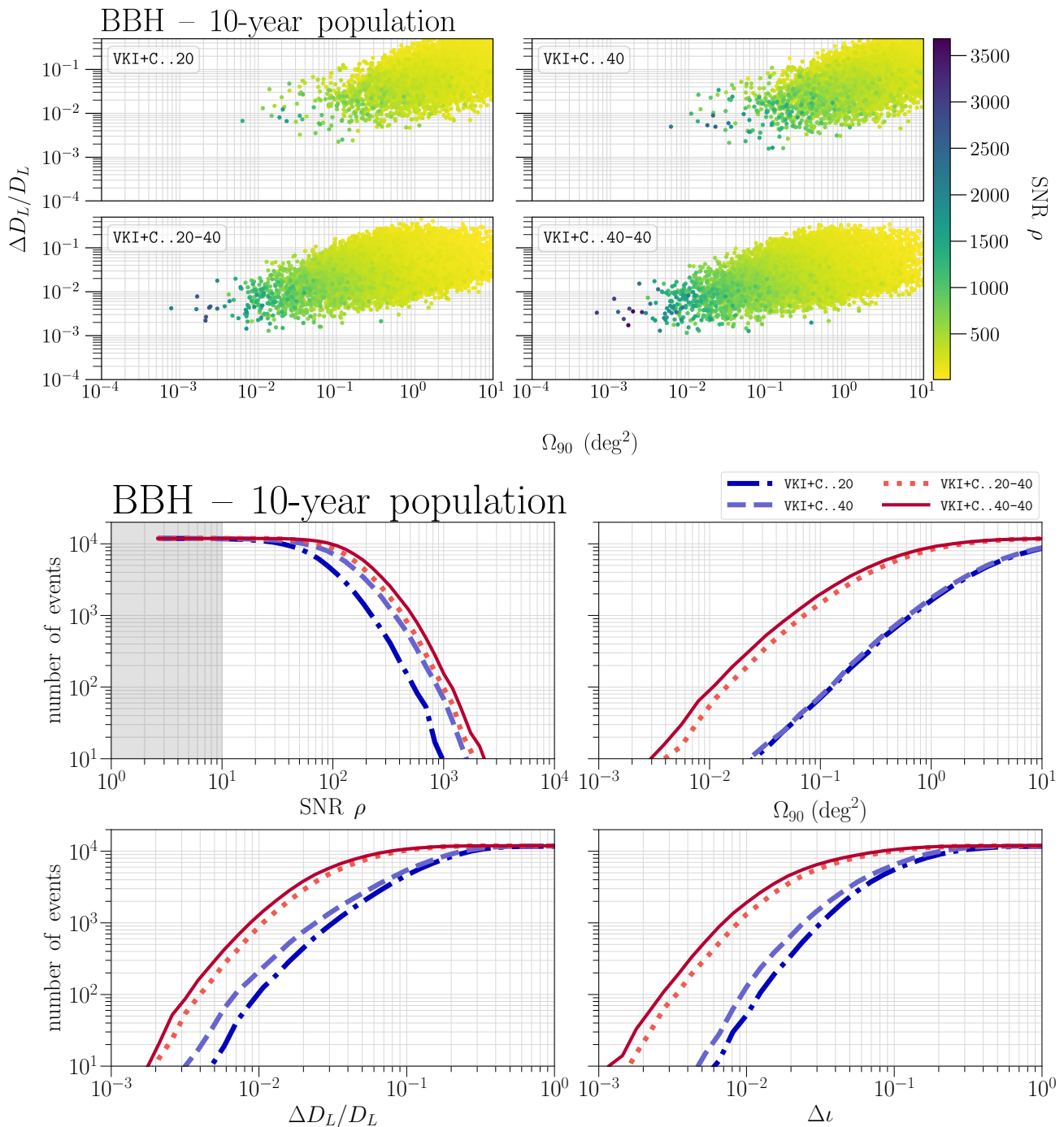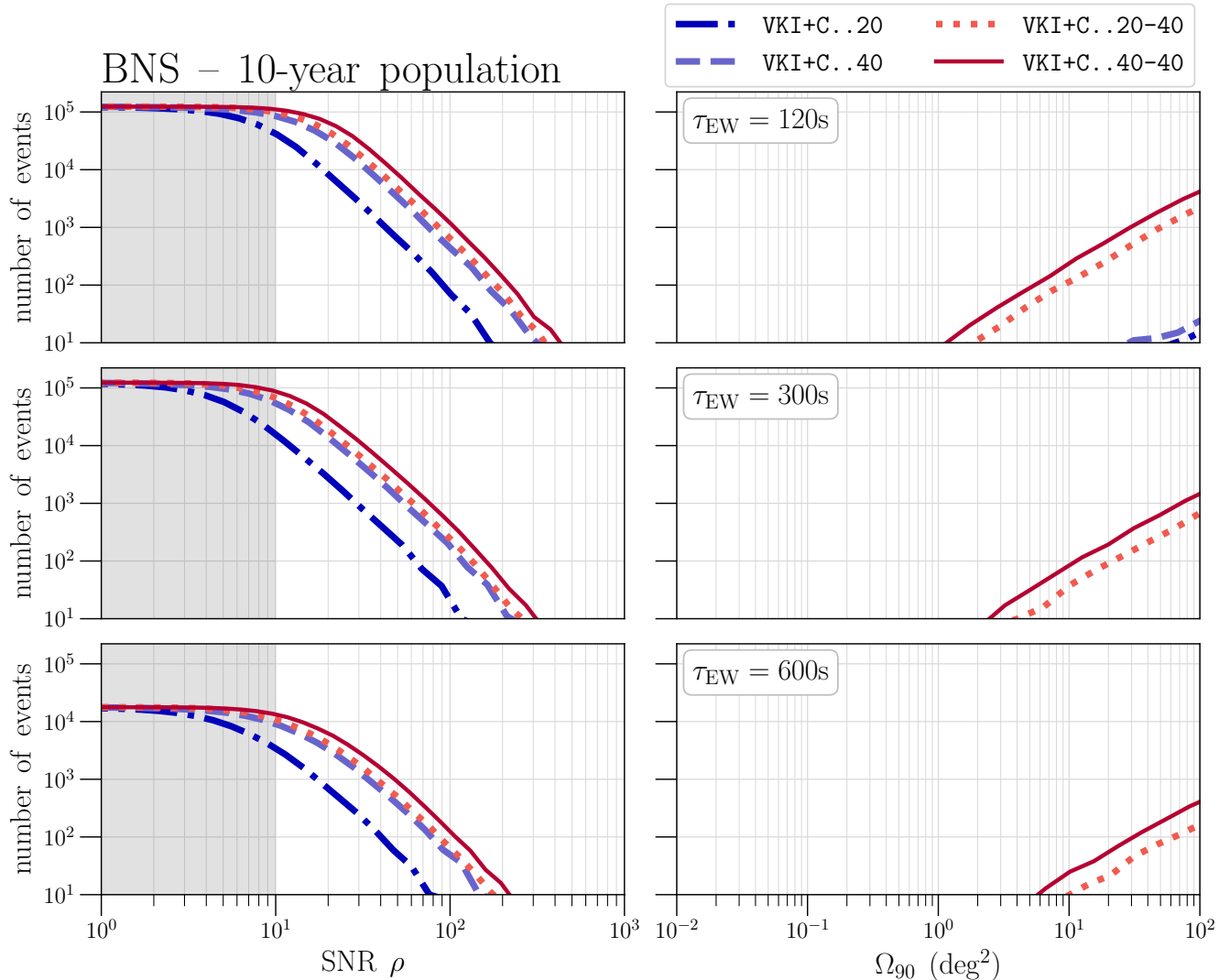
FIG. 22. Cumulative histograms for the SNR ρ and 90%-credible sky area Ω_{90} for BNS mergers observed in the four studied CE networks for redshifts $z \leq 0.5$ 2, 5, and 10 minutes before merger. The histograms were generated from $\sim 1.2 \times 10^5$ injections sampled according to Sec. IV A. The Ω_{90} panel is obtained for events with SNR $\rho \geq 10$, indicated by the non-shaded region in the SNR panel. The SNR panel is flipped to highlight the behavior for large values.

The cumulative histograms of SNR in the $\tau_{EW} = 600$ s panel do not reach the value 1 because $\sim 85\%$ of the events exhibited a cutoff-frequency $f_{EW} < 11$ Hz. Since this is too close to the lower frequency cutoff of the used V+ sensitivity curve used in half our networks, we chose to abort these runs for all networks.

TABLE XV. Number of BNS mergers events for redshifts $z \leq 0.5$ observed in the four studied CE networks that can be localized to within a small region on the sky ($\Omega_{90}/\text{deg}^2 \leq 100, 20, 10, 1$) 2, 5, and 10 minutes before merger. For a given early warning time τ_{EW} we determine the corresponding starting frequency f_{EW} using Eq. (11).

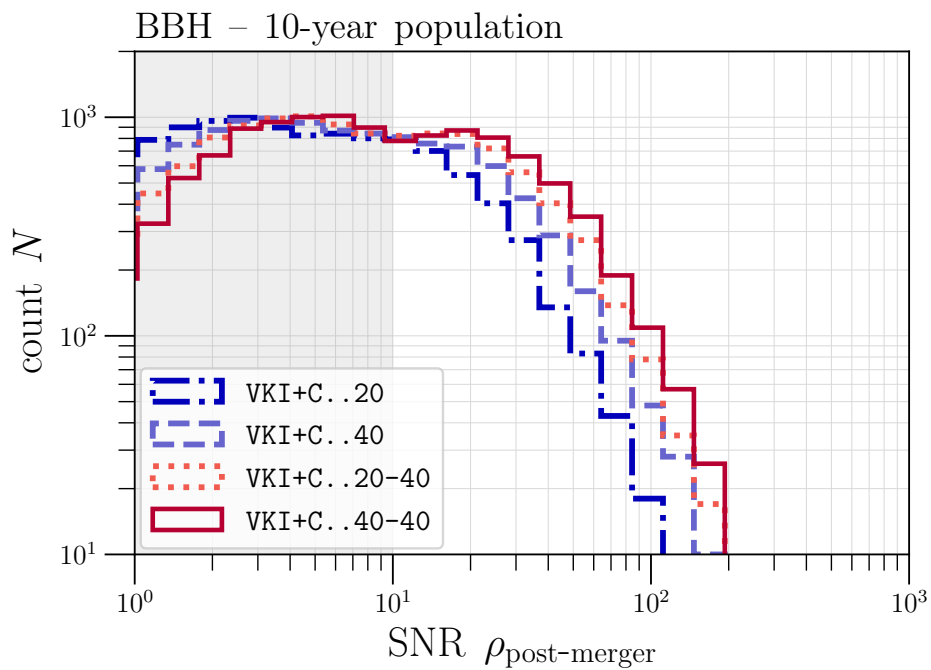| EW time	$\tau_{EW} = 120$ s				$\tau_{EW} = 300$ s				$\tau_{EW} = 600$ s			
Ω_{90} (deg²)	≤ 100	≤ 20	≤ 10	≤ 1	≤ 100	≤ 20	≤ 10	≤ 1	≤ 100	≤ 20	≤ 10	≤ 1
VKI+C..20	1	0	0	0	0	0	0	0	0	0	0	0
VKI+C..40	2	0	0	0	0	0	0	0	0	0	0	0
VKI+C..20-40	170	21	9	0	35	5	2	0	1	0	0	0
VKI+C..40-40	360	53	20	1	97	13	6	0	4	1	0	0

FIG. 23. Histograms of the SNR $\rho_{\text{post-merger}}$ in the post-merger signal of the BBH population in the four studied CE networks for redshifts $z \leq 0.5$ and a observation time of **10 years**. The histograms were generated from $\sim 1.2 \times 10^4$ injections sampled according to Sec. IV A.

[1] LIGO SCIENTIFIC collaboration, *Advanced LIGO*, *Class. Quant. Grav.* **32** (2015) 074001 [1411.4547].

[2] VIRGO collaboration, *Advanced Virgo: a second-generation interferometric gravitational wave detector*, *Class. Quant. Grav.* **32** (2015) 024001 [1408.3978].

[3] LIGO SCIENTIFIC, Virgo collaboration, *Observation of Gravitational Waves from a Binary Black Hole Merger*, *Phys. Rev. Lett.* **116** (2016) 061102 [1602.03837].

[4] LIGO SCIENTIFIC, Virgo collaboration, *GW151226: Observation of Gravitational Waves from a 22-Solar-Mass Binary Black Hole Coalescence*, *Phys. Rev. Lett.* **116** (2016) 241103 [1606.04855].

[5] LIGO SCIENTIFIC, VIRGO collaboration, *GW170104: Observation of a 50-Solar-Mass Binary Black Hole Coalescence at Redshift 0.2*, *Phys. Rev. Lett.* **118** (2017) 221101 [1706.01812].

[6] LIGO SCIENTIFIC, Virgo collaboration, *GWTC-1: A Gravitational-Wave Transient Catalog of Compact Binary Mergers Observed by LIGO and Virgo during the First and Second Observing Runs*, *Phys. Rev.* **X9** (2019) 031040 [1811.12907].

[7] LIGO SCIENTIFIC, Virgo collaboration, *GWTC-2: Compact Binary Coalescences Observed by LIGO and Virgo During the First Half of the Third Observing Run*, [2010.14527].

[8] LIGO SCIENTIFIC, Virgo collaboration, *GWTC-2: Compact Binary Coalescences Observed by LIGO and Virgo During the First Half of the Third Observing Run*, *Phys. Rev. X* **11** (2021) 021053 [2010.14527].

[9] LIGO SCIENTIFIC, Virgo collaboration, *GW170817: Observation of Gravitational Waves from a Binary Neutron Star Inspiral*, *Phys. Rev. Lett.* **119** (2017) 161101 [1710.05832].

[10] LIGO SCIENTIFIC, Virgo collaboration, *GW190425: Observation of a Compact Binary Coalescence with Total Mass $\sim 3.4 M_\odot$*, *Astrophys. J. Lett.* **892** (2020) L3 [2001.01761].

[11] LIGO SCIENTIFIC, VIRGO, KAGRA collaboration, *Observation of gravitational waves from two neutron star-black hole coalescences*, *Astrophys. J. Lett.* **915** (2021) L5 [2106.15163].

[12] LIGO SCIENTIFIC, VIRGO, FERMI GBM, INTEGRAL, ICECUBE, ASTROSAT CADMIUM ZINC TELLURIDE IMAGER TEAM, IPN, INSIGHT-HXMT, ANTARES, SWIFT, AGILE TEAM, 1M2H TEAM, DARK ENERGY CAMERA GW-EM, DES, DLT40, GRAWITA, FERMI-LAT, ATCA, ASKAP, LAS CUMBRES OBSERVATORY GROUP, OZGRAV, DWF (DEEPER WIDER FASTER PROGRAM), AST3, CAASTRO, VINROUGE, MASTER, J-GEM, GROWTH, JAGWAR, CALTECHNRAO, TTU-NRAO, NUSTAR, PAN-STARRS, MAXI TEAM, TZAC CONSORTIUM, KU, NORDIC OPTICAL TELESCOPE, EPESSTO, GROND, TEXAS TECH UNIVERSITY, SALT GROUP, TOROS, BOOTES, MWA, CALET, IKI-GW FOLLOW-UP, H.E.S.S., LOFAR, LWA, HAWC, PIERRE AUGER, ALMA, EURO VLBI TEAM, PI OF SKY, CHANDRA TEAM AT MCGILL UNIVERSITY, DFN, ATLAS TELESCOPES, HIGH TIME RESOLUTION UNIVERSE SURVEY, RIMAS, RATIR, SKA SOUTH AFRICA/MEERKAT collaboration, *Multi-messenger Observations of a Binary Neutron Star Merger*, *Astrophys. J. Lett.* **848** (2017) L12 [1710.05833].

[13] LIGO SCIENTIFIC, Virgo, FERMI-GBM, INTEGRAL collaboration, *Gravitational Waves and Gamma-rays from a Binary Neutron Star Merger: GW170817 and GRB 170817A*, *Astrophys. J. Lett.* **848** (2017) L13 [1710.05834].

[14] K. Chatziioannou et al., *On the properties of the massive binary black hole merger GW170729*, *Phys. Rev.* **D100** (2019) 104015 [1903.06742].

[15] LIGO SCIENTIFIC, Virgo collaboration, *GW190521: A Binary Black Hole Merger with a Total Mass of* $150 M_\odot$, *Phys. Rev. Lett.* **125** (2020) 101102 [2009.01075].

[16] LIGO SCIENTIFIC, Virgo collaboration, *Properties and Astrophysical Implications of the 150 $M_\odot$ Binary Black Hole Merger GW190521*, *Astrophys. J. Lett.* **900** (2020) L13 [2009.01190].

[17] LIGO SCIENTIFIC, Virgo collaboration, *GW190412: Observation of a Binary-Black-Hole Coalescence with Asymmetric Masses*, *Phys. Rev.* **D102** (2020) 043015 [2004.08342].

[18] LIGO SCIENTIFIC, Virgo collaboration, *GW190814: Gravitational Waves from the Coalescence of a 23 Solar Mass Black Hole with a 2.6 Solar Mass Compact Object*, *Astrophys. J. Lett.* **896** (2020) L44 [2006.12611].

[19] A. H. Nitz, C. Capano, A. B. Nielsen, S. Reyes, R. White, D. A. Brown et al., *1-OGC: The first open gravitational-wave catalog of binary mergers from analysis of public Advanced LIGO data*, *Astrophys. J.* **872** (2019) 195 [1811.01921].

[20] A. H. Nitz, T. Dent, G. S. Davies, S. Kumar, C. D. Capano, I. Harry et al., *2-OGC: Open Gravitational-wave Catalog of binary mergers from analysis of public Advanced LIGO and Virgo data*, *Astrophys. J.* **891** (2020) 123 [1910.05331].

[21] J. Roulet, T. Venumadhav, B. Zackay, L. Dai and M. Zaldarriaga, *Binary Black Hole Mergers from LIGO/Virgo O1 and O2: Population Inference Combining Confident and Marginal Events*, *Phys. Rev. D* **102** (2020) 123022 [2008.07014].

[22] A. H. Nitz, C. D. Capano, S. Kumar, Y.-F. Wang, S. Kastha, M. Schäfer et al., *3-OGC: Catalog of Gravitational Waves from Compact-binary Mergers*, *Astrophys. J.* **922** (2021) 76 [2105.09151].

[23] A. H. Nitz, S. Kumar, Y.-F. Wang, S. Kastha, S. Wu, M. Schäfer et al., *4-OGC: Catalog of gravitational waves from compact-binary mergers*, [2112.06878].

[24] B. Zackay, L. Dai, T. Venumadhav, J. Roulet and M. Zaldarriaga, *Detecting gravitational waves with disparate detector responses: Two new binary black hole mergers*, *Phys. Rev. D* **104** (2021) 063030 [1910.09528].

[25] B. Zackay, T. Venumadhav, L. Dai, J. Roulet and M. Zaldarriaga, *Highly spinning and aligned binary black hole merger in the Advanced LIGO first observing run*, *Phys. Rev. D* **100** (2019) 023007 [1902.10331].

[26] T. Venumadhav, B. Zackay, J. Roulet, L. Dai and M. Zaldarriaga, *New binary black hole mergers in the second observing run of Advanced LIGO and Advanced Virgo*, *Phys. Rev. D* **101** (2020) 083030 [1904.07214].

[27] H. S. Chia, S. Olsen, J. Roulet, L. Dai, T. Venumadhav, B. Zackay et al., *Boxing Day Surprise: Higher Multipoles and Orbital Precession in GW151226*, [2105.06486].

[28] S. Olsen, T. Venumadhav, J. Mushkin, J. Roulet, B. Zackay and M. Zaldarriaga, *New binary black hole mergers in the LIGO–Virgo O3a data*, [2201.02252].

[29] LIGO SCIENTIFIC, Virgo collaboration, *Tests of general relativity with GW150914*, *Phys. Rev. Lett.* **116** (2016) 221101 [1602.03841].

[30] N. Yunes, K. Yagi and F. Pretorius, *Theoretical Physics Implications of the Binary Black-Hole Mergers GW150914 and GW151226*, *Phys. Rev.* **D94** (2016) 084002 [1603.08955].

[31] LIGO SCIENTIFIC, Virgo collaboration, *Tests of General*

Relativity with GW170817, Phys. Rev. Lett. **123** (2019) 011102 [1811.00364].

[32] LIGO Scientific, Virgo collaboration, *Tests of General Relativity with the Binary Black Hole Signals from the LIGO-Virgo Catalog GWTC-1, Phys. Rev. D* **100** (2019) 104036 [1903.04467].

[33] LIGO Scientific, Virgo collaboration, *Tests of general relativity with binary black holes from the second LIGO-Virgo gravitational-wave transient catalog, Phys. Rev. D* **103** (2021) 122002 [2010.14529].

[34] LIGO Scientific, VIRGO, KAGRA collaboration, *Tests of General Relativity with GWTC-3*, [2112.06861].

[35] K. Belczynski et al., *Evolutionary roads leading to low effective spins, high black hole masses, and O1/O2 rates for LIGO/Virgo binary black holes, Astron. Astrophys.* **636** (2020) A104 [1706.07053].

[36] K. Belczynski et al., *Binary neutron star formation and the origin of GW170817*, [1812.10065].

[37] A. Gupta, D. Gerosa, K. G. Arun, E. Berti, W. M. Farr and B. S. Sathyaprakash, *Black holes in the low mass gap: Implications for gravitational wave observations, Phys. Rev. D* **101** (2020) 103036 [1909.05804].

[38] M. Fishbach and D. E. Holz, *Picky Partners: The Pairing of Component Masses in Binary Black Hole Mergers, Astrophys. J. Lett.* **891** (2020) L27 [1905.12669].

[39] M. Fishbach and D. E. Holz, *Minding the gap: GW190521 as a straddling binary, Astrophys. J. Lett.* **904** (2020) L26 [2009.05472].

[40] D. Gerosa, S. Vitale and E. Berti, *Astrophysical implications of GW190412 as a remnant of a previous black-hole merger, Phys. Rev. Lett.* **125** (2020) 101103 [2005.04243].

[41] M. Zevin, S. S. Bavera, C. P. L. Berry, V. Kalogera, T. Fragos, P. Marchant et al., *One Channel to Rule Them All? Constraining the Origins of Binary Black Holes Using Multiple Formation Pathways, Astrophys. J.* **910** (2021) 152 [2011.10057].

[42] M. Zevin, M. Spera, C. P. L. Berry and V. Kalogera, *Exploring the Lower Mass Gap and Unequal Mass Regime in Compact Binary Evolution, Astrophys. J. Lett.* **899** (2020) L1 [2006.14573].

[43] A. Olejak and K. Belczynski, *The Implications of High BH Spins on the Origin of BH–BH Mergers, Astrophys. J. Lett.* **921** (2021) L2 [2109.06872].

[44] V. Baibhav, E. Berti, D. Gerosa, M. Mould and K. W. K. Wong, *Looking for the parents of LIGO's black holes, Phys. Rev. D* **104** (2021) 084002 [2105.12140].

[45] P. Mahapatra, A. Gupta, M. Favata, K. G. Arun and B. S. Sathyaprakash, *Remnant Black Hole Kicks and Implications for Hierarchical Mergers, Astrophys. J. Lett.* **918** (2021) L31 [2106.07179].

[46] M. Fishbach, Z. Doctor, T. Callister, B. Edelman, J. Ye, R. Essick et al., *When Are LIGO/Virgo's Big Black Hole Mergers?, Astrophys. J.* **912** (2021) 98 [2101.07699].

[47] B. F. Schutz, *Determining the Hubble Constant from Gravitational Wave Observations, Nature* **323** (1986) 310.

[48] LIGO Scientific, Virgo, 1M2H, Dark Energy Camera GW-E, DES, DLT40, Las Cumbres Observatory, VINROUGE, MASTER collaboration, *A gravitational-wave standard siren measurement of the Hubble constant, Nature* **551** (2017) 85 [1710.05835].

[49] S. Mukherjee, B. D. Wandelt and J. Silk, *Probing the theory of gravity with gravitational lensing of gravitational waves and galaxy surveys, Mon. Not. Roy. Astron. Soc.* **494** (2020) 1956 [1908.08951].

[50] X. Shao, Z. Cao, X. Fan and S. Wu, *Probing the Large-scale Structure of the Universe Through Gravitational Wave Observations, Res. Astron. Astrophys.* **22** (2022) 015006 [2110.08978].

[51] S. Libanore, M. C. Artale, D. Karagiannis, M. Liguori, N. Bartolo, Y. Bouffanais et al., *Gravitational Wave mergers as tracers of Large Scale Structures, JCAP* **02** (2021) 035 [2007.06905].

[52] A. Vijaykumar, M. V. S. Saketh, S. Kumar, P. Ajith and T. R. Choudhury, *Probing the large scale structure using gravitational-wave observations of binary black holes*, [2005.01111].

[53] E. E. Flanagan and T. Hinderer, *Constraining neutron star tidal Love numbers with gravitational wave detectors, Phys. Rev.* **D77** (2008) 021502 [0709.1915].

[54] S. De, D. Finstad, J. M. Lattimer, D. A. Brown, E. Berger and C. M. Biwer, *Tidal Deformabilities and Radii of Neutron Stars from the Observation of GW170817, Phys. Rev. Lett.* **121** (2018) 091102 [1804.08583].

[55] LIGO Scientific, Virgo collaboration, *GW170817: Measurements of neutron star radii and equation of state, Phys. Rev. Lett.* **121** (2018) 161101 [1805.11581].

[56] M. Nicholl, B. Margalit, P. Schmidt, G. P. Smith, E. J. Ridley and J. Nuttall, *Tight multimessenger constraints on the neutron star equation of state from GW170817 and a forward model for kilonova light-curve synthesis, Mon. Not. Roy. Astron. Soc.* **505** (2021) 3016 [2102.02229].

[57] I. Tews, J. Margueron and S. Reddy, *Constraining the properties of dense matter and neutron stars by combining nuclear physics and gravitational waves from GW170817, AIP Conf. Proc.* **2127** (2019) 020009 [1905.11212].

[58] C. A. Raithel, *Constraints on the Neutron Star Equation of State from GW170817, Eur. Phys. J. A* **55** (2019) 80 [1904.10002].

[59] Y. Lim and J. W. Holt, *Bayesian modeling of the nuclear equation of state for neutron star tidal deformabilities and GW170817, Eur. Phys. J. A* **55** (2019) 209 [1902.05502].

[60] T. Malik, N. Alam, M. Fortin, C. Providência, B. K. Agrawal, T. K. Jha et al., *GW170817: constraining the nuclear matter equation of state from the neutron star tidal deformability, Phys. Rev. C* **98** (2018) 035804 [1805.11963].

[61] I. Tews, J. Margueron and S. Reddy, *Critical examination of constraints on the equation of state of dense matter obtained from GW170817, Phys. Rev. C* **98** (2018) 045804 [1804.02783].

[62] D. Radice, A. Perego, F. Zappa and S. Bernuzzi, *GW170817: Joint Constraint on the Neutron Star Equation of State from Multimessenger Observations, Astrophys. J. Lett.* **852** (2018) L29 [1711.03647].

[63] S. Kumar, A. Vijaykumar and A. H. Nitz, *Detecting Baryon Acoustic Oscillations with Third-generation Gravitational Wave Observatories, Astrophys. J.* **930** (2022) 113 [2110.06152].

[64] LIGO Scientific, VIRGO, KAGRA collaboration, *GWTC-3: Compact Binary Coalescences Observed by LIGO and Virgo During the Second Part of the Third Observing Run*, [2111.03606].

[65] M. R. Drout et al., *Light Curves of the Neutron Star Merger GW170817/SSS17a: Implications for R-Process Nucleosynthesis, Science* **358** (2017) 1570 [1710.05443].

[66] D. A. Coulter et al., *Swope Supernova Survey 2017a (SSS17a), the Optical Counterpart to a Gravitational Wave Source, Science* (2017) [1710.05452].

[67] P. S. Cowperthwaite et al., *The Electromagnetic Counterpart of the Binary Neutron Star Merger LIGO/Virgo GW170817. II. UV, Optical, and Near-infrared Light Curves and Comparison to Kilonova Models, Astrophys. J. Lett.* **848** (2017) L17 [1710.05840].

[68] D. Kasen, B. Metzger, J. Barnes, E. Quataert and E. Ramirez-Ruiz, *Origin of the heavy elements in binary neutron-star mergers from a gravitational wave event*, *Nature* (2017) [1710.05463].

[69] DES, Dark Energy Camera GW-EM collaboration, *The Electromagnetic Counterpart of the Binary Neutron Star Merger LIGO/Virgo GW170817. I. Discovery of the Optical Counterpart Using the Dark Energy Camera*, *Astrophys. J. Lett.* **848** (2017) L16 [1710.05459].

[70] S. Valenti, D. J. Sand, S. Yang, E. Cappellaro, L. Tartaglia, A. Corsi et al., *The discovery of the electromagnetic counterpart of GW170817: kilonova AT 2017gfo/DLT17ck*, *Astrophys. J. Lett.* **848** (2017) L24 [1710.05854].

[71] I. Arcavi et al., *Optical emission from a kilonova following a gravitational-wave-detected neutron-star merger*, *Nature* **551** (2017) 64 [1710.05843].

[72] N. R. Tanvir et al., *The Emergence of a Lanthanide-Rich Kilonova Following the Merger of Two Neutron Stars*, *Astrophys. J. Lett.* **848** (2017) L27 [1710.05455].

[73] V. M. Lipunov et al., *MASTER Optical Detection of the First LIGO/Virgo Neutron Star Binary Merger GW170817*, *Astrophys. J. Lett.* **850** (2017) L1 [1710.05461].

[74] P. A. Evans et al., *Swift and NuSTAR observations of GW170817: detection of a blue kilonova*, *Science* **358** (2017) 1565 [1710.05437].

[75] P. Creminelli and F. Vernizzi, *Dark Energy after GW170817 and GRB170817A*, *Phys. Rev. Lett.* **119** (2017) 251302 [1710.05877].

[76] J. M. Ezquiaga and M. Zumalacárregui, *Dark Energy After GW170817: Dead Ends and the Road Ahead*, *Phys. Rev. Lett.* **119** (2017) 251304 [1710.05901].

[77] K. Hotokezaka, E. Nakar, O. Gottlieb, S. Nissanke, K. Masuda, G. Hallinan et al., *A Hubble constant measurement from superluminal motion of the jet in GW170817*, *Nature Astron.* **3** (2019) 940 [1806.10596].

[78] S. Mukherjee, A. Ghosh, M. J. Graham, C. Karathanasis, M. M. Kasliwal, I. Magaña Hernandez et al., *First measurement of the Hubble parameter from bright binary black hole GW190521*, [2009.14199].

[79] H.-Y. Chen, M. Fishbach and D. E. Holz, *A two per cent Hubble constant measurement from standard sirens within five years*, *Nature* **562** (2018) 545 [1712.06531].

[80] S. Borhanian, A. Dhani, A. Gupta, K. G. Arun and B. S. Sathyaprakash, *Dark Sirens to Resolve the Hubble–Lemaître Tension*, *Astrophys. J. Lett.* **905** (2020) L28 [2007.02883].

[81] S. Mukherjee, B. D. Wandelt, S. M. Nissanke and A. Silvestri, *Accurate precision Cosmology with redshift unknown gravitational wave sources*, *Phys. Rev. D* **103** (2021) 043520 [2007.02943].

[82] B. Margalit and B. D. Metzger, *Constraining the Maximum Mass of Neutron Stars From Multi-Messenger Observations of GW170817*, *Astrophys. J. Lett.* **850** (2017) L19 [1710.05938].

[83] M. Ruiz, S. L. Shapiro and A. Tsokaros, *GW170817, General Relativistic Magnetohydrodynamic Simulations, and the Neutron Star Maximum Mass*, *Phys. Rev. D* **97** (2018) 021501 [1711.00473].

[84] E. R. Most, L. R. Weih, L. Rezzolla and J. Schaffner-Bielich, *New constraints on radii and tidal deformabilities of neutron stars from GW170817*, *Phys. Rev. Lett.* **120** (2018) 261103 [1803.00549].

[85] M. Shibata, E. Zhou, K. Kiuchi and S. Fujibayashi, *Constraint on the maximum mass of neutron stars using GW170817 event*, *Phys. Rev. D* **100** (2019) 023015 [1905.03656].

[86] D. A. Godzieba, D. Radice and S. Bernuzzi, *On the maximum mass of neutron stars and GW190814*, *Astrophys. J.* **908** (2021) 122 [2007.10999].

[87] S. Clesse and J. García-Bellido, *The clustering of massive Primordial Black Holes as Dark Matter: measuring their mass distribution with Advanced LIGO*, *Phys. Dark Univ.* **15** (2017) 142 [1603.05234].

[88] M. Sasaki, T. Suyama, T. Tanaka and S. Yokoyama, *Primordial Black Hole Scenario for the Gravitational-Wave Event GW150914*, *Phys. Rev. Lett.* **117** (2016) 061101 [1603.08338].

[89] S. Bird, I. Cholis, J. B. Muñoz, Y. Ali-Haïmoud, M. Kamionkowski, E. D. Kovetz et al., *Did LIGO detect dark matter?*, *Phys. Rev. Lett.* **116** (2016) 201301 [1603.00464].

[90] B. Carr, F. Kuhnel and M. Sandstad, *Primordial Black Holes as Dark Matter*, *Phys. Rev. D* **94** (2016) 083504 [1607.06077].

[91] A. Kashlinsky, *LIGO gravitational wave detection, primordial black holes and the near-IR cosmic infrared background anisotropies*, *Astrophys. J. Lett.* **823** (2016) L25 [1605.04023].

[92] R. Saito and J. Yokoyama, *Gravitational-Wave Constraints on the Abundance of Primordial Black Holes*, *Prog. Theor. Phys.* **123** (2010) 867 [0912.5317].

[93] G. Franciolini, *Primordial Black Holes: from Theory to Gravitational Wave Observations*, Ph.D. thesis, Geneva U., Dept. Theor. Phys., 2021. [2110.06815]. 10.13097/archive-ouverte/unige:156136.

[94] LIGO Scientific, Virgo collaboration, *GW150914: Implications for the stochastic gravitational wave background from binary black holes*, *Phys. Rev. Lett.* **116** (2016) 131102 [1602.03847].

[95] T. Regimbau, M. Evans, N. Christensen, E. Katsavounidis, B. Sathyaprakash and S. Vitale, *Digging deeper: Observing primordial gravitational waves below the binary black hole produced stochastic background*, *Phys. Rev. Lett.* **118** (2017) 151105 [1611.08943].

[96] LIGO Scientific, Virgo collaboration, *GW170817: Implications for the Stochastic Gravitational-Wave Background from Compact Binary Coalescences*, *Phys. Rev. Lett.* **120** (2018) 091101 [1710.05837].

[97] KAGRA, LIGO Scientific, VIRGO collaboration, *Prospects for Observing and Localizing Gravitational-Wave Transients with Advanced LIGO, Advanced Virgo and KAGRA*, *Living Rev. Rel.* **21** (2018) 3 [1304.0670].

[98] D. Reitze et al., *Cosmic Explorer: The U.S. Contribution to Gravitational-Wave Astronomy beyond LIGO*, *Bull. Am. Astron. Soc.* **51** (2019) 035 [1907.04833].

[99] KAGRA collaboration, *KAGRA: 2.5 Generation Interferometric Gravitational Wave Detector*, *Nature Astron.* **3** (2019) 35 [1811.08079].

[100] KAGRA collaboration, *Overview of KAGRA: Detector design and construction history*, [2005.05574].

[101] C. S. Unnikrishnan, *IndIGO and LIGO-India: Scope and plans for gravitational wave research and precision metrology in India*, *Int. J. Mod. Phys. D* **22** (2013) 1341010 [1510.06059].

[102] M. Saleem et al., *The science case for LIGO-India*, *Class. Quant. Grav.* **39** (2022) 025004 [2105.01716].

[103] A. G. Riess, S. Casertano, W. Yuan, L. M. Macri and D. Scolnic, *Large Magellanic Cloud Cepheid Standards Provide a 1% Foundation for the Determination of the Hubble Constant and Stronger Evidence for Physics beyond ΛCDM*, *Astrophys. J.* **876** (2019) 85 [1903.07603].

[104] LIGO collaboration, *A cryogenic silicon interferometer for gravitational-wave detection*, *Class. Quant. Grav.* **37** (2020) 165003 [2001.11173].

[105] M. Punturo et al., *The Einstein Telescope: A third-generation gravitational wave observatory*, *Class. Quant. Grav.* **27** (2010) 194002.

[106] S. Hild et al., *Sensitivity Studies for Third-Generation Gravitational Wave Observatories*, *Class. Quant. Grav.* **28** (2011) 094013 [`1012.0908`].

[107] LIGO Scientific collaboration, *Exploring the Sensitivity of Next Generation Gravitational Wave Detectors*, *Class. Quant. Grav.* **34** (2017) 044001 [`1607.08697`].

[108] K. Ackley et al., *Neutron Star Extreme Matter Observatory: A kilohertz-band gravitational-wave detector in the global network*, *Publ. Astron. Soc. Austral.* **37** (2020) e047 [`2007.03128`].

[109] B. S. Sathyaprakash, B. F. Schutz and C. Van Den Broeck, *Cosmography with the Einstein Telescope*, *Class. Quant. Grav.* **27** (2010) 215006 [`0906.4151`].

[110] M. Punturo et al., *The third generation of gravitational wave observatories and their science reach*, *Class. Quant. Grav.* **27** (2010) 084007.

[111] W. Zhao, C. Van Den Broeck, D. Baskaran and T. G. F. Li, *Determination of Dark Energy by the Einstein Telescope: Comparing with CMB, BAO and SNIa Observations*, *Phys. Rev. D* **83** (2011) 023005 [`1009.0206`].

[112] B. Sathyaprakash et al., *Scientific Objectives of Einstein Telescope*, *Class. Quant. Grav.* **29** (2012) 124013 [`1206.0331`].

[113] S. Vitale and M. Evans, *Parameter estimation for binary black holes with networks of third generation gravitational-wave detectors*, *Phys. Rev. D* **95** (2017) 064052 [`1610.06917`].

[114] S. Vitale and C. Whittle, *Characterization of binary black holes by heterogeneous gravitational-wave networks*, *Phys. Rev. D* **98** (2018) 024029 [`1804.07866`].

[115] R. X. Adhikari et al., *Astrophysical science metrics for next-generation gravitational-wave detectors*, *Class. Quant. Grav.* **36** (2019) 245010 [`1905.02842`].

[116] E. D. Hall and M. Evans, *Metrics for next-generation gravitational-wave detectors*, *Class. Quant. Grav.* **36** (2019) 225002 [`1902.09485`].

[117] B. S. Sathyaprakash et al., *Cosmology and the Early Universe*, [`1903.09260`].

[118] B. S. Sathyaprakash et al., *Multimessenger Universe with Gravitational Waves from Binaries*, [`1903.09277`].

[119] B. S. Sathyaprakash et al., *Extreme Gravity and Fundamental Physics*, [`1903.09221`].

[120] V. Kalogera et al., *Deeper, Wider, Sharper: Next-Generation Ground-Based Gravitational-Wave Observations of Binary Black Holes*, [`1903.09220`].

[121] M. Maggiore et al., *Science Case for the Einstein Telescope*, *JCAP* **03** (2020) 050 [`1912.02622`].

[122] M. Evans et al., *A Horizon Study for Cosmic Explorer: Science, Observatories, and Community*, [`2109.09882`].

[123] M. Bailes et al., *Gravitational-wave physics and astronomy in the 2020s and 2030s*, *Nature Rev. Phys.* **3** (2021) 344.

[124] V. Kalogera et al., *The Next Generation Global Gravitational Wave Observatory: The Science Book*, [`2111.06990`].

[125] T. Yang, *Gravitational-Wave Detector Networks: Standard Sirens on Cosmology and Modified Gravity Theory*, *JCAP* **05** (2021) 044 [`2103.01923`].

[126] S.-J. Jin, T.-N. Li, J.-F. Zhang and X. Zhang, *Prospects for measuring the Hubble constant and dark energy using gravitational-wave dark sirens with neutron star tidal deformation*, *JCAP* **08** (2023) 070 [`2202.11882`].

[127] S.-J. Jin, D.-Z. He, Y. Xu, J.-F. Zhang and X. Zhang, *Forecast for cosmological parameter estimation with gravitational-wave standard siren observation from the Cosmic Explorer*, *JCAP* **03** (2020) 051 [`2001.05393`].

[128] S.-J. Jin, L.-F. Wang, P.-J. Wu, J.-F. Zhang and X. Zhang, *How can gravitational-wave standard sirens and 21-cm intensity mapping jointly provide a precise late-universe cosmological probe?*, *Phys. Rev. D* **104** (2021) 103507 [`2106.01859`].

[129] J.-F. Zhang, M. Zhang, S.-J. Jin, J.-Z. Qi and X. Zhang, *Cosmological parameter estimation with future gravitational wave standard siren observation from the Einstein Telescope*, *JCAP* **09** (2019) 068 [`1907.03238`].

[130] M. Branchesi et al., *Science with the Einstein Telescope: a comparison of different designs*, *JCAP* **07** (2023) 068 [`2303.15923`].

[131] B. Goncharov, A. H. Nitz and J. Harms, *Utilizing the null stream of the Einstein Telescope*, *Phys. Rev. D* **105** (2022) 122007 [`2204.08533`].

[132] S. Borhanian, GWBENCH*: A novel Fisher information package for gravitational-wave benchmarking*, [`2010.15202`].

[133] L. Barsotti, L. McCuller, M.Evans and P. Fritschel, *The A+ Design Curve*, (2018), https://dcc.ligo.org/LIGO-T1800042/public.

[134] LIGO Scientific, Virgo collaboration, *Population Properties of Compact Objects from the Second LIGO-Virgo Gravitational-Wave Transient Catalog*, [`2010.14533`].

[135] C. Cutler and E. E. Flanagan, *Gravitational waves from merging compact binaries: How accurately can one extract the binary's parameters from the inspiral wave form?*, *Phys. Rev. D* **49** (1994) 2658 [`gr-qc/9402014`].

[136] E. Poisson and C. M. Will, *Gravitational waves from inspiraling compact binaries: Parameter estimation using second postNewtonian wave forms*, *Phys. Rev. D* **52** (1995) 848 [`gr-qc/9502040`].

[137] R. Balasubramanian, B. Sathyaprakash and S. Dhurandhar, *Gravitational waves from coalescing binaries: Detection strategies and Monte Carlo estimation of parameters*, *Phys. Rev. D* **53** (1996) 3033 [`gr-qc/9508011`].

[138] K. G. Arun, B. R. Iyer, B. S. Sathyaprakash and P. A. Sundararajan, *Parameter estimation of inspiralling compact binaries using 3.5 post-Newtonian gravitational wave phasing: The Non-spinning case*, *Phys. Rev. D* **71** (2005) 084008 [`gr-qc/0411146`].

[139] LIGO Scientific Collaboration et al., *LSC Algorithm Library Suite*, (2020), https://doi.org/10.7935/GT1W-FZ16.

[140] F. Iacovelli, M. Mancarella, S. Foffa and M. Maggiore, *GWFAST: A Fisher Information Matrix Python Code for Third-generation Gravitational-wave Detectors*, *Astrophys. J. Supp.* **263** (2022) 2 [`2207.06910`].

[141] U. Dupletsa, J. Harms, B. Banerjee, M. Branchesi, B. Goncharov, A. Maselli et al., *gwfish: A simulation software to evaluate parameter-estimation capabilities of gravitational-wave detector networks*, *Astron. Comput.* **42** (2023) 100671 [`2205.02499`].

[142] T. Dietrich, A. Samajdar, S. Khan, N. K. Johnson-McDaniel, R. Dudi and W. Tichy, *Improving the NRTidal model for binary neutron star systems*, *Phys. Rev. D* **100** (2019) 044003 [`1905.06011`].

[143] C. García-Quirós, M. Colleoni, S. Husa, H. Estellés, G. Pratten, A. Ramos-Buades et al., *Multimode frequency-domain model for the gravitational wave signal from nonprecessing black-hole binaries*, *Phys. Rev. D* **102** (2020) 064002 [`2001.10914`].

[144] C. García-Quirós, S. Husa, M. Mateu-Lucena and A. Borchers, *Accelerating the evaluation of inspiral–merger–ringdown waveforms with adapted grids*, *Class. Quant. Grav.* **38** (2021) 015006 [`2001.10897`].

[145] L. P. Singer and L. R. Price, *Rapid Bayesian position reconstruction for gravitational-wave transients*, *Phys. Rev. D* **93** (2016) 024013 [`1508.03634`].

[146] R. Magee and S. Borhanian, *Realistic observing scenarios for the next decade of early warning detection of binary neutron stars*, [`2201.11841`].

[147] C. L. Rodriguez, I. Mandel and J. R. Gair, *Verifying the no-hair property of massive compact objects with intermediate-mass-ratio inspirals in advanced gravitational-wave detectors*, *Phys. Rev. D* **85** (2012) 062002 [1112.1404].

[148] B. S. Sathyaprakash and B. F. Schutz, *Physics, Astrophysics and Cosmology with Gravitational Waves*, *Living Rev. Rel.* **12** (2009) 2 [0903.0338].

[149] S. Dhurandar and M. Tinto, *Astronomical observations with a network of detectors of gravitational waves – I. Mathematical framework and solution of the five detector problem*, *Monthly Notices of the Royal Astronomical Society* **234** (1988) 663.

[150] M. Tinto, *Antenna patterns of interferometric detectors of gravitational waves – II. Elliptically and randomly polarized waves*, *Monthly Notices of the Royal Astronomical Society* **226** (1987) 829.

[151] L. S. Finn, *The Response of interferometric gravitational wave detectors*, *Phys. Rev. D* **79** (2009) 022002 [0810.4529].

[152] L. Blanchet, *Gravitational Radiation from Post-Newtonian Sources and Inspiralling Compact Binaries*, *Living Rev. Rel.* **17** (2014) 2 [1310.1528].

[153] M. L. Chan, C. Messenger, I. S. Heng and M. Hendry, *Binary Neutron Star Mergers and Third Generation Detectors: Localization and Early Warning*, *Phys. Rev. D* **97** (2018) 123014 [1803.09680].

[154] H.-Y. Chen, D. E. Holz, J. Miller, M. Evans, S. Vitale and J. Creighton, *Distance measures in gravitational-wave astrophysics and cosmology*, *Class. Quant. Grav.* **38** (2021) 055010 [1709.08079].

[155] K. Belczynski, D. E. Holz, T. Bulik and R. O'Shaughnessy, *The first gravitational-wave source from the isolated evolution of two 40-100 Msun stars*, *Nature* **534** (2016) 512 [1602.04531].

[156] P. Madau, H. C. Ferguson, M. E. Dickinson, M. Giavalisco, C. C. Steidel and A. Fruchter, *High redshift galaxies in the hubble deep field. color selection and star formation history to z=4*, *Mon. Not. Roy. Astron. Soc.* **283** (1996) 1388 [astro-ph/9607172].

[157] A. M. Hopkins and J. F. Beacom, *On the normalisation of the cosmic star formation history*, *Astrophys. J.* **651** (2006) 142 [astro-ph/0601463].

[158] M. A. Fardal, N. Katz, D. H. Weinberg and R. Dav'e, *On the Evolutionary History of Stars and their Fossil Mass and Light*, *Mon. Not. Roy. Astron. Soc.* **379** (2007) 985 [astro-ph/0604534].

[159] S. M. Wilkins, N. Trentham and A. M. Hopkins, *The Evolution of Stellar Mass and the Implied Star Formation History*, *Mon. Not. Roy. Astron. Soc.* **385** (2008) 687 [0801.1594].

[160] P. Madau and M. Dickinson, *Cosmic Star Formation History*, *Ann. Rev. Astron. Astrophys.* **52** (2014) 415 [1403.0007].

[161] J. A. de Freitas Pacheco, T. Regimbau, S. Vincent and A. Spallicci, *Expected coalescence rates of ns-ns binaries for laser beam interferometers*, *Int. J. Mod. Phys. D* **15** (2006) 235 [astro-ph/0510727].

[162] T. Regimbau et al., *A Mock Data Challenge for the Einstein Gravitational-Wave Telescope*, *Phys. Rev. D* **86** (2012) 122001 [1201.3563].

[163] V. Sahni and A. A. Starobinsky, *The Case for a positive cosmological Lambda term*, *Int. J. Mod. Phys. D* **9** (2000) 373 [astro-ph/9904398].

[164] M. Safarzadeh and E. Berger, *Measuring the delay time distribution of binary neutron stars. I. Through Scaling Relations of the Host Galaxies of Gravitational Wave Events*, *Astrophys. J. Lett.* **878** (2019) L12 [1904.08436].

[165] M. Safarzadeh, E. Berger, K. K. Y. Ng, H.-Y. Chen, S. Vitale, C. Whittle et al., *Measuring the delay time distribution of binary neutron stars. II. Using the redshift distribution from third-generation gravitational wave detectors network*, *Astrophys. J. Lett.* **878** (2019) L13 [1904.10976].

[166] M. Safarzadeh, E. Berger, J. Leja and J. S. Speagle, *Measuring the delay time distribution of binary neutron stars. III. Using the individual star formation histories of gravitational wave event host galaxies in the local universe*, [1905.04310].

[167] K. K. Y. Ng, S. Vitale, W. M. Farr and C. L. Rodriguez, *Probing multiple populations of compact binaries with third-generation gravitational-wave detectors*, [2012.09876].

[168] *Rubin Observatory System & LSST Survey Key Numbers*, (2022), https://www.lsst.org/scientists/keynumbers.

[169] *Euclid Technical Details*, https://www.euclid.caltech.edu/page/technical-details.

[170] *Athena*, https://arxiv.org/abs/1308.6785.

[171] *Roman Space Telescope: Wide-Field Instrument*, https://roman.gsfc.nasa.gov/science/WFI_technical.html.

[172] *Chandra X-ray Observatory*, https://heasarc.gsfc.nasa.gov/docs/chandra/chandra.html.

[173] *Lynx*, https://www.lynxobservatory.com/mission.

[174] *Swift–XRT*, https://heasarc.gsfc.nasa.gov/docs/heasarc /caldb/swift/docs/xrt/XRT_SPIE_2003_final.pdf.

[175] *30m–Telescope*, https://www.eso.org/sci/meetings/2011 /feedgiant/presentations/Davidge.pdf.

[176] *Keck*, https://www.ucobservatories.org/projects_at/fobos/.

[177] *VLT*, https://www.eso.org/sci/facilities/paranal /decommissioned/vimos.html.

[178] *ELT*, https://elt.eso.org/about/facts/.

[179] *GMT*, https://www.gmto.org/wp-content/uploads/2021/11/ Instrumentation-progress-at-the-Giant-Magellan-Telescope-project.pdf.

[180] *HST–WFC3*, https://www.nasa.gov/content/hubble-space-telescope-wide-field-camera-3.

[181] L. P. Singer et al., *Going the Distance: Mapping Host Galaxies of LIGO and Virgo Sources in Three Dimensions Using Local Cosmography and Targeted Follow-up*, *Astrophys. J. Lett.* **829** (2016) L15 [1603.07333].

[182] LIGO SCIENTIFIC, VIRGO, FERMI-GBM, INTEGRAL collaboration, *Gravitational Waves and Gamma-rays from a Binary Neutron Star Merger: GW170817 and GRB 170817A*, *Astrophys. J. Lett.* **848** (2017) L13 [1710.05834].

[183] M. Ajello et al., *Fermi-LAT Observations of LIGO/Virgo Event GW170817*, *Astrophys. J.* **861** (2018) 85.

[184] V. Savchenko et al., *INTEGRAL Detection of the First Prompt Gamma-Ray Signal Coincident with the Gravitational-wave Event GW170817*, *Astrophys. J. Lett.* **848** (2017) L15 [1710.05449].

[185] (2017), https://gcn.gsfc.nasa.gov/other/G298048.gcn3.

[186] S. Sachdev et al., *An Early-warning System for Electromagnetic Follow-up of Gravitational-wave Events*, *Astrophys. J. Lett.* **905** (2020) L25 [2008.04288].

[187] K. Cannon et al., *Toward Early-Warning Detection of Gravitational Waves from Compact Binary Coalescence*, *Astrophys. J.* **748** (2012) 136 [1107.2665].

[188] T. Tsutsui, A. Nishizawa and S. Morisaki, *Early warning of precessing compact binary merger with third-generation gravitational-wave detectors*, *Phys. Rev. D* **104** (2021) 064013 [2011.06130].

[189] S. J. Kapadia, M. K. Singh, M. A. Shaikh, D. Chatterjee and P. Ajith, *Of Harbingers and Higher Modes: Improved gravitational-wave early-warning of compact binary mergers*, *Astrophys. J. Lett.* **898** (2020) L39 [2005.08830].

[190] M. K. Singh, S. J. Kapadia, M. A. Shaikh, D. Chatterjee and P. Ajith, *Improved early warning of compact binary mergers using higher modes of gravitational radiation: A population study*, *Mon. Not. Roy. Astron. Soc.* **502** (2021) 1612

[2010.12407].

[191] T. Tsutsui, A. Nishizawa and S. Morisaki, *Early warning of precessing neutron-star black-hole binary mergers with the near-future gravitational-wave detectors*, [2107.12531].

[192] Y. Li, I. S. Heng, M. L. Chan, C. Messenger and X. Fan, *Exploring the sky localization and early warning capabilities of third generation gravitational wave detectors in three-detector network configurations*, [2109.07389].

[193] A. H. Nitz and T. Dal Canton, *Pre-merger Localization of Compact-binary Mergers with Third-generation Observatories*, *Astrophys. J. Lett.* **917** (2021) L27 [2106.15259].

[194] M. K. Singh, Divyajyoti, S. J. Kapadia, M. A. Shaikh and P. Ajith, *Improved early-warning estimates of luminosity distance and orbital inclination of compact binary mergers using higher modes of gravitational radiation*, [2202.05802].

[195] S. Akcay, *Forecasting Gamma-Ray Bursts Using Gravitational Waves*, *Annalen Phys.* **531** (2019) 1800365 [1808.10057].

[196] G. Baltus, J. Janquart, M. Lopez, A. Reza, S. Caudill and J.-R. Cudell, *Convolutional neural networks for the detection of the early inspiral of a gravitational-wave signal*, *Phys. Rev. D* **103** (2021) 102003 [2104.00594].

[197] R. Magee et al., *First demonstration of early warning gravitational wave alerts*, *Astrophys. J. Lett.* **910** (2021) L21 [2102.04555].

[198] H. Yu, R. X. Adhikari, R. Magee, S. Sachdev and Y. Chen, *Early warning of coalescing neutron-star and neutron-star-black-hole binaries from the nonstationary noise background using neural networks*, *Phys. Rev. D* **104** (2021) 062004 [2104.09438].

[199] B. S. Sathyaprakash and S. V. Dhurandhar, *Choice of filters for the detection of gravitational waves from coalescing binaries*, *Phys. Rev. D* **44** (1991) 3819.

[200] W. Israel, *Event horizons in static vacuum space-times*, *Phys. Rev.* **164** (1967) 1776.

[201] B. Carter, *Axisymmetric Black Hole Has Only Two Degrees of Freedom*, *Phys. Rev. Lett.* **26** (1971) 331.

[202] O. Dreyer, B. J. Kelly, B. Krishnan, L. S. Finn, D. Garrison and R. Lopez-Aleman, *Black hole spectroscopy: Testing general relativity through gravitational wave observations*, *Class. Quant. Grav.* **21** (2004) 787 [gr-qc/0309007].

[203] E. Berti, J. Cardoso, V. Cardoso and M. Cavaglia, *Matched-filtering and parameter estimation of ringdown waveforms*, *Phys. Rev. D* **76** (2007) 104044 [0707.1202].

[204] S. Gossan, J. Veitch and B. S. Sathyaprakash, *Bayesian model selection for testing the no-hair theorem with black hole ringdowns*, *Phys. Rev. D* **85** (2012) 124056 [1111.5819].

[205] I. Kamaretsos, M. Hannam, S. Husa and B. S. Sathyaprakash, *Black-hole hair loss: learning about binary progenitors from ringdown signals*, *Phys. Rev. D* **85** (2012) 024018 [1107.0854].

[206] I. Kamaretsos, M. Hannam and B. Sathyaprakash, *Is black-hole ringdown a memory of its progenitor?*, *Phys. Rev. Lett.* **109** (2012) 141102 [1207.0399].

[207] L. London, D. Shoemaker and J. Healy, *Modeling ringdown: Beyond the fundamental quasinormal modes*, *Phys. Rev. D* **90** (2014) 124032 [1404.3197].

[208] M. Giesler, M. Isi, M. A. Scheel and S. Teukolsky, *Black Hole Ringdown: The Importance of Overtones*, *Phys. Rev. X* **9** (2019) 041060 [1903.08284].

[209] S. Bhagwat, X. J. Forteza, P. Pani and V. Ferrari, *Ringdown overtones, black hole spectroscopy, and no-hair theorem tests*, *Phys. Rev. D* **101** (2020) 044033 [1910.08708].

[210] I. Ota and C. Chirenti, *Overtones or higher harmonics? Prospects for testing the no-hair theorem with gravitational wave detections*, *Phys. Rev. D* **101** (2020) 104005 [1911.00440].

[211] A. Dhani, *Importance of mirror modes in binary black hole ringdown waveform*, *Phys. Rev. D* **103** (2021) 104048 [2010.08602].

[212] A. Dhani and B. S. Sathyaprakash, *Overtones, mirror modes, and mode-mixing in binary black hole mergers*, [2107.14195].

[213] R. Cotesta, G. Carullo, E. Berti and V. Cardoso, *On the detection of ringdown overtones in GW150914*, [2201.00822].

[214] S. Dhanpal, A. Ghosh, A. K. Mehta, P. Ajith and B. S. Sathyaprakash, *A no-hair test for binary black holes*, *Phys. Rev. D* **99** (2019) 104056 [1804.03297].

[215] T. Islam, A. K. Mehta, A. Ghosh, V. Varma, P. Ajith and B. S. Sathyaprakash, *Testing the no-hair nature of binary black holes using the consistency of multipolar gravitational radiation*, *Phys. Rev. D* **101** (2020) 024032 [1910.14259].

[216] J. M. Lattimer, *Equation of State from Neutron Star Mass and Radius Measurements*, *JPS Conf. Proc.* **31** (2020) 011021.

[217] T. Hinderer, B. D. Lackey, R. N. Lang and J. S. Read, *Tidal deformability of neutron stars with realistic equations of state and their gravitational wave signatures in binary inspiral*, *Phys. Rev. D* **81** (2010) 123016 [0911.3535].

[218] T. Damour, A. Nagar and L. Villain, *Measurability of the tidal polarizability of neutron stars in late-inspiral gravitational-wave signals*, *Phys. Rev. D* **85** (2012) 123007 [1203.4352].

[219] W. Kastaun and F. Ohme, *Finite tidal effects in GW170817: Observational evidence or model assumptions?*, *Phys. Rev. D* **100** (2019) 103023 [1909.12718].

[220] D. A. Godzieba, R. Gamba, D. Radice and S. Bernuzzi, *Updated universal relations for tidal deformabilities of neutron stars from phenomenological equations of state*, [2012.12151].

[221] R. Smith et al., *Bayesian Inference for Gravitational Waves from Binary Neutron Star Mergers in Third Generation Observatories*, *Phys. Rev. Lett.* **127** (2021) 081102 [2103.12274].

[222] K. Takami, L. Rezzolla and L. Baiotti, *Constraining the Equation of State of Neutron Stars from Binary Mergers*, *Phys. Rev. Lett.* **113** (2014) 091104 [1403.5672].

[223] S. Bose, K. Chakravarti, L. Rezzolla, B. S. Sathyaprakash and K. Takami, *Neutron-star Radius from a Population of Binary Neutron Star Mergers*, *Phys. Rev. Lett.* **120** (2018) 031102 [1705.10850].

[224] M. Breschi, S. Bernuzzi, F. Zappa, M. Agathos, A. Perego, D. Radice et al., *kiloHertz gravitational waves from binary neutron star remnants: time-domain model and constraints on extreme matter*, *Phys. Rev. D* **100** (2019) 104029 [1908.11418].

[225] P. J. Easter, S. Ghonge, P. D. Lasky, A. R. Casey, J. A. Clark, F. H. Vivanco et al., *Detection and parameter estimation of binary neutron star merger remnants*, *Phys. Rev. D* **102** (2020) 043011 [2006.04396].

[226] M. Shibata, K. Taniguchi and K. Uryu, *Merger of binary neutron stars with realistic equations of state in full general relativity*, *Phys. Rev. D* **71** (2005) 084021 [gr-qc/0503119].

[227] M. Shibata, K. Taniguchi and K. Uryu, *Merger of binary neutron stars of unequal mass in full general relativity*, *Phys. Rev. D* **68** (2003) 084020 [gr-qc/0310030].

[228] M. Prakash, J. R. Cooke and J. M. Lattimer, *Quark - hadron phase transition in protoneutron stars*, *Phys. Rev. D* **52** (1995) 661.

[229] E. R. Most, L. J. Papenfort, V. Dexheimer, M. Hanauske, S. Schramm, H. Stöcker et al., *Signatures of quark-hadron phase transitions in general-relativistic neutron-star mergers*, *Phys. Rev. Lett.* **122** (2019) 061101 [1807.03684].

[230] S. Blacker, N.-U. F. Bastian, A. Bauswein, D. B. Blaschke, T. Fischer, M. Oertel et al., *Constraining the onset density of the hadron-quark phase transition with gravitational-wave observations*, *Phys. Rev. D* **102** (2020) 123023 [2006.03789].

[231] V. Srivastava, D. Davis, K. Kuns, P. Landry, S. Ballmer, M. Evans et al., *Science-Driven Tunable Design of Cosmic Explorer Detectors*, [2201.10668].

[232] C. M. Will, *The Confrontation between General Relativity and Experiment*, *Living Rev. Rel.* **17** (2014) 4 [1403.7377].

[233] E. Berti et al., *Testing General Relativity with Present and Future Astrophysical Observations*, *Class. Quant. Grav.* **32** (2015) 243001 [1501.07274].

[234] N. Yunes and X. Siemens, *Gravitational-Wave Tests of General Relativity with Ground-Based Detectors and Pulsar Timing-Arrays*, *Living Rev. Rel.* **16** (2013) 9 [1304.3473].

[235] W. G. Unruh and R. M. Wald, *Information Loss*, *Rept. Prog. Phys.* **80** (2017) 092002 [1703.02140].

[236] S. W. Hawking, *Breakdown of Predictability in Gravitational Collapse*, *Phys. Rev. D* **14** (1976) 2460.

[237] SUPERNOVA SEARCH TEAM collaboration, *Observational evidence from supernovae for an accelerating universe and a cosmological constant*, *Astron. J.* **116** (1998) 1009 [astro-ph/9805201].

[238] SUPERNOVA COSMOLOGY PROJECT collaboration, *Measurements of Ω and Λ from 42 high redshift supernovae*, *Astrophys. J.* **517** (1999) 565 [astro-ph/9812133].

[239] S. W. Hawking and R. Penrose, *The Singularities of gravitational collapse and cosmology*, *Proc. Roy. Soc. Lond. A* **314** (1970) 529.

[240] S. E. Perkins, N. Yunes and E. Berti, *Probing Fundamental Physics with Gravitational Waves: The Next Generation*, *Phys. Rev. D* **103** (2021) 044024 [2010.09010].

[241] A. Ghosh et al., *Testing general relativity using golden black-hole binaries*, *Phys. Rev. D* **94** (2016) 021101 [1602.02453].

[242] A. Ghosh, N. K. Johnson-Mcdaniel, A. Ghosh, C. K. Mishra, P. Ajith, W. Del Pozzo et al., *Testing general relativity using gravitational wave signals from the inspiral, merger and ringdown of binary black holes*, *Class. Quant. Grav.* **35** (2018) 014002 [1704.06784].

[243] M. Abernathy et al., *Einstein Gravitational-Wave Telescope: Conceptual Design Study*. Available at: https://tds.virgo-gw.eu/?call_file=ET-0106C-10.pdf, (2010).

[244] X. Zhang, J. Yu, T. Liu, W. Zhao and A. Wang, *Testing Brans-Dicke gravity using the Einstein telescope*, *Phys. Rev. D* **95** (2017) 124008 [1703.09853].

[245] K. G. Arun and C. M. Will, *Bounding the mass of the graviton with gravitational waves: Effect of higher harmonics in gravitational waveform templates*, *Class. Quant. Grav.* **26** (2009) 155002 [0904.1190].

[246] A. Samajdar and K. G. Arun, *Projected constraints on the dispersion of gravitational waves using advanced ground- and space-based interferometers*, *Phys. Rev. D* **96** (2017) 104027 [1708.00671].

[247] D. Schaerer, *On the Properties of massive population III stars and metal-free stellar populations*, *Astron. Astrophys.* **382** (2002) 28 [astro-ph/0110697].

[248] Z.-C. Chen and Q.-G. Huang, *Distinguishing Primordial Black Holes from Astrophysical Black Holes by Einstein Telescope and Cosmic Explorer*, *JCAP* **08** (2020) 039 [1904.02396].

[249] K. K. Y. Ng, S. Chen, B. Goncharov, U. Dupletsa, S. Borhanian, M. Branchesi et al., *On the single-event-based identification of primordial black hole mergers at cosmological distances*, [2108.07276].

[250] S. Clesse and J. García-Bellido, *Massive Primordial Black Holes from Hybrid Inflation as Dark Matter and the seeds of Galaxies*, *Phys. Rev. D* **92** (2015) 023524 [1501.07565].

[251] J. García-Bellido, *Massive Primordial Black Holes as Dark Matter and their detection with Gravitational Waves*, *J. Phys. Conf. Ser.* **840** (2017) 012032 [1702.08275].

[252] M. Volonteri, F. Haardt and P. Madau, *The Assembly and merging history of supermassive black holes in hierarchical models of galaxy formation*, *Astrophys. J.* **582** (2003) 559 [astro-ph/0207276].

[253] P. Natarajan et al., *Disentangling nature from nurture: tracing the origin of seed black holes*, [1904.09326].

[254] L. Barack et al., *Black holes, gravitational waves and fundamental physics: a roadmap*, *Class. Quant. Grav.* **36** (2019) 143001 [1806.05195].

[255] M. Volonteri, *Formation of Supermassive Black Holes*, *Astron. Astrophys. Rev.* **18** (2010) 279 [1003.4404].

[256] R. Valiante, M. Colpi, R. Schneider, A. Mangiagli, M. Bonetti, G. Cerini et al., *Unveiling early black hole growth with multifrequency gravitational wave observations*, *Mon. Not. Roy. Astron. Soc.* **500** (2020) 4095 [2010.15096].

[257] M. Volonteri, M. Habouzit and M. Colpi, *The origins of massive black holes*, *Nature Rev. Phys.* **3** (2021) 732 [2110.10175].

[258] M. Vallisneri, *Use and abuse of the Fisher information matrix in the assessment of gravitational-wave parameter-estimation prospects*, *Phys. Rev. D* **77** (2008) 042001 [gr-qc/0703086].

[259] Z. Wang, C. Liu, J. Zhao and L. Shao, *Extending the Fisher Information Matrix in Gravitational-wave Data Analysis*, *Astrophys. J.* **932** (2022) 102 [2203.02670].

[260] U. Dupletsa, J. Harms, K. K. Y. Ng, J. Tissino, F. Santoliquido and A. Cozzumbo, *Validating Prior-informed Fisher-matrix Analyses against GWTC Data*, [2404.16103].